Study of the Energetics of Polycyclic Aromatic Hydrocarbons and their Interstellar Implications

Brandi Justina West

Thesis submitted to the
Faculty of Graduate & Postdoctoral Studies
University of Ottawa
In partial fulfillment of the requirements for the
Ph.D. degree in the Ottawa-Carleton Chemistry Institute

Department of Chemistry

Faculty of Science

University of Ottawa

Dedicated to my parents,
Words can’t express how much you mean to me.
This would not have been possible without your support,
so all I’m going to say is...

I did it!

“Shoot for the moon. Even if you miss, you'll land among the stars.”
— Norman Vincent Peale

Abstract

Interstellar chemistry has been a growing field over the last several decades. There is particular interest on the nature and reactivity of interstellar molecules; most notably that of polycyclic aromatic hydrocarbons (PAHs). My thesis focused on the kinetics of unimolecular dissociation of small PAH and PAH-like molecules under interstellar conditions. PAHs (naphthalene (NAP), anthracene (ANT) and pyrene (PYR)), some dihydro- equivalents (1,2-dihydronapthalene (DHN) and 9,10-dihydrophenanthrene (DHP)) and a few other small aromatic organic molecules (indene (IND), ethynylbenzene (EB), propynylbenzene (PB) and benzocyclobutene (BCB)) were studied using imaging photo-electron photo-ion coincidence spectroscopy (iPEPICO) and electron impact mass spectrometry (MS); both mass analyzed ion kinetic energy spectrometry (MIKES) and collision induced dissociation (CID). Experiments were performed at different ionization energies to produce breakdown diagrams for the various fragments. These diagrams are then fit using RRKM theory to determine the zero Kelvin activation energy (E_0) and the entropy of activation ($\Delta^{\ddagger}S$); these results are then compared and discussed.

All these molecules were compared in order to try and find any overlying trends which could be applied to their role in the interstellar medium (ISM). It was determined that H loss was the dominant fragmentation channel, as it was the only dissociation channel common to the majority of molecules studied. It was also seen that organic fragment loss (C_2H_2, CH_3 and C_4H_2) was only observed in smaller molecules which indicates that PAHs are not likely a source of these molecules. The small fragment molecules gave insight into the stability of closed ring structures, such as PAHs, through the comparison of the

dissociation of closed and open structures. The dihydro-PAHs, selected as a probe to investigate the proposed catalytic role of PAHs in the formation of molecular hydrogen, yielded very interesting results. It was seen that these molecules would readily undergo isomerisation prior to dissociation. This added an unexpected level of difficulty to the calculations but quickly demonstrated how the presence of additional hydrogen atoms could greatly disrupt the dissociations, as it was not the simple process of removing them as it was originally believed.

The overall trend observed was that it is the structure, not the size, which has the dominating effect on the dissociation. Ions of similar structure behaved similarly, regardless of a change in mass; isomers, however, had radically different behaviours which can only be attributed to their differing molecular conformations. This observation could aid in the understanding of larger PAHs, those which are believed to exist in the ISM, and what role they may play in the chemistry of the universe.

Acknowledgements

Firstly, I want to thank my family. Without their support I don't know if I would have continued with my studies as long as I did. I especially want to thank my parents. When I first told them I wanted to do a PhD they were overjoyed but not surprised; they were never surprised by my accomplishments simply because they never doubted my abilities. Their unshakable confidence in me held me up when I had no confidence in myself.

Next, I would like to thank my supervisor, Dr. Paul Mayer. He too had faith in my abilities from the beginning and I cannot thank him enough for everything he has done for me to make the last 5 years of my life truly memorable. I am grateful that he was able to cope with my idiosyncrasies in times of stress, which probably happened more often than is typical.

I would also like to thank Dr. Sander Mommers and Dr. John Holmes. They helped me deal with, what at times, was the most frustrating instrument. I have never felt such relief as I did whenever they came into the lab and decided to sit with me while I was doing an experiment; or sometimes they would just say the one thing that I needed to know to get my experiment to work. They are both endless fonts of knowledge and I hope that I will be able to continue to call on their council as I pursue my scientific career.

To all my friends: in Ottawa, back home, and those I've met in my travels, I owe them all my sanity. They never let me take myself too seriously and were always willing to give me a wonderful distraction when the stress became too much. I don't know if I say this enough but from the bottom of my heart I thank you.

In my time with the Mayer group I've decided that there is no better group of people than those in the lab, both present and past. They have been some of the greatest friends and I hope that we stay in contact. I will never forget the pranks, the lunchtime euchre tournaments, as well as all the truly great discussions I've had with many of them. Over the course of five years there have been so many of you that I hesitate to address you by name for fear of forgetting someone, but please know that I think of you all often and remember our time together fondly.

Publications

1. West, B.; Joblin, C.; Blanchet, V.; Bodi, A.; Sztáray, B.; Mayer, P. M., On the Dissociation of the Naphthalene Radical Cation: New iPEPICO and Tandem Mass Spectrometry Results. *J. Phys. Chem. A* **2012,** *116* (45), 10999-11007.

The research with naphthalene was used to validate the process by comparison with the extensive literature. While fitting the data it was seen that the literature had largely ignored the minor primary channels (M-H_2 and M-C_4H_2), which allowed us to expand the current knowledge. We were also able to look at consecutive dissociations, and match literature from separate experiments for each step (looking at $C_{10}H_8^{\bullet}$ and $C_{10}H_7^+$).

2. West, B.; Joblin, C.; Blanchet, V.; Bodi, A.; Sztáray, B.; Mayer, P., Dynamics of hydrogen and methyl radical loss from ionized dihydro-polycyclic aromatic hydrocarbons: a tandem mass spectrometry and imaging-PEPICO study of dihydronaphthalene and dihydrophenanthrene. *J. Phys. Chem. A* **2014,** *118* (10), 1807-1816.

The research on the DHP had not been done previously, and the literature for DHN was scarce. The literature values used for comparison were from protonated PAHs for the comparison of secondary channels for DHN. The results of this research adds to the knowledge of how PAHs may participate in H_2 formation, primarily how the introduction of additional H atoms affect the energetic. These molecules also introduced the idea of isomerisation upon H absorption onto PAHs.

3. West, B.; Sit, A.; Mohamed, S.; Joblin, C.; Blanchet, V.; Bodi, A.; Mayer, P., Dissociation of the Anthracene Radical Cation: A Comparative Look at iPEPICO and Collision-Induced Dissociation Mass Spectrometry Results. *J. Phys. Chem. A* **2014**, submitted.

The research for anthracene was used to test the viability of using APCI-CID as another method for studying the energetic of PAHs. It has fewer size restrictions and thus would allow for the study of molecules which are otherwise difficult to study. The anthracene results also demonstrated that the dissociation energies for catacondensed PAHs are unaffected by size which makes it possible to started looking at trends in their dissociation.

4. West, B.; Sit, A.; Bodi, A.; Hemberger, P.; Mayer, P. M., Dissociative Photoionization and Threshold Photoelectron Spectra of Polycyclic Aromatic Hydrocarbon Fragments: An iPEPICO Study of Four Substituted Benzene Radical Cations. **2014**, in preparation.

The research on these small molecules has turned out to be very enlightening on the possible fate of the product ions post PAH fragmentation in the ISM. The use of 'isomer-like' molecules gives insight into how the structure of the resulting ion affects its survival in the ISM. This paper will be submitted for publication in the very near future.

5. West, B.; Useli-Bacchitta, F.; Sabbah, H.; Blanchet, V.; Bodi, A.; Mayer, P. M.; Joblin, C., Photodissociation of Pyrene: Structure and Energetics from $C_{16}H_{10}^{+}$ to C_{14}^{+} and almost everything in between. **2014**, in preparation.

The research for pyrene has added a lot of information to the field. First, by pairing up with the PIRENEA experiment, a much more elaborate fragmentation map has been developed which give new insight into how PAHs dissociate under photodissociation conditions. The iPEPICO results show that going to larger molecules isn't necessarily as useful as first thought, at least with this experiment; this allows us to focus our energy on the small molecules which we know gives good energetic results. This paper is also just about ready for publication.

Table of Contents

List of Figures

List of Tables

List of Abbreviations

Abbreviation	Description	Abbreviation	Description
1 MI	1-Methylindene	FTICR	Fourier Transform Ion Cyclotron Resonance
9 MF	9-Methylfluorene	IE or IP	Ionization Energy or Ionization Potential
ANT	Anthracene	iPEPICO	imaging photoelectron photoion coincidence spectroscopy
BCB	Benzocyclobutene	IR	Infrared
DHN	1,2-Dihydronaphthalene	ISM	Interstellar Medium
DHP	9,10-Dihydrophenanthrene	m/z	Mass to Charge Ratio
EB	Ethynylbenzene	MCP	Microchannel Plate
IND	Indene	MI-CID	Metastable Ion CID
NAP	Naphthalene	MIKES	Mass-analyzed Ion Kinetic Energy Spectrometry
PB	Propynylbenzene	MO	Molecular Orbital
PYR	Pyrene	MSMS	Tandem Mass Spectrometry
APCI	Atmospheric Pressure Chemical Ionization	PAH	Polycyclic Aromatic Hydrocarbons
B3LYP	Becke 3-Parameter (Exchange), Lee, Yang and Parr	PIRENEA	Piège à Ions pour la Recherche et l'Etude de Nouvelles Espèces Astrochimiques
CID	Collision Induced Dissociation	RRKM	Rice–Ramsperger–Kassel–Marcus
cm^{-1}	Wavenumbers	SLS	Swiss Light Source
DFT	Density Functional Theory	TOF	Time-of-Flight
DIB	Diffuse Interstellar Bands	TPES	Threshold Potential Energy Surface
E_0	0K Activation Energy	TS	Transition State
EI	Electron Ionization	UV or VUV	Ultraviolet or Vacuum Ultraviolet
ESA	Electrostatic Analyzer	ZAB	Zero Aberration
ESI	Electrospray Ionization	ZPE	Zero Point Energy
eV	Electronvolt	$\Delta^{\ddagger}S$	Entropy of Activation
FFR	Field Free Region	ΔE	Energy Difference

1 Introduction

1.1 Objective

The goal of this thesis was to study the unimolecular dissociation of numerous polycyclic aromatic hydrocarbons (PAHs) and related species under conditions similar to those found in the interstellar medium (ISM). Using computational modelling, statistical rate theory and a combination of mass spectrometry techniques (MIKES, CID, MI-CID and iPEPICO, to be defined below) the unimolecular dissociation of three PAHs (naphthalene, anthracene and pyrene), two PAH derivatives (1,2-dihydronaphthalene and 9,10-dihydrophenanthrene) and four possible PAH fragments (indene, propynylbenzene, benzocyclobutene and ethynylbenzene) were studied and their 0K activation energies (E_0) and entropies of activation ($\Delta^{\ddagger}S$) were measured for all primary and consecutive dissociation channels in the hope that these numbers will aid in the improvement of current PAH models used in the attempt to understand their role in the ISM.

1.2 The Interstellar Medium

Interstellar chemistry has been an ongoing, interdisciplinary study since the first interstellar molecules were discovered between 1937-1941.[1] Since then, more and more complex molecules have been observed as well as a plethora of small molecules. Over two hundred small molecules, all containing less than 10 atoms, have been positively identified in the ISM with many of the more complex species being postulated.[2] The most complex inorganic molecules which have been discovered are various forms of carbon clusters and

hydrocarbons; to date, diamond, amorphous carbon and graphene type structures have been theorized; meanwhile the group which has garnered the most attention is that of fullerenes.[3] Fullerenes have been the focus of both interstellar and laboratory studies for several decades, but renewed interest has occurred since their positive identification in the ISM in 2010.[4] Of the molecules which have been discovered, the vast majority are organic in nature; many of which are hydrocarbons that may contain oxygen or nitrogen.[5] The most complex of the organic molecules which are proposed to be present, and are the subject of this thesis, is that of PAHs. [6] While there is still a debate over the specific PAHs present, the general consensus is that the vast majority of them must be large, compact examples in order to survive the conditions in the ISM. These molecules will be discussed in more detail in the following section.

Before a discussion about interstellar chemistry can proceed, it is necessary to discuss how the ISM differs from terrestrial conditions. For this comparison, Figure 1 shows the variance in temperature and pressure with increasing altitude in the atmosphere. [7] As there is no firm boundary separating the atmosphere from the ISM, as you travel further from the surface the pressures and temperatures will approach those in the ISM.

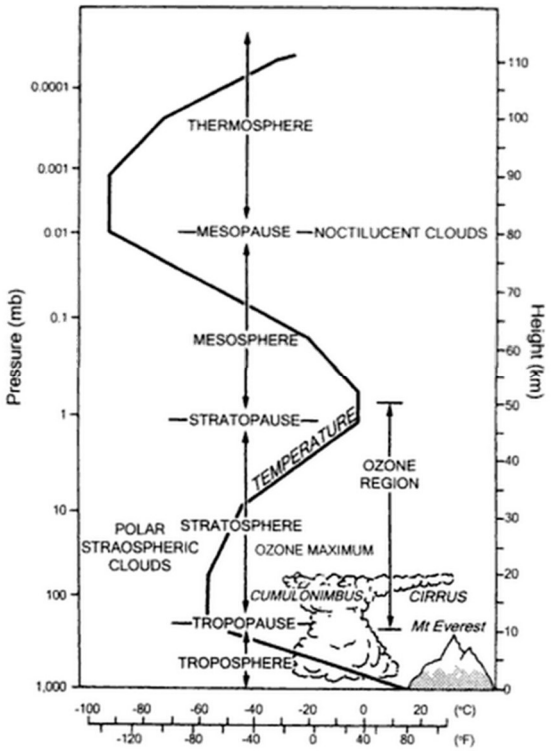

Figure 1: Chart relating atmospheric temperature and pressure with increasing height above sea level.[7]

If the atmosphere is considered up to stratopause, where the ozone layer ends, then the pressure ranges from 1000 – 1 mbar and temperatures range from 298 – 238 K based on average temperatures at each altitude. By comparison, the conditions of the ISM are extreme; with particle densities ranging between 10^{-4} and 10^{5} cm^{-3} (translating to pressures between 10^{-21} and 10^{-6} mbar) while the temperatures range from only 10 – 150 K.[8] The ISM is far from homogeneous, so each region can be considered separately. The least dense regions are the diffuse atomic regions which are defined by a very low H_2 ratio (as compared to other forms of H) of less than 0.1. This is an indication that the majority of elements are in atomic form. These are the hottest regions and are exposed to the most radiation; while H atoms remain neutral, any species with an ionization energy (IE) lower than that will exist as ions, such as C^{+}.[8] The next level would be the diffuse and dense

molecular clouds. It is believed that dense clouds evolve from the diffuse.[9] These clouds are where molecules begin to play a role, though their concentrations are orders of magnitude lower than that of H_2.[10] The denser the clouds the less radiation can penetrate them which gives a spectrum of chemical processes which can occur depending on the density. The last region to be discussed is the photospheres of old stars. These areas consist of large, dense cloud, known as envelopes, which possess a wide range of molecular species. These areas are believed to be the best source of synthetic reactions. Photospheres of stars have vast temperature ranges (10-10^4 K) where higher temperatures will increase reaction rates, but they also possess high UV radiation. While PAH molecules are stable enough to withstand the radiation, most molecular species are not. Therefore while there is a lot of matter surrounding these stars, it is believed to be composed of mostly atomic species.[10] As will be shown in the following section, diffuse molecular clouds are the environment most likely to contain our molecules of interest, PAHs, and thus it is these conditions that will be simulated in the laboratory experiments.

Another factor to the environment of the interstellar medium is that of radiation. If radiation is only described as electromagnetic radiation, then it is a safe assumption that all the electromagnetic spectrum is present in the various ISM environments to a greater or lesser degree based on the photoemission of stars.[11] Depending on the temperature of the star, it will emit different wavelengths of radiation; the hotter the star the higher energy radiation it emits.[12] Depending on the local environment, different wavelengths and amounts of radiation will be available; this was alluded to when describing diffuse clouds. Hydrogen and helium atoms, due to their overwhelming presence in the ISM, have an overall effect on the available radiation regardless of the local environment; they will absorb

any emitted radiation greater than 13.6 eV, up to approximately 100 eV.[13] The absorption typically occurs directly outside the photosphere of stars, which precludes the presence of wavelengths greater than 13.6 eV anywhere in the ISM. Another form of 'radiation' which has an effect on the chemistry of the ISM is that of cosmic rays. While cosmic rays are not technically radiation, they do have a similar effect on the molecules in the ISM. Cosmic rays are defined as high energy atomic nuclei travelling at ultrarelativistic speeds. These particles can cause the ionization of any atom in their path and the ejected electrons are of such a high energy that they too will cause secondary ionization; the energy range of these particles are measured in GeV.[13]

Observation of interstellar molecules presents a unique challenge simply due to their environment as well as ours. The majority of these species are observed by spectroscopy, both emission and absorption, over all the electromagnetic spectrum. The oldest method of detection, as it can be conducted from the surface of the earth, is microwave spectroscopy. The first diatomics detected in the late 1930s were observed by microwave spectroscopy, and dozens more were discovered by the 1960s.[14] This technique is still widely used for the observation of interstellar molecules with more than 150 species discovered in the last 50 years via this method.[15]

Vibrational spectra of the ISM have been studied extensively for the last several decades. The primary cause for this is the uniform presence of specific strong absorption features found throughout the ISM in different local environments known as the diffuse interstellar bands (DIB), two representative spectra are shown in Figure 2.

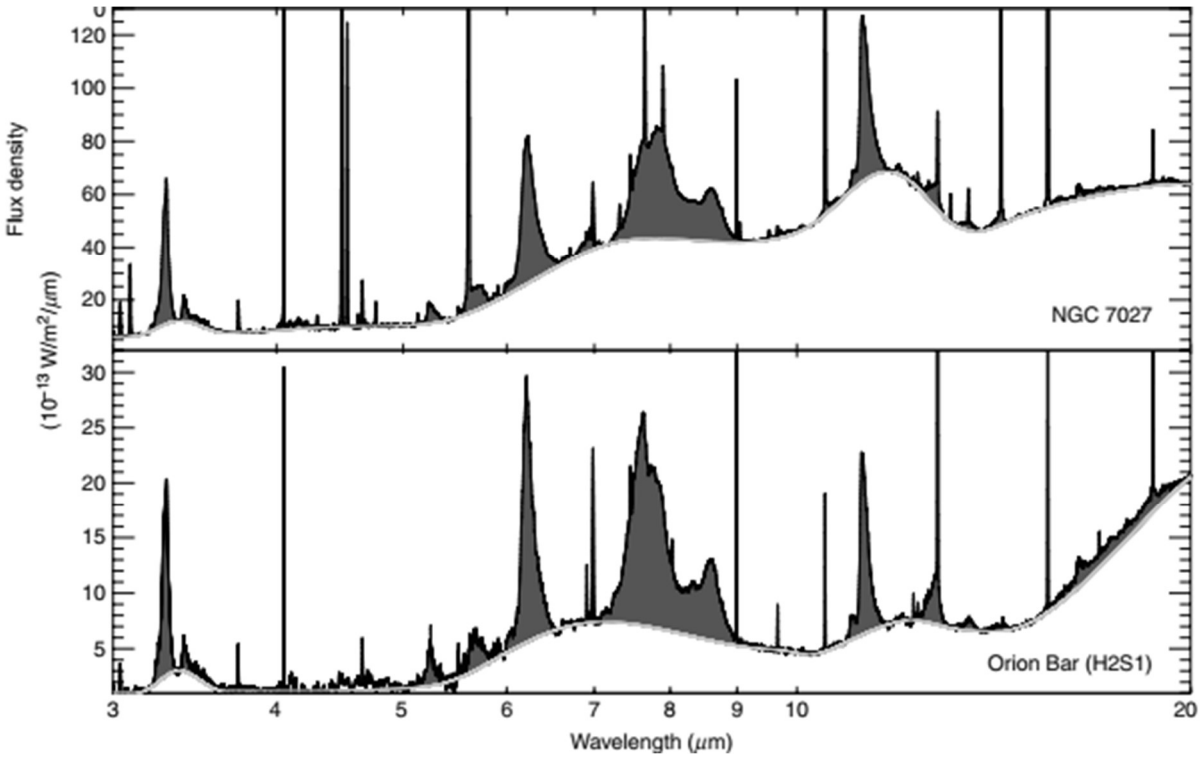

Figure 2: Two representative examples of the vibrational spectra found in the ISM. The shaded features are referred to as DIBs.[16]

While the presence of the DIBs make using IR spectroscopy for molecular identification difficult, this method has been used extensively to learn more about the ISM; based on the presence and concentration of known molecules, such as CO.[17] The DIBs themselves have been the focus of intense research since their discovery; the primary goal being to positively identify the specie or species responsible for them.[18] They will be discussed further in the next section.

The last spectroscopic method that will be presented is that of electronic spectroscopy. Figure 3 shows the UV spectrum measured by the Far Ultraviolet

Spectroscopic Explorer; it can be seen that the UV region of the electromagnetic spectrum has many features present in the ISM. Most of the signal is due to H_2, but there are still some unidentified features to investigate.[19]

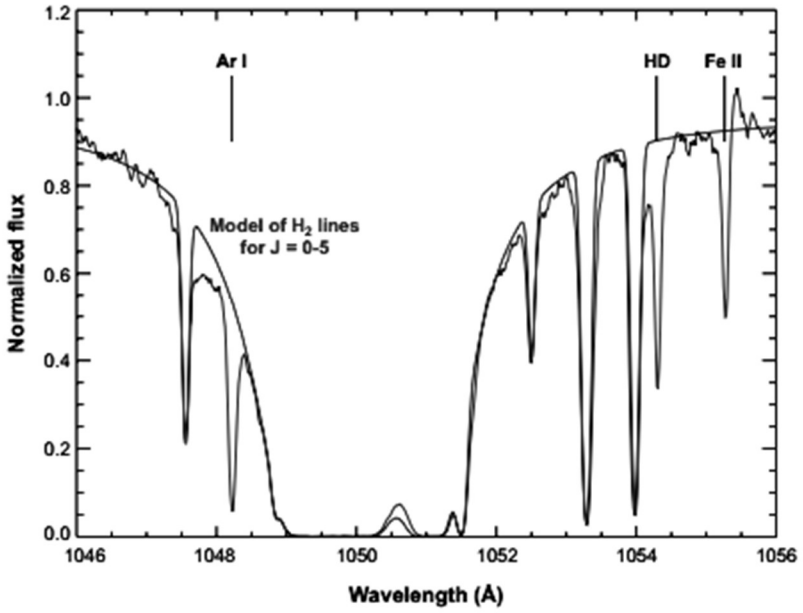

Figure 3: UV spectrum showing interstellar absorption lines obtained by NASA. The calculated spectrum of H_2 is overlaid to show the identity of the majority of the signals though there are some still unidentified (1048 Å).[19]

In order to be able to identify the species which are responsible for all the unknown features in the ISM, it is necessary to first record their spectra in the laboratory setting for comparison.[20] This is where much of the focus is right now, measuring spectra in laboratory conditions approaching those of the ISM.[21-23]

Now that molecules have been identified, a lot of research is focused on the chemistry of the ISM; the players are known so now it is time to find out what game they are playing. Due to the plethora of ionization sources in the ISM, and the low pressures which

give the ionized species sufficiently long lifetimes, ion-molecule reactions are of particular importance. With the absence of any substantial reaction barrier, these reactions can occur quickly even at the low temperatures found in the ISM.[24-25] The rate of ion-molecule reactions is completely independent of temperature, the average rate constant being about 10-100 times greater than for neutral reactions.[25] The majority of these studies have been laboratory studies using instruments designed to simulate the ISM to the best of our abilities.[25-26] Where laboratory studies are not possible, computational chemistry has been employed.[27]

1.3 Polycyclic Aromatic Hydrocarbons in the ISM

The DIBs, also sometimes referred to as the unidentified interstellar bands, are a group of approximately 400 absorption features ranging from the near UV to the near IR.[28] The features, seen in Figure 2 of section 1.2, have been observed in a wide range of interstellar locations, over a hundred different spectra have been measured, dependant on sightlines between the spectrometer and an appropriate star to act as a light source.[29] While the DIBs were discovered back in 1922, their cause is still unknown; it has been determined they are due to molecular emissions, as opposed to atomic, due to their broad nature.[29] Since 1985, the most popular theory for the species responsible for this mystery is that of neutral and ionized PAHs.[6] The primary reason for this assignment is based on promising laboratory studies which hint at peak matching between a combination of different PAHs and the DIBs.[30] The current belief is that PAH molecules are excited by UV radiation, which causes

rapid heating of the molecule followed by IR emission (among other relaxation methods).[31] While PAHs haven't been positively identified in the ISM, they have been studied extensively in the lab using comparable methods to those used in the ISM, spectroscopy ranging from UV to IR under a range of conditions such as matrix isolation,[32-33] mass spectrometry,[34-35] and computational simulated spectra.[36]

Based on the belief that PAHs are the source of the DIBs, this group of molecules constitutes one of the largest groups of molecules in the ISM, accounting for anywhere from 5% up to 20% of interstellar carbon.[37-39] PAHs make up a large group of molecules therefore many theories have arisen to attempt to narrow in on a smaller subset of molecules. Some research points at only larger, condensed PAHs ($> C_{50}$) being present due to their stability.[40-41] However, there is research which may indicate the presence of naphthalene and anthracene molecules, in addition to the larger species.[28, 42] The PAHs are predominantly pericondensed (carbon atoms shared between more than two rings) due to their superior stability and improved electron delocalization as compared to catacondensed molecules (linear ring arrangement).[41] Initially, there was also some uncertainty over the charge state of the PAHs, due in part to the limited data collected on charged PAHs. The current consensus is that a mixture of neutral and charged (both cationic and anionic) PAHs must be present as there are features found in the DIBs which coincide with both groups.[42-43]

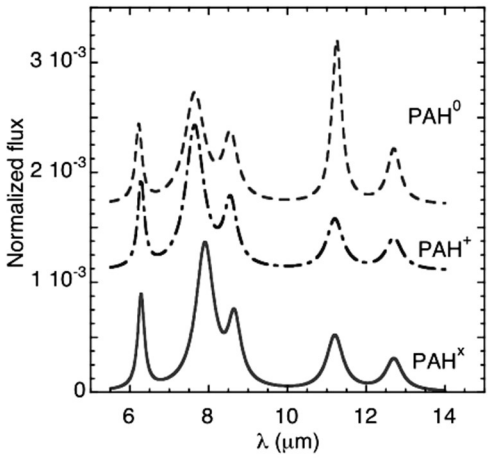

Figure 4: Spectra showing the intensity differences between neutral (dashed line) cationic (dash dot line) and anionic (solid line) PAHs in the wavelength region of the DIBs.[44]

This indicates that there is still a lot of research to be done to hone in on a specific subset of "interstellar PAHs" but due to the nature of the DIBs, this will be difficult to achieve as many combinations of PAHs can result in similar spectra.[45]

If PAHs are present in the ISM in such large quantities, the next question must be how they are formed. Of all the molecules which have been positively identified to date, PAHs are more complex than all of them with the exception of fullerenes.[2] One method put forward is their formation around carbon-rich stars which have all the necessary ingredients for PAH formation; high gas density, fast collision rate and aliphatic hydrocarbons to react.[46] The PAHs would then be ejected into the ISM at large, which is a very slow process, the absence of large PAH populations around young stars supports this theory.[47] While this is the current theory, there have been many possibilities put forward in the last 30 years. One such theory is if PAHs were synthesized in the diffuse or dense molecular clouds via ion-molecule reactions between propyne and similar hydrocarbon units, or with the addition of acetylene molecules.[48] These techniques are all bottom up methods, where the

PAHs are built by small fragments; top down method has also been considered, such as collisions between carbonaceous grains.[49]

The final question to ask is, now that we have an idea of how PAHs may be formed and in what quantities, why do we study them? Aside from finally determining the source of the DIBs, and identifying more interstellar species, PAHs may serve an important role in the chemistry of the ISM. One theory suggests that PAHs are a source of photoelectric heating. Photoelectric heating consists of the absorbance of UV radiation by species (PAHs, dust grains etc) and the kinetic energy of ejected electrons heating the surrounding gases. Heating is achieved by the increase in translational energy of the surrounding molecules thus increasing their thermal motion. Depending on the charge state of the PAHs (neutral or positively charged) they will have either a constructive or destructive effect on the heating efficiency; either way their presence has a major role in the process.[50] Another proposal suggests that PAHs might play a role as a catalyst for the formation of H_2. H_2 is the most abundant of interstellar molecules, and its concentration defines the difference between atomic and molecular clouds. Gas phase formation of H_2 is very inefficient and thus there has been extensive research in attempting to determine alternate routes to its synthesis.[51] One method is H atom adsorption on the PAH cations via the following reactions,

$$PAH^+ + H \rightarrow [PAH^+ + H] \tag{1.2}$$

$$[PAH^+ + H] + H \rightarrow PAH^+ + H_2 \tag{1.3}$$

or similar process where a dehydrogenated PAH cation gets hydrogenated and then a second H atom dehydrogenates the PAH^+ again and forms H_2.[52] Due to H atoms being the dominant species in the ISM, these reactions are fast and pressure isn't a consideration. The

study of reactions such as these gives an example of another reason to study PAHs, and the purpose of this thesis, modelling interstellar PAHs. In order to determine the validity of these reactions, and to simulate any dynamics of PAHs in interstellar environments, computational models play a vital role as they are the best way to investigate the extreme conditions presented in section 1.1. The rates and energetic of formation of each of the species in equations 1.1 and 1.2 are needed to test the theory.

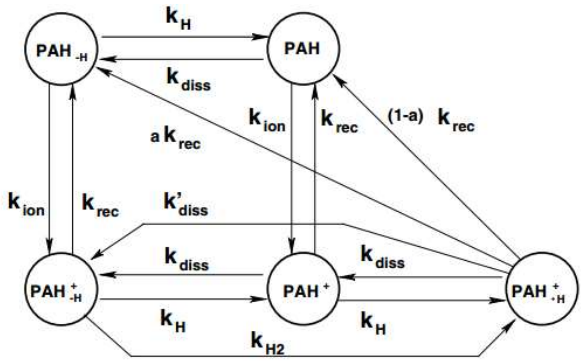

Figure 5: Mechanism used to model H_2 formation with all applicable rate constants labeled.[52]

All the rate constants, and the thermodynamic variables affiliated with them, outlined in Figure 5, need to be determined before the model can be used. Much research, like that presented here, has been focused on providing as much of this information as possible to improve and expand upon the data available for these and many other models concerned with the role of PAHs in the ISM.

1.4 The Use of Prototype Systems

While the exact identity of the PAHs present in the ISM has been up for some debate, it seems to be agreed that large PAHs (>C_{50}) are likely present.[28, 40-41] A large number of the

laboratory studies are focused on the smaller examples, whose presence in the ISM is not as certain.[53-54] The use of the smaller PAHs as a prototype system for the larger molecules seems to be an accepted practice in the field of astrochemistry, especially in investigating the energetics. [55-57] There are many reasons for this but the two main ones are quite simple, availability and ease of use. For energetics experiments, such as mass analysed kinetic energy spectrometry (MIKES) and photoelectron photoion coincidence spectroscopy (PEPICO) samples must be pure.[56, 58-60] This means that the samples which can be studied must be available for purchase with a high degree of purity. In most cases, as the number of carbon atoms increase in PAHs, the number of isomers also increases.[61] An exception to this would be molecules such as ovalene ($C_{32}H_{14}$) which due to its low H content it is unique.[62] This makes getting a pure sample much more difficult and expensive as costly separation methods would be required.[63-64] Small PAHs have no such limitations and are readily available. The next limitation is again a size effect, vapour pressure. As PAHs increase in mass, their vapour pressure decreases.[65] The experimental setups discussed above both rely on passive sample introduction, which in turn relies on the vapour pressure. Small PAHs do not suffer from this problem as many of them sublimate readily at room temperature. As will be seen in the body of this thesis, the energetic results for the smaller PAHs yield more reliable results which makes them not only easier to work with but more valuable for learning of the possible energetic profile of PAHs of all sizes.

1.5 References for Chapter 1

1. Hartquist, T. W.; Williams, D. A.; Williams, D. A., *The Molecular Astrophysics of Stars and Galaxies*. Clarendon Press: 1998.

2. Herbst, E., Three Milieux for Interstellar Chemistry: Gas, Dust, and Ice. *PCCP* **2014,** *16*, 3344-3359.

3. Krätschmer, W., Fullerenes, Carbon Chains, and Interstellar Matter. *Fullerenes, Nanotubes and Carbon Nanostructures* **2013,** *22*, 23-34.

4. Cami, J.; Bernard-Salas, J.; Peeters, E.; Malek, S. E., Detection of C60 and C70 in a Young Planetary Nebula. *Sci* **2010,** *329*, 1180-1182.

5. Sellgren, K., Aromatic Hydrocarbons, Diamonds, and Fullerenes in Interstellar Space: Puzzles to Be Solved by Laboratory and Theoretical Astrochemistry. *Spectrochimica Acta Part A: Molecular and Biomolecular Spectroscopy* **2001,** *57*, 627-642.

6. Joblin, C.; Tielens, A. G. G. M., *Pahs and the Universe: A Symposium to Celebrate the 25th Anniversary of the Pah Hypothesis*. EAS Publications Series: 2011; Vol. 46.

7. Barry, R. G.; Chorley, R. J., *Atmosphere, Weather, and Climate*. 8 ed.; Routledge: New York, New York, 2003.

8. Snow, T. P.; McCall, B. J., Diffuse Atomic and Molecular Clouds. *ARA&A* **2006,** *44*, 367-414.

9. Shematovich, V. I., Formation of Complex Chemical Species in Astrochemistry (a Review). *SoSyR* **2012,** *46*, 391-407.

10. Herbst, E., Chemistry in the Interstellar Medium. *Annu. Rev. Phys. Chem.* **1995,** *46*, 27-53.

11. Köppel, C.; Schwarz, H.; Bohlmann, F., Elektronenstossinduzierte Fragmentierung Von Acetylenverbindungen. Ix—Struktur Der Stabilen [C9H11]+-Ionen Aus Isomeren C9H11-Chloriden. *Org. Mass Spectrom.* **1974,** *9*, 321-323.

12. Fujiwara, K.; Harada, A.; Aihara, J.-i., Ch Bond Dissociation Energies of Polycyclic Aromatic Hydrocarbon Molecular Cations: Theoretical Interpretation of the (M-1)+ Peak in the Mass Spectra. *J. Mass Spectrom.* **1996,** *31*, 1216-1220.

13. West, B.; Useli-Bacchitta, F.; Sabbah, H.; Blanchet, V.; Bodi, A.; Mayer, P. M.; Joblin, C., Photodissociation of Pyrene Cations: Structure and Energetics from C16h10+ to C14+ and Almost Everything in Between. *J. Phys. Chem. A* **2014**.

14. Fischer, K. H.; Schneider, M.; Fischer, I.; Pfaffinger, B.; Braunschweig, H.; Sztáray, B.; Bodi, A., Bonding in a Borylene Complex Investigated by Photoionization and Dissociative Photoionization. *Chemistry – A European Journal* **2012,** *18*, 4533-4540.

15. Hemberger, P.; Bodi, A.; Gerber, T.; Würtemberger, M.; Radius, U., Unimolecular Reaction Mechanism of an Imidazolin-2-Ylidene: An Ipepico Study on the Complex Dissociation of an Arduengo-Type Carbene. *Chemistry – A European Journal* **2013,** *19*, 7090-7099.

16. Peeters, E.; Cami, J., Polycyclic Aromatic Hydrocarbons. In *Encyclopedia of Astrobiology*, Gargaud, M.; Amils, R.; Quintanilla, J.; Cleaves, H., II; Irvine, W.; Pinti, D.; Viso, M., Eds. Springer Berlin Heidelberg: 2011; pp 1307-1321.

17. Geballe, T., Highlights of Infrared Spectroscopy of the Interstellar Medium at Ukirt. In *Thirty Years of Astronomical Discovery with Ukirt*, Adamson, A.; Davies, J.; Robson, I., Eds. Springer Netherlands: 2013; Vol. 37, pp 159-172.

18. McCall, B. J.; Drosback, M. M.; Thorburn, J. A.; York, D. G.; Friedman, S. D.; Hobbs, L. M.; Rachford, B. L.; Snow, T. P.; Sonnentrucker, P.; Welty, D. E., Studies of the Diffuse Interstellar Bands. Iv. The Nearly Perfect Correlation between Λλ6196.0 and 6613.6. *The Astrophysical Journal* **2010,** *708*, 1628.

19. Snow, T. P.; Bierbaum, V. M., Ion Chemistry in the Interstellar Medium. *Annual Review of Analytical Chemistry* **2008,** *1*, 229-259.

20. Wheeler, R. A., *Annual Reports in Computational Chemistry*. Elsevier Science: 2011.

21. Sivaraman, B.; Nair, B. G.; Lo, J.-I.; Kundu, S.; Davis, D.; Prabhudesai, V.; Sekhar, B. N. R.; Mason, N. J.; Cheng, B.-M.; Krishnakumar, E., Vacuum Ultraviolet and Infrared Spectra of Condensed Methyl Acetate on Cold Astrochemical Dust Analogs. *The Astrophysical Journal* **2013,** *778*, 157.

22. Zack, L.; Maier, J., Laboratory Electronic Spectra of Carbon Chains and Rings. *Proceedings of the International Astronomical Union* **2013,** *9*, 237-246.

23. Nuevo, M. In *Laboratory Astrochemistry: A Powerful Tool to Understand the Origin of Organic Molecules in the Interstellar Medium, Comets, and Meteorites*, New Horizons in Astronomy, Proceedings of the Frank N. Bash Symposium 2011, held October 9-11, 2011. Austin, Texas, USA. Edited by S. Salviander, J. Green, and A. Pawlik. Published online at http://pos.sissa.it/cgi-bin/reader/conf.cgi? confid= 149., id. 4, 2011; p 4.

24. Bierbaum, V. M., Laboratory Studies of Ion Chemistry in the Interstellar Medium. *Proceedings of the International Astronomical Union* **2013,** *9*, 258-264.

25. Herbst, E., The Chemistry of Interstellar Space. *Chem. Soc. Rev.* **2001,** *30*, 168-176.

26. Gerlich, D., Experimental Investigations of Ion–Molecule Reactions Relevant to Interstellar Chemistry. *J. Chem. Soc., Faraday Trans.* **1993,** *89*, 2199-2208.

27. Fortenberry, R., Theoretical and Computational Studies of Interstellar C2nH and SiC2m.

28. Salama, F.; Galazutdinov, G. A.; Krełowski, J.; Biennier, L.; Beletsky, Y.; Song, I.-O., Polycyclic Aromatic Hydrocarbons and the Diffuse Interstellar Bands: A Survey. *ApJ* **2011,** *728*, 154.

29. McCall, B. J.; Griffin, R. E., On the Discovery of the Diffuse Interstellar Bands. *Proceedings of the Royal Society A: Mathematical, Physical and Engineering Science* **2013,** *469*.

30. Salama, F.; Bakes, E. L. O.; Allamandola, L. J.; Tielens, A. G. G. M., Assessment of the Polycyclic Aromatic Hydrocarbons -- Diffuse Interstellar Band Proposal. *ApJ* **1996,** *458*, 621-636.

31. Allamandola, L. J.; Tielens, A. G. G. M.; Barker, J. R., Infrared Emission from Interstellar Pahs. In *Physical Processes in Interstellar Clouds*, Morfill, G. E.; Scholer, M., Eds. Springer Netherlands: 1987; Vol. 210, pp 305-331.

32. Hendecourt, L.; Joblin, C.; Jones, A., *Solid Interstellar Matter: The Iso Revolution ; Les Houches Workshop, February 2-6, 1998*. Springer: 1999.

33. Oomens, J.; et al., Laboratory Infrared Spectroscopy of Cationic Polycyclic Aromatic Hydrocarbon Molecules. *The Astrophysical Journal* **2003,** *591*, 968.

34. Spencer, M. K.; Hammond, M. R.; Zare, R. N., Laser Mass Spectrometric Detection of Extraterrestrial Aromatic Molecules: Mini-Review and Examination of Pulsed Heating Effects. *Proceedings of the National Academy of Sciences* **2008,** *105*, 18096-18101.

35. Knorke, H.; Langer, J.; Oomens, J.; Dopfer, O., Infrared Spectra of Isolated Protonated Polycyclic Aromatic Hydrocarbon Molecules. *The Astrophysical Journal Letters* **2009,** *706*, L66.

36. Cook, D. J.; Saykally, R. J., Simulated Infrared Emission Spectra of Highly Excited Polyatomic Molecules: A Detailed Model of the PAH-UIR Hypothesis. *The Astrophysical Journal* **1998,** *493*, 793.

37. Vuong, M. H.; Foing, B. H., Dehydrogenation of Polycyclic Aromatic Hydrocarbons in the Diffuse Interstellar Medium. *arXiv preprint astro-ph/0010385* **2000**.

38. Joblin, C., Pahs in the Interstellar Carbon Cycle: The Experimental View of PIRENEA. In *The Dense Interstellar Medium in Galaxies*, Pfalzner, S.; Kramer, C.; Straubmeier, C.; Heithausen, A., Eds. Springer Berlin Heidelberg: 2004; Vol. 91, pp 517-520.

39. Thrower, J. D.; Jørgensen, B.; Friis, E. E.; Baouche, S.; Mennella, V.; Luntz, A. C.; Andersen, M.; Hammer, B.; Hornekær, L., Experimental Evidence for the Formation of Highly Superhydrogenated Polycyclic Aromatic Hydrocarbons through H Atom Addition and Their Catalytic Role in H2 Formation. *The Astrophysical Journal* **2012,** *752*, 3.

40. Tielens, A. G. G. M., Interstellar Polycyclic Aromatic Hydrocarbon Molecules*. *ARA&A* **2008,** *46*, 289-337.

41. *Crawford, M. K. T., A. G. G. M.*, Ionized Polycyclic Aromatic Hydrocarbons and the Diffuse Interstellar Bands. *The Astrophysical Journal* **1985,** *293*, L45-L48.

42. Snow, T. P.; Le Page, V.; Keheyan, Y.; Bierbaum, V. M., The Interstellar Chemistry of PAH Cations. *Natur* **1998,** *391*, 259.

43. Allamandola, L. J.; Hudgins, D. M.; Sandford, S. A., Modeling the Unidentified Infrared Emission with Combinations of Polycyclic Aromatic Hydrocarbons. *The Astrophysical Journal Letters* **1999,** *511*, L115.

44. Joblin, C.; Berne, O.; Simon, A.; Mulas, G. In *Laboratory Studies of Polycyclic Aromatic Hydrocarbons: The Search for Interstellar Candidates*, Cosmic Dust–Near and Far, Heidelberg (Germany), Henning, T.; Grün, E.; Steinacker, J., Eds. Astronomical Society of the Pacific: Heidelberg (Germany), 2008; pp 1-20.

45. Rosenberg, M. J.; Berné, O.; Boersma, C., Random Mixtures of Polycyclic Aromatic Hydrocarbon Spectra Match Interstellar Infrared Emission. *arXiv preprint arXiv:1405.5383* **2014**.

46. Lebouteiller, V.; Bernard-Salas, J.; Whelan, D. G.; Brandl, B.; Galliano, F.; Charmandaris, V.; Madden, S.; Kunth, D., Influence of the Environment on Polycyclic Aromatic Hydrocarbon Emission in Star-Forming Regions. *The Astrophysical Journal* **2011,** *728*, 45.

47. Galliano, F.; Madden, S. C.; Tielens, A. G. G. M.; Peeters, E.; Jones, A. P., Variations of the Mid-Ir Aromatic Features inside and among Galaxies. *The Astrophysical Journal* **2008,** *679*, 310.

48. Bohme, D. K., Pah [Polycyclic Aromatic Hydrocarbons] and Fullerene Ions and Ion/Molecule Reactions in Interstellar and Circumstellar Chemistry. *Chem. Rev.* **1992,** *92*, 1487-1508.

49. Seok, J. Y.; Hirashita, H.; Asano, R. S., Formation History of Polycyclic Aromatic Hydrocarbons in Galaxies. *arXiv preprint arXiv:1401.3943* **2014**.

50. Okada, Y.; Pilleri, P.; Berné, O.; Ossenkopf, V.; Goicoechea, J. R.; Joblin, C.; Kramer, C.; Röllig, M.; Teyssier, D.; van der Tak, F. F., Probing the Role of Polycyclic Aromatic Hydrocarbons in the Photoelectric Heating within Photodissociation Regions. *arXiv preprint arXiv:1303.2030* **2013**.

51. Vidali, G., H2 Formation on Interstellar Grains. *Chem. Rev.* **2013,** *113*, 8762-8782.

52. Page, V. L.; Snow, T. P.; Bierbaum, V. M., Molecular Hydrogen Formation Catalyzed by Polycyclic Aromatic Hydrocarbons in the Interstellar Medium. *The Astrophysical Journal* **2009,** *704*, 274.

53. Rastogi, S., Polycyclic Aromatic Hydrocarbons in Stellar Medium. *BASI* **2005,** *33*, 167-174.

54. Swamy, K. S. K., *Dust in the Universe: Similarities and Differences*. World Scientific: 2005.

55. Jochims, H. W.; Baumgärtel, H.; Leach, S., Structure-Dependent Photostability of Polycyclic Aromatic Hydrocarbon Cations: Laboratory Studies and Astrophysical Implications. *The Astrophysical Journal* **1999,** *512*, 500.

56. Lifshitz, C., Energetics and Dynamics through Time-Resolved Measurements in Mass Spectrometry: Aromatic Hydrocarbons, Polycyclic Aromatic Hydrocarbons and Fullerenes. *Int. Rev. Phys. Chem.* **1997,** *16*, 113-139.

57. Ricca, A.; Bakes, E. L. O.; Bauschlicher, C. W., The Energetics for Hydrogen Addition to Naphthalene Cations. *The Astrophysical Journal* **2007,** *659*, 858.

58. Ling, Y.; Lifshitz, C., Time-Dependent Mass Spectra and Breakdown Graphs. 21. C14h10 Isomers. *J. Phys. Chem. A* **1998,** *102*, 708-716.

59. West, B.; Joblin, C.; Blanchet, V.; Bodi, A.; Sztáray, B.; Mayer, P., The Dynamics of Hydrogen and Methyl Radical Loss from Ionized Dihydro-Polycyclic Aromatic Hydrocarbons: A Tandem Mass Spectrometry and Imaging-Pepico Study of Dihydronaphthalene and Dihydrophenanthrene. *J. Phys. Chem. A* **2014,** *118*, 1807-1816.

60. West, B.; Joblin, C.; Blanchet, V.; Bodi, A.; Sztáray, B.; Mayer, P. M., On the Dissociation of the Naphthalene Radical Cation: New iPEPICO and Tandem Mass Spectrometry Results. *J. Phys. Chem. A* **2012,** *116*, 10999-11007.

61. Fetzer, J. C., *Large (C = 24) Polycyclic Aromatic Hydrocarbons: Chemistry and Analysis*. Wiley: 2000.

62. NIST, *Nist Chemistry Webbook, Nist Standard Reference Database*. National Institute of Standards and Technology: Gaithersburg MD, 20899, Vol. Number 69, March 2003.

63. Dunn, B. P.; Armour, R. J., Sample Extraction and Purification for Determination of Polycyclic Aromatic Hydrocarbons by Reversed-Phase Chromatography. *Anal. Chem.* **1980,** *52*, 2027-2031.

64. Fetzer, J. C., The Chemistry and Analysis of Large PAHs. *Polycyclic Aromat. Compd.* **2007,** *27*, 143-162.

65. Shimmo, M.; Saarnio, K.; Aalto, P.; Hartonen, K.; Hyötyläinen, T.; Kulmala, M.; Riekkola, M.-L., Particle Size Distribution and Gas-Particle Partition of Polycyclic Aromatic Hydrocarbons in Helsinki Urban Area. *JAtC* **2004,** *47*, 223-241.

2. Experimental Methods

2.1. Modified reverse geometry three sector instrument

All the mass spectrometry (MSMS) experiments conducted at the University of Ottawa, with the exception of the APCI-CID experiments conducted with anthracene, were performed on a modified VG-ZAB mass spectrometer, sketched in Figure 6.

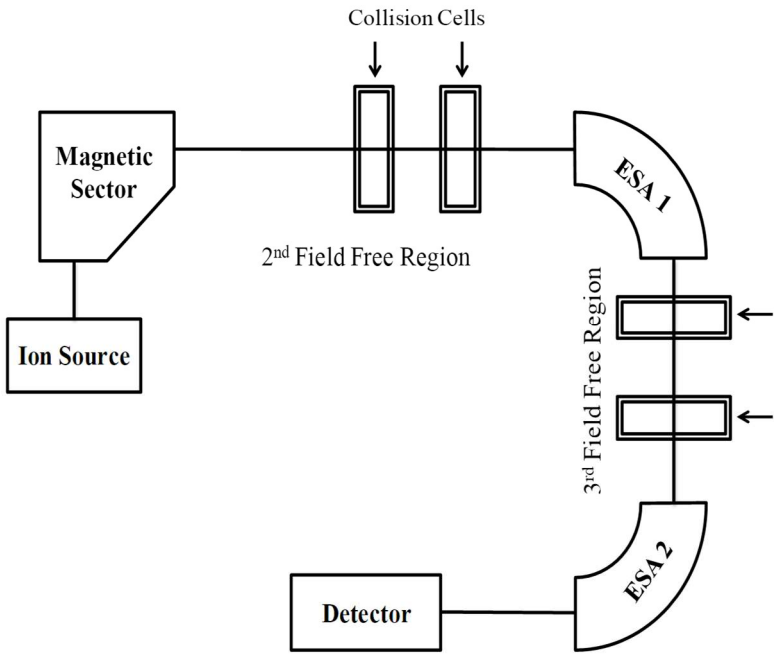

Figure 6: Schematic representation of modified VG-ZAB instrument.

Each component will be described individually and its purpose in each of the various experiments will be explained. In brief, the ions are generated via electron ionization (EI) and accelerated towards the magnetic sector when the ions are separated by mass. Once the desired ions are selected, they pass through the second field free region (2FFR) where,

depending on the experiment, a neutral gas may be introduced to induce fragmentation. From here, the ions and fragments are either detected or selected in the first electrostatic analyzer (ESA) based on their kinetic energy. In the case of Tandem MS experiments, the ion selected in ESA1 will travel through the third field free region (3FFR) where it is collided with a neutral target gas to induce further fragmentation. The fragments are then detected based on their kinetic energy in ESA2.

The first component of the VG-ZAB is the ion source. The neutral molecules are introduced in one of two ways depending on their physical state at room temperature. The majority were solid samples and thus were introduced using a heated solid probe. The sample could be heated slightly to encourage sublimation if necessary. In the case of liquid samples, such as DHN, a liquid inlet was used as a means to introduce the molecules to the source. A schematic representation of the ion source is provided in Figure 7.

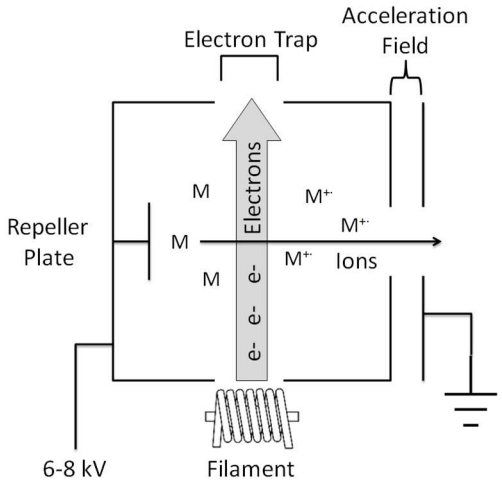

Figure 7: Schematic representation of electron impact ion source.

Electrons were ejected from the metal filament through thermal emission from a wire filament. The resulting electron beam possesses approximately 80 eV of energy. This energy is close to the accepted peak efficiency of 70 eV.[1] The electron beam is directed through the molecular cloud due to the attraction towards the electron trap. The molecules are ionized via the following reaction,

$$M + e^- \rightarrow M^{+\bullet} + 2e^- \qquad (2.1)$$

The radical cations are then accelerated out of the source housing at a speed corresponding to the energy difference between the housing and the grounded plate immediately outside, the energies used are either 6, 7 or 8 kV depending on the timescale desired for the experiment.

After the ions are formed, they travel briefly through a field free region before being entering the magnetic sector where the ion of choice is selected based on its momentum using the magnetic field. Figure 8 shows how selection is achieved based on a test case where there is a mixture of three different ions.

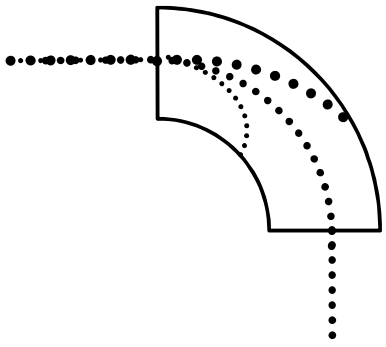

Figure 8: Diagram of magnetic sector showing mass selection.

The magnetic sector consists of two, parallel, curved electromagnets with a gap between them where the ions will travel. The electromagnets create a magnetic field between them which can separate the ions based on their momentum; the momentum of the ions and the magnetic field are related according to the formula,

$$mv = rBze \tag{2.2}$$

where mv is the momentum of the ion, r is the radius of curvature of the magnetic sector, B is the magnetic field, z is the charge of the ion, and e is the elementary charge.[1] The radius is a fixed value which means that the only variable that can be controlled is the magnetic field. If the momentum of the desired ion is known, it is possible to fix the magnetic field so that only the selected ion can successfully traverse the curved trajectory. The velocity of the ion is related to the acceleration voltage (V) by,

$$zeV = \tfrac{1}{2}\, mv^2 \tag{2.3}$$

The mass to charge ratio (m/z) of the selected ion can be obtained by combining equations (2.2) and (2.3),

$$\frac{m}{z} = \left(\frac{B^2 r^2 e}{2V}\right) \tag{2.4}$$

The selected ions are now allowed to travel through 2FFR. This region, as well as 3FFR, is equipped with collisions cells which consist of 2-3 cm steel boxes with slits cut into both end plates to allow the ion beam to travel though. The collision cells can be filled with a neutral gas, monitored via an ion gauge, to perform collision experiments.

The next two components of the sector instrument to be discussed are the electrostatic analyzers, ESA1 and ESA2. The ESA sectors consist of two curved metal plates with a consistent gap between them.

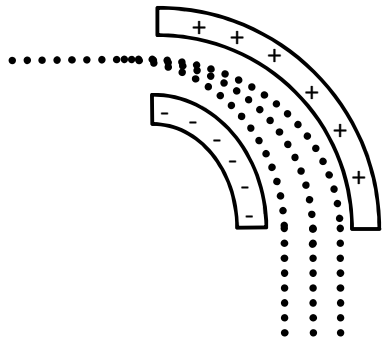

Figure 9: Graphical representation of electrostatic analyzer

Each plate is held at a different potential, thus an electric field is induced across this gap to separate the ions based on their kinetic energy. Separation is achieved using the following equation,

$$\frac{1}{2}mv^2 = zeV = \frac{1}{2}zeEr \tag{2.5}$$

where E represents the electric field. This equation can be rearranged in order to define the ion based on its *m/z*,

$$\frac{m}{z} = \frac{eEr}{v^2} \tag{2.6}$$

The electric field can either be fixed, to have the ESA act as a mass selector, or scanned to behave as a mass filter.

The final component of the sector instrument is the detector. The VG-ZAB instrument uses a photomultiplier detector, depicted in Figure 10.

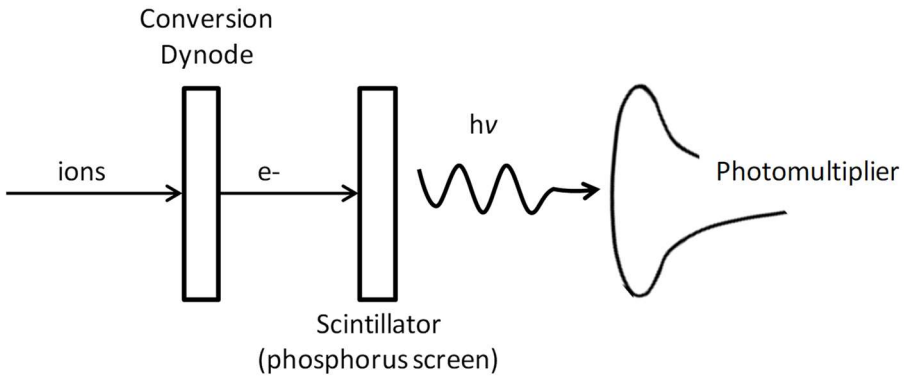

Figure 10: Schematic of photomultiplier detector

The ions collide with the conversion dynode, which in turn releases an electron. This electron collides with a scintillator, which converts that electron into a photon. The photon travels into a photomultiplier where the signal is amplified by using several dynodes. As the ESA is scanned, the different ions will be selected so and the detector measures the intensity of the ion count.

2.1.1. Mass-analyzed Ion Kinetic Energy Spectrometry

All experiments performed on the VG-ZAB start out identically. The ions are created in the source and are accelerated to 6, 7 or 8 kV, depending on what time scale is desired for the experiment. The ionization process is quite hard, thus many fragments are made alongside the precursor ion, and so the magnetic sector is needed to filter out only the desired ion. Once the ion of choice has been mass selected, it travels into the 2FFR. This is the point where the experiments branch off. MIKES experiments rely on the spontaneous

dissociation of metastable ions, those which possesses sufficient internal energy to dissociate within the dissociation region without any assistance (i.e. no collisions).[2]

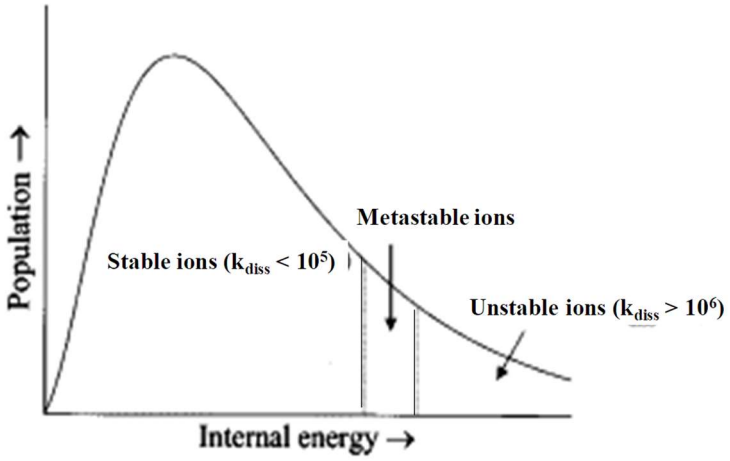

Figure 11: Graphical representation of how metastable ions compare to stable and unstable ions.[3]

As can be seen in Figure 11, there is a very small window of internal energies which meet this criteria and the majority of the ion population is in the "stable ion" region.[3] For this reason, very little of the metastable ions are ever generated so the signal is quite low compared to the stable ions. During a MIKES experiment, the metastable ions dissociate in the 2FFR and their fragments, along with the remaining precursor ions, are detected by scanning ESA1. The experiment is then repeated using a different acceleration voltage so that the branching ratios for the various fragments can be compared.

2.1.2. Collision Induced Dissociation

As stated in the previous section, the ions are generated and mass selected in the magnetic sector in exactly the same way as for a MIKES experiment. In this case, the

acceleration voltage used is only 8 kV to get the best fragmentation yield. Other than that, the main difference between the two methods is that in a CID experiment, a neutral collision gas is introduced in the collision cell in the 2FFR. The collision gas, in this work helium was the only gas used, induces further fragmentation than spontaneous dissociation alone. When the mass selected ion collides with the helium atom, the collision causes an increase in the internal energy of the ion, which may cause dissociation if the energy is sufficiently high. This process is more efficient than metastable ion decomposition because, statistically, there is a greater chance of inducing dissociation as there are far more stable ions than metastable ones.[3] For this reason, not only are the dissociation channels found for metastable ions more populated, but new channels can also be accessed. Once the ions have been fragmented, the fragments and remaining precursor ion can again be detected by scanning ESA1. CID is used primarily as a method for the determination of the structure of the precursor ion.

2.1.3. Metastable Ion Collision Induced Dissociation

MI-CID is a combination of the two previous techniques, MIKES and CID. Again, the ions are generated and selected in the magnetic sector in the same way as the previous two experiments. Like with CID, only 8kV was used as an acceleration voltage to maximize the amount of metastable ions. The 2FFR remains free of collision gas to allow for metastable ion dissociation. Instead of scanning ESA1 to detect all the fragments, it is held fixed to select one of the fragment ions. This ion is permitted through to the 3FFR. Here, helium is added to one of the collision cells to induce further dissociation. For detection of the fragments and remaining precursor ion, ESA2 can be scanned to detect them based on

their kinetic energy. This process allows for the determination of the structure of the metastably-generated fragments. This process is helpful in determining if there is a difference in the structure of these ions with those produced using more energetic means, to determine if there is any rearrangement which occurs. A limitation to this method is that, since few metastable ions are present, there is very little ion flux which reaches the 3FFR, as not all the ions will produce a specific fragment; only the most intense fragments can be selected for these experiments.

2.2. Imaging Photoelectron Photoion Coincidence Spectroscopy

All the iPEPICO experiments were conducted at the Swiss Light Source (SLS) (Villigen, Switzerland). The experimental setup is shown in Figure 12.

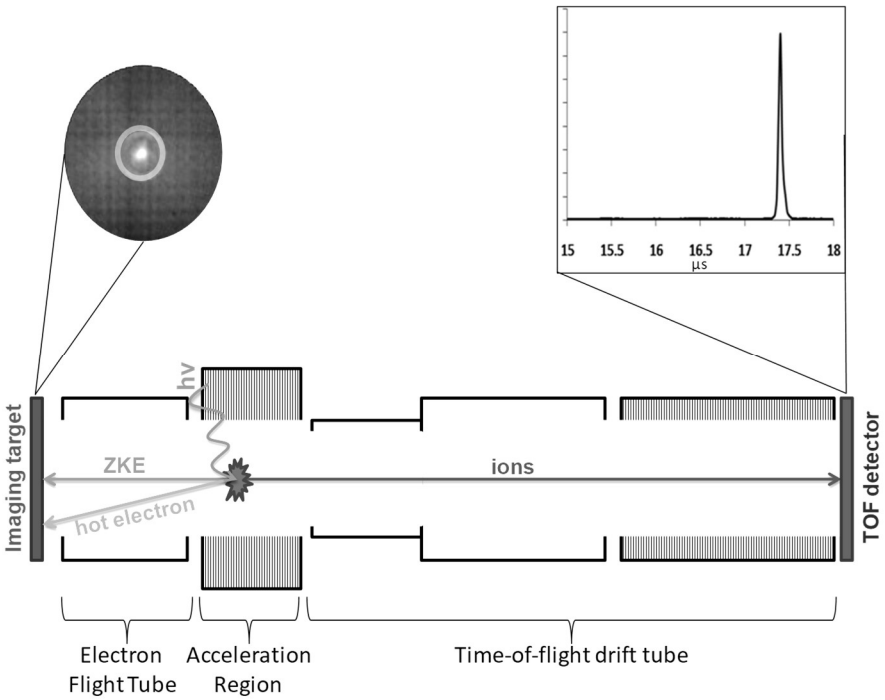

Figure 12: schematic representation of iPEPICO apparatus.

The iPEPICO apparatus consists of three main components which will be discussed: the ionization and acceleration region, the electron flight tube and detector and the time-of-flight (TOF) mass spectrometer.

The iPEPICO experiment relies on knowing the internal energy of the ion (E_{ion}) within a very small margin. This is accomplished from the following formula,

$$h\nu = IE_{adia} + E_{ion} + KE \tag{2.7}$$

where $h\nu$ is the ionizing photon energy, IE_{adia} is the adiabatic ionization energy and KE is the kinetic energy of the electron.

If a sample is sufficiently volatile, as was the case with all samples discussed here, they are introduced to the source chamber via a room temperature effusion source; from here they are bled into the ionization area (within the acceleration region) through a 5mm opening or, if there is need to reduce the pressure, a skimmer cone. Once the sample is introduced, synchrotron radiation is used for photoionization. Vacuum ultraviolet (VUV) radiation, wavelengths between 10-200 nm, was collimated and passed through one of two silicon gratings, depending on the energy range needed; 600 mm^{-1} line density is used to access 5 – 15 eV and 1200 mm^{-1} to access 15 – 30 eV energies.[4] The light is passed through a gas filter, 10 mbar of either a 75:25 mixture of N_2: Ar or pure N_2, to filter out harmonics above 15.759 eV and 21.565 eV respectively.[5] The photon energy resolution is on the order of 10^4 (1meV at 10 eV photon energy) which is precise enough for the calculation of E_{ion}. Once the sample is ionized, the electron is extracted towards the imaging target while the ions travel into the TOF.

In this type of experiment, the only way to know the kinetic energy of the ejected electron is if it is a threshold electron, thus having no (or as close to it as possible) kinetic energy. When an ion is generated, both the ion and the electron are accelerated in opposing directions (40– 80 V cm^{-1} field strength).[5] In the case of the electron, it is both position and time stamped. Threshold electrons collide with the center of the target while the majority of the energetic electrons, referred to as hot electrons, will collide outside the center spot. An example of how the target looks after an experiment is shown in Figure 12. As there will be some hot electrons which coincidentally have the correct trajectory to strike the center of the target, a ring just outside of the center spot is subtracted from the center signal. The imaging detector consists of microchannel plates (MCPs). MCPs function by multiplying the electron signal as it travels down the channel. The two MCPs in this detector are in a chevron configuration with an 8° angel between the two plates. This allows for further signal magnification as illustrated in Figure 13.

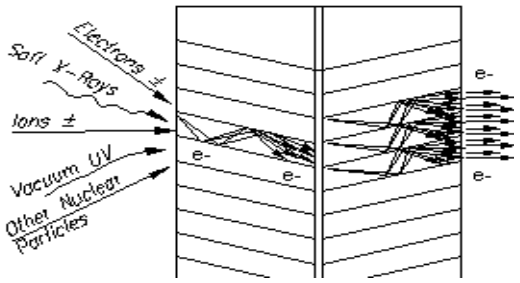

Figure 13: Illustration of signal enhancement in chevron MCP.[6]

Each MCP consists of an array of electron multipliers, each electron produces a secondary electron at every collision with the sides of the channel; this cascade is repeated numerous times. The advantage to a chevron configuration is that when the electrons leave the first

MCP and enter then next, there is a bit of diffusion and multiple channels on the second plate receive electrons to increase the signal further. This does cause a small reduction in the image resolution but the result is simply the need to sample a larger center spot for the threshold electrons. Now that the electron has been detected, and its position known, the signal from the MCP acts as the start time for the TOF flight time for the ions.

Time of flight is one of the simpler mass analyzers. They work on the understanding that fragments with the same energy but different masses will have different velocities. Using the physics relationship the velocity can be expressed as,

$$v = \sqrt{\frac{2KE}{m}} \tag{2.8}$$

The iPEPICO apparatus accelerates the fragments within an electric field, thus their kinetic energies are the same. As they drift down the field free drift tube, which is 550 mm in length, the smaller ions will drift faster than heavier fragments thus as they travel there will be a time separation. As each fragment arrives at the detector, another MCP, their arrival time is recorded which acts as the 'stop' signal. The time delay between the arrival of the electron at the imaging target and the detection of the fragment gives the flight time for the fragment. Only fragments which are the product of ions made with threshold electrons, fragments measured in coincidence with the threshold electrons, are analyzed; the remaining signals are discarded.

2.2.1. iPEPICO experimental setup

As stated, in an iPEPICO experiment, ions are generated via photoionization with VUV light generated by synchrotron radiation. The ejected electron will be directed back towards the electron target where it will be time and positioned stamped. This signal is the 'start' for the TOF detector. The ions, either precursor or fragments depending on the photon energy used for ionization, will travel through the TOF MS where they will be detected upon their arrival; this is the 'stop' signal so that each time can be measured. This experiment is repeated many times at a range of photon energies to generate unimolecular breakdown diagrams which will be fit using RRKM theory. It should be noted that by the very nature of the experiment, there is a low ion flux which necessitates a longer acquisition time at each energy in order to gather enough intensity to get good signal to noise.

2.3. Computational Methods

2.3.1. Density Functional Theory

Density functional theory (DFT) is a computational method for the calculation of molecular structures and energies based, not on the wavefunction, but on the electron density of the molecule.[7] This allows for more rapid calculations, compared to the more expensive *ab initio* methods, while giving results which are comparable to them. Regardless of the molecule size, DFT calculations only need to consider three variables $\rho(x, y, z)$ while the more labour intensive methods focus on the wavefunction and thus have to solve the Schrödinger equation, rapidly becoming more difficult as the molecule gets larger.[8]

As stated, one of the pieces of information that one can learn from DFT calculations is that of molecular structure. Due to the experimental conditions of the work presented here, we can consider the simplest situation of an isolated molecule without having to factor in thermal or solvent effects. Structure determination is achieved based on a gradient search; the energy is calculated from an initial guess and then the geometry undergoes minute adjustments and the process is repeated. The end result is that an optimized structure is determined within an energy minimum; depending on how close the first guess is to the final structure it can either be a local or global minimum of the potential energy surface (PES).[9] The minimum energy structures are the stable geometries. Another molecular geometry of interest is that of the transition state of a reaction. The transition state is defined as the structure associated with a saddle point of the PES.

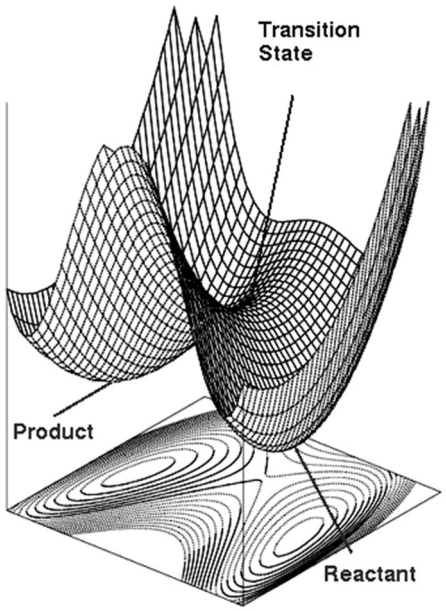

Figure 14: Representative potential energy surface with the location of reactant, transition state and product indicated.[10]

where a saddle point is defined as a stationary point, where the first derivative is zero, and its partial second derivatives give both positive and negative results (2^{nd} derivative > 0 indicates minimum while 2^{nd} derivative < 0 indicates a maximum).[11] For a transition state, the saddle point must be a maximum along only one path, that of the reaction coordinate, while it is a minimum in all other directions. Now that the optimize geometries have been defined, the energy corresponding to them must be determined.

While it is easy to visualize a molecule sitting in a minimum on the surface, like a marble falling into a divot, this is not an accurate representation as the atoms in a molecule are constantly vibrating; the minimum energy of this vibration is known as the molecule's zero point energy (ZPE).[7] This minimum energy is added to the optimized energy (the electronic energy) in order to get the real minimum energy which is used for calculating the reaction energies, such as dissociation energy (ΔE) and ionization potential (IP).

Vibrational frequencies are calculated based on the normal modes of the molecule, where all the atoms of the same type move symmetrically with the same amplitude. The number of frequencies is determined based on the degrees of freedom of the molecule with the translational and rotational degrees removed,

$$3N - 6 \text{ (non-linear)} \tag{2.9a}$$

$$3N - 5 \text{ (linear)} \tag{2.9b}$$

where N represents the number of atoms in the molecule. The calculated frequencies are typically higher in frequency than experimental therefore they need to be scaled based on an empirically determined scaling value.[12] The vibrational frequencies calculated can also be useful for confirmation of transition states. The critical frequency, that which leads the

molecule to products, will have an imaginary frequency due to the lack of restorative forces on the vibration.[7] This is the easiest way to confirm that the structure is that of the transition state, if it has more than one imaginary frequency then it is a maximum or an nth order saddle point.

The final values extracted from the DFT calculations were that of the rotational constants. These three values correspond to the three primary moments of inertia, and their energies are determined by solving the rigid rotor Schrödinger equation.

2.3.2. Rice–Ramsperger–Kassel–Marcus (RRKM) theory

All the reactions that are being discussed in this thesis are unimolecular dissociation reactions of the type,

$$A^* \xrightarrow{k} A^{\ddagger} \rightarrow P \qquad (2.10)$$

where A* is an excited molecule, k is the rate constant for the dissociation, $A^{\ddagger}$ is the transition state (TS) of A and P are the dissociation products.[13] With DFT it is possible to calculate the optimized and transition state structures, which can now be related to the experimental results. One method which has been used extensively for this purpose is RRKM theory, which calculates the rate of reactions based on calculated structures.

As stated in the introduction, the conditions in the ISM are such that all molecular and ionic species are in the gas phase at low pressures.[14] This makes calculating rate constants based on temperature, *k(T)*, impractical. RRKM calculates rate constants based on energy, *k(E)*, which was found to be a more versatile methods for calculation rate constants for most chemical systems, especially in the gas phase.[15] RRKM theory is unique in that it

includes transition state theory (TST), which makes the assumption that once the reaction reaches the transition state, or dividing surface, it will always continue to products.[16] To calculate *k(E)*, the typical formula used is as follows,[17-18]

$$k(E) = \frac{\sigma N^{\ddagger}(E-E_0)}{h\rho(E)} \quad (2.11)$$

In this equation, σ represents the degeneracy of the reaction (how many equivalent paths lead to the same product), h is Plank's constant, $\rho(E)$ is the density of rotational-vibrational (ro-vib) states of the precursor ion at an internal energy E and $N^{\ddagger}(E-E_0)$ is the sum of internal ro-vib states of the transition state at an internal energy of $(E-E_0)$ with E_0 being the 0 K activation energy. It is possible to calculate $N^{\ddagger}(E-E_0)$ and $\rho(E)$ based on the DFT calculated structures for the precursor, the vibrational frequencies and rotational constants, by using the Beyer and Swinehart direct count algorithm.[19]

2.4. References for Chapter 2

1. Moore, J. H.; Spencer, N. D., Encyclopedia of Chemical Physics and Physical Chemistry, Volumes 1 - 3. Institute of Physics: 2001.
2. Beynon, J. H.; Cooks, R. G.; Amy, J. W.; Baitinger, W. E.; Ridley, T. Y., Design and Performance of a Mass-Analyzed Ion Kinetic Energy (MIKE) Spectrometer. *Anal. Chem.* **1973,** *45*, 1023A-1031A.
3. Sleno, L.; Volmer, D. A., Ion Activation Methods for Tandem Mass Spectrometry. *J. Mass Spectrom.* **2004,** *39*, 1091-1112.
4. Johnson, M.; Bodi, A.; Schulz, L.; Gerber, T., Vacuum Ultraviolet Beamline at the Swiss Light Source for Chemical Dynamics Studies. *Nucl. Instrum. Meth. A.* **2009,** *610*, 597-603.
5. Bodi, A.; Johnson, M.; Gerber, T.; Gengeliczki, Z.; Sztaray, B.; Baer, T., Imaging Photoelectron Photoion Coincidence Spectroscopy with Velocity Focusing Electron Optics. *Rev. Sci. Instrum.* **2009,** *80*, 7.

6. Amptek http://www.amptek.com/wp-content/uploads/2013/12/ a111aray.gif. (accessed June 12th, 2014)

7. Lewars, E., *Computational Chemistry: Introduction to the Theory and Applications of Molecular and Quantum Mechanics*. Springer: 2003.

8. Kohanoff, J.; Gidopoulos, N., Density Functional Theory: Basics, New Trends and Applications. *Handbook of molecular physics and quantum chemistry* **2003,** *2*, 532-568.

9. Cramer, C. J., *Essentials of Computational Chemistry: Theories and Models*. Wiley: 2005.

10. Harvey, J. Molecular Electronic Structure - Lecture 5. http://www.chm.bris.ac.uk/pt/harvey/elstruct/hf_2.html (accessed June 3 2014).

11. Ghorpade, S. R.; Limaye, B. V., A Geometric Approach to Saddle Points of Surfaces. *Austral. Math. Soc. Gaz.* **2009,** *36*, 127-136.

12. Krishnakumar, V.; Keresztury, G.; Sundius, T.; Ramasamy, R., Simulation of Ir and Raman Spectra Based on Scaled Dft Force Fields: A Case Study of 2-(Methylthio)Benzonitrile, with Emphasis on Band Assignment. *J. Mol. Struct.* **2004,** *702*, 9-21.

13. Kim, G.-S.; Nguyen, T. L.; Mebel, A. M.; Lin, S. H.; Nguyen, M. T., Ab Initio/Rrkm Study of the Potential Energy Surface of Triplet Ethylene and Product Branching Ratios of the C(3p) + CH4 Reaction. *J. Phys. Chem. A* **2003,** *107*, 1788-1796.

14. Snow, T. P.; McCall, B. J., Diffuse Atomic and Molecular Clouds. *ARA&A* **2006,** *44*, 367-414.

15. Green, N., *Comprehensive Chemical Kinetics: Unimolecular Kinetics, Part 1. The Reaction Step*. Elsevier Science: 2003.

16. Green, W. H.; Moore, C. B.; Polik, W. F., Transition States and Rate Constants for Unimolecular Reactions. *Annu. Rev. Phys. Chem.* **1992,** *43*, 591-626.

17. Baer, T.; Hase, W. L., *Unimolecular Reaction Dynamics, Theory and Experiments*. Oxford University Press: New York, 1996.

18. Baer, T.; Mayer, P. M., Statistical Rice-Ramsperger-Kassel-Marcus Quaiequilibrium Theory Calculations in Mass Spectrometry *J. Am. Soc. Mass. Spectrom.* **1997,** *8*, 103-115.

19. Beyer, T.; Swinehart, D. R., Direct Count for RRKM. *ACM Commun.* **1973,** *16*, 379.

3. Procedures

3.1. Experimental Methods

All molecules (NAP, ANT, PYR, DHN, DHP, EB, PB, BCB and IND) were obtained from Sigma-Aldrich (Sigma-Aldrich, Oakville, Canada) and used without further purification. The sample was introduced into the modified VG ZAB mass spectrometer via either a direct insertion probe for solid samples or a liquid inlet in the case of liquid samples. It was introduced into the iPEPICO apparatus after pumping to remove air.

3.1.1. MIKES, CID and MI-CID experiments

All mass-analyzed ion kinetic energy spectrometry (MIKES), collision induced dissociation (CID) and metastable ion collision induced dissociation (MI-CID) experiments were performed on a modified VG-ZAB three sector instrument.[1] The geometry consists of a magnetic sector, followed by two electrostatic analyzers (BEE geometry) (VG Analytical, Manchester, UK.) The molecule was introduced to the source resulting in a pressure reading of ~$1x10^{-4}$ mbar which is detected by an ion gauge positioned above the source diffusion pump. Radical cations were generated via electron ionization in the source of the instrument. The ions were then accelerated towards the magnetic sector using acceleration voltages ranging from 6-8 kV depending on the experiment being performed. The ion of interest would be mass selected in the magnetic sector. In the case of a MIKES experiment, the mass selected ion is allowed to travel through the second field free region towards the first electrostatic analyzer (ESA).[2] If the ion has sufficient energy to dissociate (i.e., is metastable), its fragment ions will be detected along with the remaining parent ions according to their kinetic energies. For CID experiments, helium collision gas was

introduced into the collision cell in the second field-free region of the instrument to a pressure that resulted in 10% reduction of the precursor ion beam (single collision conditions). For MI-CID experiments, one of the metastably-generated ions is selected in the first ESA, and then undergoes CID in the third field-free region. Spectra were recorded using ZABCAT program which was developed by Mommers Technologies (Ottawa, Canada). [3]

3.1.2. iPEPICO

All iPEPICO experiments were performed on the VUV beamline at the Swiss Light Source (Paul Scherrer Institut, Villigan, Switzerland). The experimental setup and a detailed description of the experiment are presented elsewhere.[4-6] Briefly, monochromatic VUV synchrotron radiation is used as a photoionization source to ionize gas molecules. Ions are directed towards a time of flight mass spectrometer (TOF) while the ejected electrons are extracted in the opposite direction towards an imaging multichannel plate (MCP) detector with each event time and position stamped. Threshold electrons are focused onto the center of the MCP, and kinetic energy electrons detected in a small ring region around this center spot give a good representation of the hot electron background of the threshold signal. The mass spectrum corresponding to this ring is subtracted from the center TOF distribution to obtain the threshold ionization mass spectra.

The time-of-flight mass spectrometer has two acceleration regions, one of which has a low draw out potential which means that ions dissociating on the microsecond timescale can do so in this region. The results are ion time of flight distributions that are asymmetric. These asymmetric distributions can be modeled to extract absolute unimolecular decay rate constants.

The small fields of 40–120 V cm^{-1} in the ion acceleration region lead to the long ion residence times, which are indispensable for rate measurements and are also necessary for the 1 meV electron kinetic energy resolution at threshold. As a drawback, thermal TOF peak widths on the order of 100 ns mean that the parent, H-loss and 2H-loss peaks overlap, and it is necessary to use a deconvolution procedure to extract parent and daughter ion fractional abundances. It was shown previously that H-loss peak center of gravity functions can be used as a measure for peak asymmetries at very low signal levels.[7] and to extract the rate information even when the peak shape is dominated by thermal broadening.[8] In our case, the rate information is readily available based on the C_2H_2-loss peak shape, in cases where this fragment is found, which decays towards higher times-of-flight as the parent ion is depleted, i.e. according to the sum of rates for all parallel processes. In turn, the fractional abundances of the fragment ions indicate the relative rates. In the deconvolution procedure, we assume that the peak positions are constant and the peaks have the same full-width-half-maximum. Because of the small mass and time-of-flight differences, the error of these assumptions is expected to be negligible.

The weighted center of the TOF distribution easily yields the fractional abundances for two peaks. For example, if the molecular ion $M^{+\bullet}$ is detected at a TOF of t_1 and the $[M–H]^+$ peak grows in with increasing photon energy at t_2, the center of gravity of their TOF band will be $\mu = a \cdot t_1 + (1 - a)t_2$, where a is the parent ion fractional abundance. The breakdown diagram can thus be plotted by evaluating μ as a function of photon energy and solving this equation for a. However, a second metric is required to deconvolute a band of three such peaks with arrival times t_1, t_2 and t_3, and to obtain the fractional abundances a, b,

and c where $a + b + c = 1$. In the present case, this involves either the combination of $[M–H]^+$, $M^{+\bullet}$ and $^{13}C\text{-}M^{+\bullet}$, or that of $[M–2H]^{+\bullet}$, $[M–H]^+$ and $M^{+\bullet}$.

In addition to the band center $\mu = \int t\ \mathrm{TOF}(t)\ \mathrm{d}t\ /\ \int \mathrm{TOF}(t)\ \mathrm{d}t$, the 2nd moment of the distribution, $\sigma^2 = \int t^2\ \mathrm{TOF}(t)\ \mathrm{d}t\ /\ \int \mathrm{TOF}(t)\ \mathrm{d}t$ can be used as additional metric. For a single Gaussian distribution with a mean t_1 and standard deviation σ_P, this evaluates to $\sigma^2 = t_1^2 + \sigma_P^2$. If we consider three peaks with relative abundances a, b and c, with arrival times of t_1, t_2 and t_3, the 2nd moment will be given as $\sigma^2 = a \cdot t_1^2 + b \cdot t_2^2 + c \cdot t_3^2 + \sigma_P^2$, whereas the band center of gravity is obtained as $\mu = a \cdot t_1 + b \cdot t_2 + c \cdot t_3$. The time-of-flight distributions are, thus, used to obtain σ and μ, and the two expressions just derived can be solved for the fractional abundances a, b and c:

$$a = \left(\sigma^2 - \sigma_p^2 - \mu(t_2 + t_3) + t_2 t_3\right) / \left((t_1 - t_2)(t_1 - t_3)\right) \tag{3.1}$$

$$b = \left(\sigma^2 - \sigma_p^2 - \mu(t_1 + t_2) + t_1 t_2\right) / \left((t_3 - t_2)(t_3 - t_1)\right) \tag{3.2}$$

$$c = \left(\sigma^2 - \sigma_p^2 - \mu(t_1 + t_3) + t_1 t_3\right) / \left((t_2 - t_1)(t_2 - t_3)\right) \tag{3.3}$$

After deconvolution of the three peaks in question, ^{13}C contributions were taken into account prior to the calculation of final relative abundances for use in the breakdown diagrams.

The threshold photoelectron spectrum for a given compound was obtained by summing the counts of all threshold electrons at each photon energy.

3.2. Computational methods

3.2.1. Ab Initio Calculations

Ionic structures were calculated for the precursor ion and all potential fragments, as well as the neutral structures for the precursor molecules. These *ab initio* calculations were completed using Gaussian 09 suite of programs.[9] Geometry optimizations and vibrational calculations were performed using the B3LYP/6-31+G(d) level of theory, while single point energies were calculated at B3LYP/6-311+G(3df,2p) level. The harmonic vibrational frequencies and rotational constants for neutral and ionic naphthalene were used as input for subsequent RRKM calculations.

Outer valence Green's function calculations (OVGF) were carried out with the cc-pVQZ basis set to predict molecular orbital ionization energies.[10]

3.2.2. RRKM calculations

In order to determine the 0K activation energy (E_0) and the entropy of activation ($\Delta S^{\ddagger}$) from the experimental breakdown curves, the rate of each dissociation pathway, k(E), needs to be determined. k(E) was calculated according to equation 2.11.[11] The calculated vibrational frequencies and rotational constants were used to calculate the reactant ion density of states according to the Beyer and Swinehart direct count algorithm.[12] The transition states were not calculated; instead, an appropriate vibrational mode was removed to simulate the critical transition coordinate, such as a C-H stretch removed for the formation of $C_{10}H_7^+$ from naphthalene, or a mode corresponding to a change in H-H distance (and H-C distance) for H_2 loss. These frequencies are listed in the appendix. The transition state sum-of-states were varied as part of the fitting process by scaling the transitional

modes by a common factor. $\Delta S^{\ddagger}_{1000}$ was calculated at 1000 K according to the standard statistical mechanics equations. No restriction has been imposed on the degree of tightness or looseness of the transitions states.

3.2.3. Theoretical model fitting

The minimal iPEPICO program of Sztáray et al. was used for fitting the experimental breakdown curves and ion time-of-flight distributions.[13] In brief, this program employs RRKM theory to fit experimental breakdown curves for competing dissociation channels based on vibrational frequencies and rotational constants for the parent neutral and dissociating ions, which in this work consists of $M^{+\bullet}$ and $M\text{-}H^{+}$, the experimental conditions such as temperature, the experimental data, and the ion optics parameters of the iPEPICO apparatus, as well as the barrier heights of each dissociation step. The experimental data required consists of the fractional fragment ion abundances over a range of energies (i.e. the breakdown diagram) as well as the TOF spectra corresponding to each energy. Photon energies were converted to ion internal energies for the RRKM modeling using the reported ionization energy of each molecule.[10]

The rate constants determined from the iPEPICO experiments, ranging between 10^3-10^7 s^{-1}, have been compared with those from the MIKES results in Figure 15. It can be seen that the iPEPICO samples a much larger portion of the k(E) curve, but due to the overlap between the two techniques, the MIKES data is beneficial in confirming the values determined by the iPEPICO results.

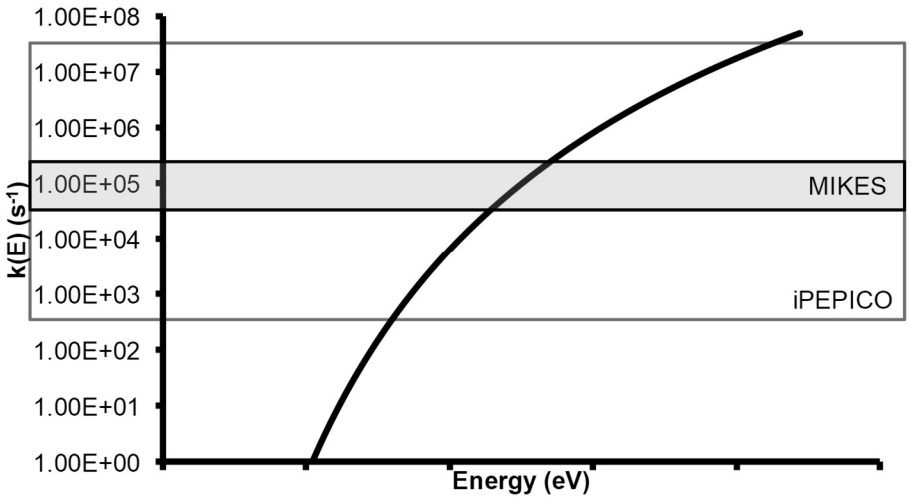

Figure 15: Energy (eV) versus k(E) plot comparing the regions of the rate curve sampled by MIKES experiments (grey shading) and iPEPICO (white area)

3.2.4. APCI-CID Modelling

Full details for the APCI-CID model have been reported previously.[14] The three main experimental parameters for this model are; the time-scale of the dissociation, the internal energy distribution of the collision complex (dependent on E_{com} and gas density) and k(E). The time scale is known based on the length of the collision cell (10 cm) and the translational energy, T (in this case T = E_{lab}). The energy range was converted to center of mass energy (E_{com}) using the following equation,

$$E_{com} = E_{lab}\left(\frac{M_{Ar}}{M_{Ar}+M_{ion}}\right) \tag{3.4}$$

where M_{Ar} and M_{ion} are the respective mass (argon and anthracene radical cation). The microcanonical rate constant is given by RRKM theory as outlined earlier, having two adjustable parameters, E_0 and $\Delta^{\ddagger}S$. As mentioned in the introduction, the post-collision internal energy distribution of the dissociating ions has been approximated by the relationship,

$$T_{eff} = T_i + \alpha(E_{com}) \quad (3.5)$$

with α and the initial temperature (T_i) also being adjustable parameters that can be varied in order to obtain the best fit between the theoretical and experimental dissociation diagrams.[15] The resulting internal energy distribution of the anthracene ions is given by:

$$P(E, E_{com}) = \frac{\rho(E)e^{-E/RT_{eff}}}{Q(E_{com})} \quad (3.6)$$

where ρ(E) is the vibrational density of states (same as what was used for RRKM), $Q(E_{com})$ is the vibrational partition function at an effective temperature, T_{eff}, described above. Theoretical branching ratios are then derived and fit to the experimental CID breakdown diagrams.

In fitting the APCI-CID experiments, the iPEPICO results were used as an initial guess for E_0 and $\Delta^{\ddagger}S$ for $[M\text{-}H]^+$ and $[M\text{-}C_2H_2]^{+\cdot}$. Once an acceptable α value was obtained, these values were then adjusted to get the best possible fit with the experimental data.

3.3 References for Chapter 3

1. Holmes, J. L.; Mayer, P. M., Combined Mass Spectrometric and Thermochemical Examination of the C2H2n Family of Cations and Radicals. *J. Phys. Chem.* **1995,** *99*, 1366-1370.
2. Busch, K. L.; Glish, G. L.; McLuckey, S. A., *Mass Spectrometry/Mass Spectrometry*. VCH Publishers: New York, 1988.
3. Traeger, J. C.; Mommers, A. A., A Data Acquisition System for Mass-Analyzed Ion Kinetic Energy Spectra Using a Personal Computer. *Org. Mass Spectrom.* **1987,** *22*, 592-596.
4. Johnson, M.; Bodi, A.; Schulz, L.; Gerber, T., Vacuum Ultraviolet Beamline at the Swiss Light Source for Chemical Dynamics Studies. *Nucl. Instrum. Meth. A.* **2009,** *610*, 597-603.

5. Bodi, A.; Johnson, M.; Gerber, T.; Gengeliczki, Z.; Sztáray, B.; Baer, T., Imaging Photoelectron Photoion Coincidence Spectroscopy with Velocity Focusing Electron Optics. *Rev. Sci. Instr.* **2009,** *80*, 034101.

6. Bodi, A.; Sztaray, B.; Baer, T.; Johnson, M.; Gerber, T., Data Acquisition Schemes for Continuous Two-Particle Time-of-Flight Coincidence Experiments. *Rev. Sci. Instrum.* **2007,** *78*, 084102.

7. Fischer, K. H.; Schneider, M.; Fischer, I.; Pfaffinger, B.; Braunschweig, H.; Sztáray, B.; Bodi, A., Bonding in a Borylene Complex Investigated by Photoionization and Dissociative Photoionization. *Chemistry – A European Journal* **2012,** *18*, 4533-4540.

8. Bodi, A.; Daniel Brannock, M.; Sztaray, B.; Baer, T., Tunneling in H Loss from Energy Selected Ethanol Ions. *PCCP* **2012,** *14*, 16047-16054.

9. Frisch, M. J.; Trucks, G. W.; Schlegel, H. B.; Scuseria, G. E.; Robb, M. A.; Cheeseman, J. R.; Montgomery, J. A.; Vreven, T.; Kudin, K. N.; Burant, J. C.*, et al.*, Gaussian 03, Revision C.02. 2003.

10. Mayer, P. M.; Blanchet, V.; Joblin, C., Threshold Photoelectron Study of Naphthalene, Anthracene, Pyrene, 1,2-Dihydronaphthalene, and 9,10-Dihydroanthracene. *J. Chem. Phys.* **2011,** *134*, 244312.

11. Baer, T.; Hase, W. L., *Unimolecular Reaction Dynamics, Theory and Experiments*. Oxford University Press: New York, 1996.

12. Beyer, T.; Swinehart, D. R., Direct Count for RRKM. *ACM Commun.* **1973,** *16*, 379.

13. Sztáray, B.; Bodi, A.; Baer, T., Modeling Unimolecular Reactions in Photoelectron Photoion Coincidence Experiments. *J. Mass Spectrom.* **2010,** *45*, 1233-1245.

14. Mayer, P. M.; Martineau, E., Gas-Phase Binding Energies for Non-Covalent a[Small Beta]-40 Peptide/Small Molecule Complexes from CID Mass Spectrometry and RRKM Theory. *PCCP* **2011,** *13*, 5178-5186.

15. Renaud, J. B.; Martineau, E.; Mironov, G. G.; Berezovski, M. V.; Mayer, P. M., The Collaborative Role of Molecular Conformation and Energetics in the Binding of Gas-Phase Non-Covalent Polymer/Amine Complexes. *PCCP* **2012,** *14*, 165-172.

4 Naphthalene

4.1 Introduction

Naphthalene ($C_{10}H_8$) is one of the smallest PAHs, and the fragmentation of its cation has been intensively studied in the past showing that H-loss and C_2H_2-loss are the two main channels of fragmentation appearing with equal branching ratios at low photon energy (< 18 eV). There is no significant difference that has been observed in the dissociative ionization of the fully deuterated naphthalene,[1-3] although Jochims and co-workers have claimed a small kinetic isotope effect from differences in the onset appearance energies between deuterated and undeuterated naphthalene.[4-5] The main cationic fragment is the $C_{10}H_7^+$ ion with three higher energy parallel fragmentations that have been detected in ion cyclotron resonance experiments.[6] By different mass spectrometric techniques, it has been established that the cationic fragment $C_8H_6^+$ is benzocyclobutadiene[7] as initially suggested theoretically and confirmed recently.[8] Two more (minor) dissociation channels observed are H_2 loss and C_4H_2 loss. For the latter the phenylvinylacetylene structure has been proposed for the resulting ion, similar to what has been suggested for the dissociation of the neutral system.[9]

In this chapter, we revisit experimentally the dissociation reactions of the naphthalene ion via mass-analyzed ion kinetic energy spectrometry (MIKES), collision induced dissociation (CID) and metastable ion collision induced dissociation (MI-CID) experiments as well as imaging photoelectron-photoion coincidence experiment (iPEPICO). The iPEPICO experiment at the VUV beamline of the Swiss Light Source (SLS) selects ions as a function of their internal energy with 2 meV photon resolution and measures dissociation rate constants within the 10^3-10^7 s^{-1} range. This experimental set-up allows the

determination of the dissociation thresholds for fragment ions. By fitting the breakdown curves as well as the asymmetric time-of-flight profiles, kinetic modeling of the dissociative ionization processes can be achieved. This allows an accurate determination of barrier heights and entropies of activation that have an impact on dissociation and are useful parameters for the atmospheric, combustion or interstellar chemistry models to postulate pathways of aromatic formation by hydrogen-abstraction and C_2H_2-addition. The present results can be compared to the early experiments done in time-resolved photodissociation: Ho et al.[1] worked at a single internal energy of $C_{10}H_8^+$ (namely 7.1 eV) while Gotkis et al.[3] assumed loose transition states, meaning little to no need for rearrangement prior to dissociation, for both H and C_2H_2 losses and neglected the minor channels that are the H_2 and C_4H_2 losses. In these two preceding works, a phenylacetylene structure was assumed for $C_8H_6^+$ obtained by C_2H_2 abstraction, while here the benzocyclobutadiene isomer is considered. The present energy resolution allows a greater confidence in the parameters extracted and consequently allows us to predict the structures of $C_{10}H_6^+$ produced in two different channels.

4.2 Results and discussion

4.2.1 Tandem Mass Spectrometry

Figure 16a shows the MIKES spectra for the fragmentation of the naphthalene radical cation at different acceleration voltages.

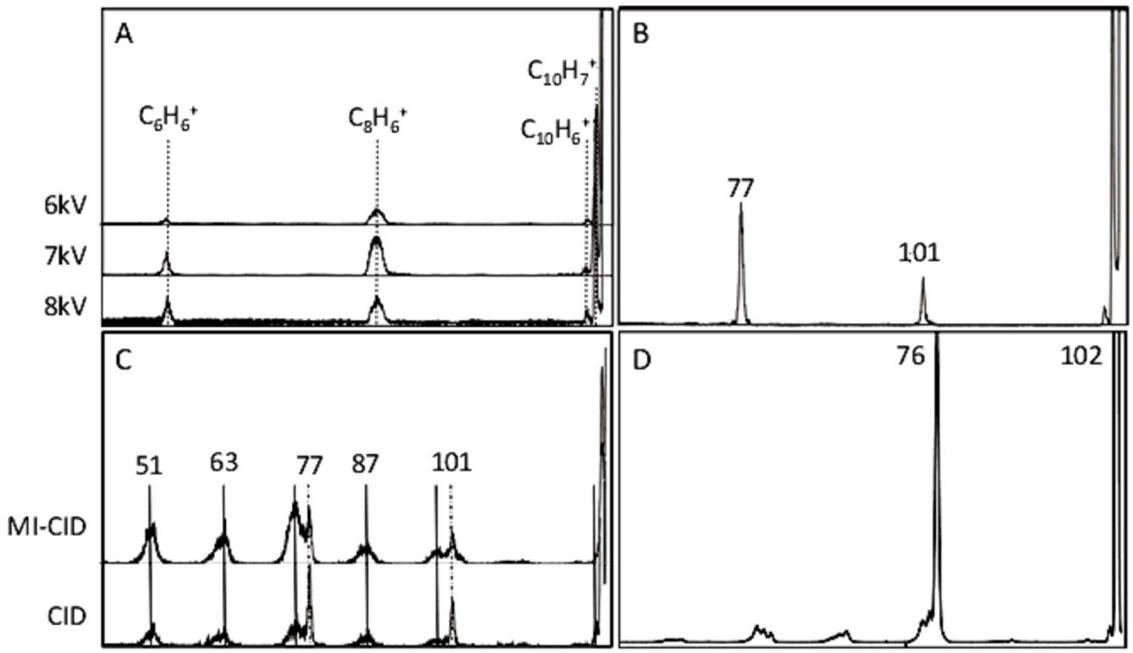

Figure 16: (A) MIKES mass spectra of $C_{10}H_8^+$ collected at acceleration voltages of 6, 7 and 8 kV; (B) MIKES mass spectrum of $C_{10}H_7^+$ collected at an acceleration voltage of 8kV; (C) Comparison of CID and MI-CID mass spectra of source-generated versus metastably- generated $C_{10}H_7^+$ collected at an acceleration voltage of 8 kV. (D) CID mass spectrum of source generated $C_8H_6^{+\bullet}$ collected at an accelerating voltage of 8 kV and colliding with helium gas at single collision conditions (10% beam reduction).

By changing the accelerating voltage, the timescale of the metastable dissociation in the second field-free region is also changed, which affects the competition between the various reaction pathways. Four primary dissociation channels (reactions of naphthalene) have been observed from the naphthalene radical cation ($C_{10}H_8^{\cdot+}$). These channels correspond to the reactions (R1) through (R4);

$$C_{10}H_8^{\cdot+} \rightarrow C_{10}H_7^+ + H \quad (m/z\ 127) \qquad (R1)$$

$$C_{10}H_8^{\cdot+} \rightarrow C_8H_6^{\cdot+} + C_2H_2\ (m/z\ 102) \qquad (R2)$$

$$C_{10}H_8^{\cdot+} \rightarrow C_6H_6^{\cdot+} + C_4H_2\ (m/z\ 78) \qquad (R3)$$

$$C_{10}H_8^{\cdot+} \rightarrow C_{10}H_6^{\cdot+} + H_2\ (m/z\ 126) \qquad (R4)$$

Figure 16b shows the MIKES results for the fragment ion $C_{10}H_7^+$ which shows loss of C_2H_2 (m/z 101) and three additional pathways, reactions R5 – R7;

$$C_{10}H_7^+ \rightarrow C_6H_5^+ + C_4H_2 \text{ (m/z 77)} \quad \text{(R5)}$$

$$C_{10}H_7^+ \rightarrow C_{10}H_6^{\cdot+} + H \text{ (m/z 126)} \quad \text{(R6)}$$

$$C_{10}H_7^+ \rightarrow C_8H_5^{\cdot+} + C_2H_2 \text{ (m/z 101)} \quad \text{(R7)}$$

Reactions (R5) and (R6) will come into play later in the iPEPICO experiment. It should be noted that all MI-CID mass spectra of metastably-generated fragment ions were compared to their source-generated analogues, and found to be indistinguishable. Figure 16c shows a comparison between the CID mass spectrum of source-generated $C_{10}H_7^+$ and the MI-CID of metastably-generated $C_{10}H_7^+$. It can be seen that the fragmentation patterns of the two ions are identical, with only small intensity differences, indicating that the same structures are formed from source generated and metastable ions.

The most likely fragment ion structures in reactions (R1)-(R6) are outlined in Figure 17. For reaction (R1), it is not possible to identify the location of the missing hydrogen atom due to hydrogen scrambling which is known to occur upon CID.[10] Dyakov et al. also calculated that the difference in energy for the two distinct hydrogen sites as being only 0.05 eV.[8] For this reason, all hydrogen atoms are treated equally for the purpose of RRKM calculations. Reaction (R2) introduces a more complicated structure assignment. While there are many possible structures to produce $C_8H_6^{+\cdot}$, there are two which were theorized as the possible structures based on naphthalene being the starting structure, phenylacetylene and benzocyclobutadiene.[11]

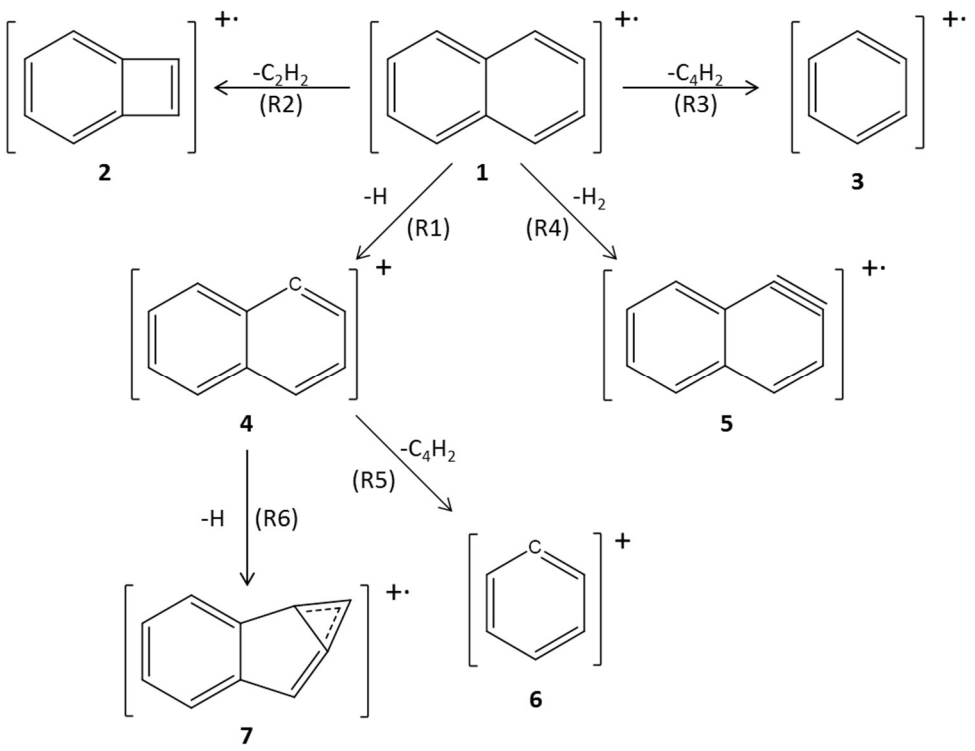

Figure 17: Model for fragmentation of naphthalene radical cations with the most likely structures shown for fragment ions from reactions (R1)-(R6). The reaction number for each product channel has been included in parentheses.

Looking at the CID mass spectrum of $C_8H_6^{+\cdot}$ (Figure 16d), it can be seen that the most intense peak is located at m/z 76, which is a second loss of C_2H_2. There are other peaks which are also consistent with the breakdown of conjugated unsaturated hydrocarbons. Both structures can lose these fragments quite easily and therefore there is little distinction that would be visible through CID. In fact, it has been reported that both ions have identical tandem mass spectra due to small differences in energy. Schroeter et al. deduced the structure of $C_8H_6^+$ through charge reversal (CR) mass spectrometry.[7] They were able to eliminate ionized phenylacetylene as a contributing structure based on the presence of $C_8H_5^-$ in its CR mass spectrum while the same peak was absent in the mass spectrum of $C_8H_6^{+\cdot}$

produced from naphthalene and from benzocyclobutadiene. Thus, the structure assignment of $C_8H_6^{+\cdot}$ for reaction (R2) is that of ionized benzocyclobutadiene. The next fragment, reaction (R3), $C_6H_6^{+\cdot}$ was assigned as the benzene cation. For reaction (R4), the formation of $C_{10}H_6^{+\cdot}$, has several possible structures; however, only two structures were calculated to be of reasonable energy, which are shown as structures **5** and **7** in Figure 17. When calculated at the B3LYP/6-311+G(3df,2p) level of theory, the difference in energy between these two structures was only 0.11 eV, which makes both structures attainable. The best way to differentiate between the two structures would be to use $\Delta^{\ddagger}S$, as structure **7** requires a lot of rearrangement, which would result in $\Delta^{\ddagger}S$ being negative, whereas the 1,2 hydrogen loss leading to structure **5** would have an $\Delta^{\ddagger}S$ closer to zero or slightly positive. As will be seen below, we derive a positive $\Delta^{\ddagger}S$ for the reaction channel (R4), suggesting the product of this reaction is structure **5**.

Reaction (R5) was relatively straightforward to assign as $C_6H_5^+$ is most likely the phenyl cation based on the starting structure of $C_{10}H_7^+$. For reaction (R6), the assignment of the secondary formation of $C_{10}H_6^{+\cdot}$ requires the same steps as its production from reaction (R4), however as there is no need for the formation of H_2 it is expected that the 1,3 H loss product ion is the resulting structure as it is the lowest in energy (structure **7**, cycloprop[a]indene). This structure is further supported when the iPEPICO results are considered. As will be seen in the following section, the fitted curve for reaction (R6) resulted in $\Delta^{\ddagger}S_{1000} = -19 \pm 11$ J K^{-1} mol^{-1}, whereas reaction (R4) resulted in $\Delta^{\ddagger}S_{1000} = 11 \pm 4$ J K^{-1} mol^{-1}. This indicates that the two pathways result in different structures, with reaction (R6) requiring more extensive rearrangement. Therefore, structure **7** was assigned to

reaction (R6) as it is the lowest energy structure, and would result in a negative value for $\Delta^{\ddagger}S$.

The tandem mass spectra can also be used to assign some preliminary values for $\Delta^{\ddagger}S$ and E_0. This is accomplished by comparing the various branching ratios at different acceleration voltages, and hence kinetic timescales (Figure 16A). When the ratios of $C_{10}H_7^+$ and $C_8H_6^{+\cdot}$ are compared over the range of acceleration voltages used (6 - 8kV) it can be seen that as the kinetic energy increases, the relative amount of $C_{10}H_7^+$ compared to $C_8H_6^{+\cdot}$ decreases. In order to compete on the microsecond timescale in this fashion, the dissociation leading to $C_{10}H_7^+$ must have a higher $\Delta^{\ddagger}S$ compared to $C_8H_6^{+\cdot}$, while its E_0 must therefore be higher as well. This trend is in agreement with the conclusions of references 4 and 26 for the relative values of both $\Delta^{\ddagger}S$ and E_0 (Tables 1 and 2).

Table 1: Activation energies (E_0/eV) for the dissociation pathways of naphthalene cation compared to literature values from both experimental and computational methods

	iPEPICO	**Literature**			
		Experimental		**Theoretical**	
(R1) $C_{10}H_8^{\cdot+} \rightarrow C_{10}H_7^+ + H$	4.20 ± 0.04	4.23[a]	4.48 ± 0.10[b]	3.79[d]	4.8[e]
(R2) $C_{10}H_8^{\cdot+} \rightarrow C_8H_6^{\cdot+} + C_2H_2$	4.12 ± 0.05	4.6[a]	4.41 ± 0.20[b]	3.89[d]	4.6[e]
(R3) $C_{10}H_8^{\cdot+} \rightarrow C_6H_6^{\cdot+} + C_4H_2$	4.27 ± 0.07			4.50[d]	
(R4) $C_{10}H_8^{\cdot+} \rightarrow C_{10}H_6^{\cdot+} + H_2$	4.72 ± 0.06			3.25[d]	5.76[f]
(R5) $C_{10}H_7^+ \rightarrow C_6H_5^{\cdot+} + C_4H_2$	3.69 ± 0.26	4.3 ± 0.2[c]			
(R6) $C_{10}H_7^+ \rightarrow C_{10}H_6^{\cdot+} + H$	3.20 ± 0.13	4.1 ± 0.2[c]			

[a]Reference 6. [b]Reference 4. [c]Reference 9. [d]Reference 11. [e]Reference 26. [f]Reference 25, calculated barrier for loss of H_2 from 1 and 9 positions.

Table 2: Entropy of Activation ($\Delta^{\ddagger}S$) for All Dissociation Pathways of Naphthalene Compared to Literature Values

	iPEPICO $\Delta^{\ddagger}S_{1000}$	Literature $\Delta^{\ddagger}S_{1000}$	
(R1) $C_{10}H_8^{\cdot+} \rightarrow C_{10}H_7^{+} + H$	2 ± 2	12.5[a]	23.4 ± 8.4[b]
(R2) $C_{10}H_8^{\cdot+} \rightarrow C_8H_6^{\cdot+} + C_2H_2$	0 ± 2	35.5[a]	14.6 ± 12.6[b]
(R3) $C_{10}H_8^{\cdot+} \rightarrow C_6H_6^{\cdot+} + C_4H_2$	4 ± 4		
(R4) $C_{10}H_8^{\cdot+} \rightarrow C_{10}H_6^{\cdot+} + H_2$	11 ± 4		
(R5) $C_{10}H_7^{+} \rightarrow C_6H_5^{\cdot+} + C_4H_2$	5 ± 15	26.8 ± 8[c]	
(R6) $C_{10}H_7^{+} \rightarrow C_{10}H_6^{\cdot+} + H$	-19 ± 11	-0.4 ± 3[c]	

*(All Numbers Given in J K^{-1} mol^{-1} and Determined at 1000 K). [a]Reference 6. [b]Reference 4. [c]Reference 9.

The results are similar for reactions (R3) and (R4). When the ratios of $C_6H_6^{\cdot+}$ to $C_{10}H_6^{\cdot+}$ are compared, it was observed that an increase in the acceleration voltage (which results in a shorter reaction time in the second field-free region) favors $C_6H_6^{\cdot+}$. This indicates that $\Delta^{\ddagger}S$ for $C_{10}H_6^{\cdot+}$ formation must be greater than that to make $C_6H_6^{\cdot+}$, and consequently so must the E_0, if the two channels are to be competitive on this time scale. To date, no experimental data has been found confirming this trend as most groups disregard these pathways due to their low intensities.[3]

4.2.2 iPEPICO Spectrometry

iPEPICO experiments were conducted for photon energies ranging from 14 to 20.5 eV. The fragment ions observed in the tandem MS experiments were also observed in the iPEPICO experiments, with the sequential channels (R5 and R6) becoming evident at approximately 18.5 eV. Figure 18 shows the experimental breakdown curves for all 6 channels.

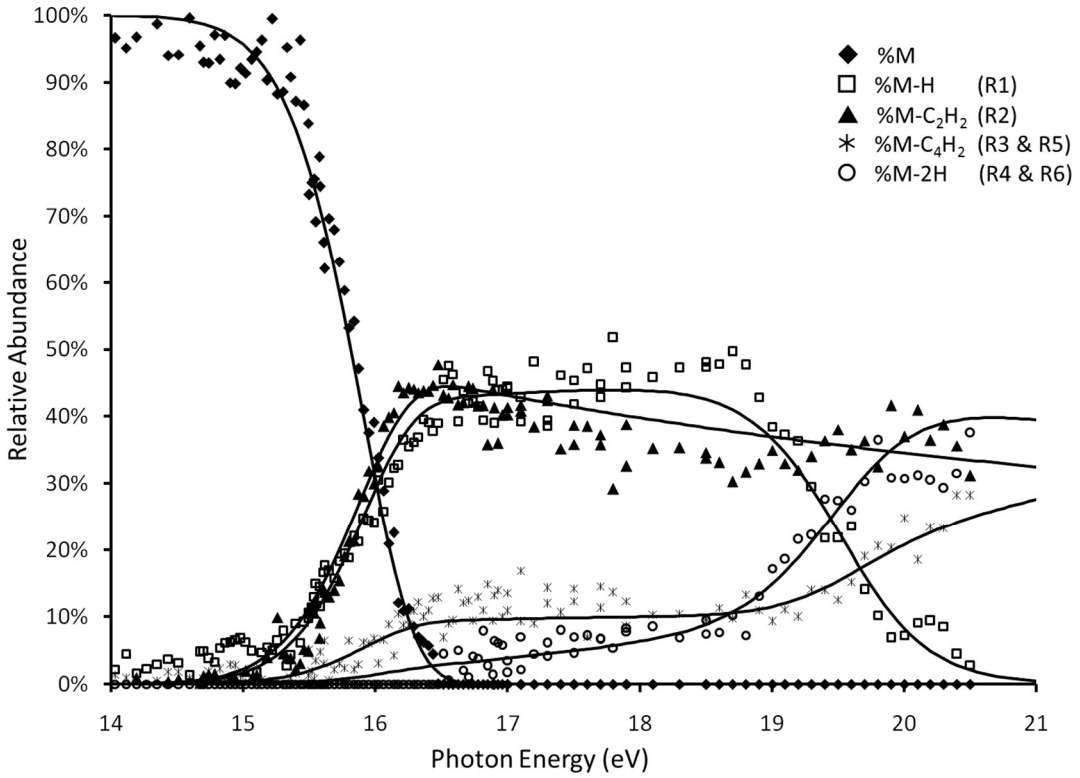

Figure 18: Experimental iPEPICO breakdown curve for the naphthalene radical cation over the photon energy range of 14.0 to 20.5 eV. The reaction number for each product channel has been included in parentheses. Calculated fits are overlaid. Derived energetic and entropic parameters can be found in Tables 1 and 2.

It should be noted that the peak at m/z 77 (R5) was not resolved in the iPEPICO results; instead there was an increase in the intensity, and breadth of the peak with m/z 78 at energies above 18.5 eV. Due to this, and the low signal-to-noise in the mass spectrum at m/z 78, it was not possible to de-convolute m/z 77 and 78, and so the breakdown curve was simulated as if the peak was m/z 78. The same transition state parameters used for m/z 78 were used for this "second" onset corresponding to m/z 77. A similar situation arises for the m/z 102 curve above 18.5 eV photon energy. While it is tempting to assign the slight rise in m/z 102 to the secondary fragmentation in which $[M\text{-}H]^+$ loses C_2H_2 (R7), there is no direct evidence from the data that this is the cause of the change in slope. Examination of the peak

at m/z 102 does not show conclusive evidence of the growth of m/z 101. The apparent small "dip" in the m/z 102 relative abundance is mirrored by the small rise in m/z 127, and we attribute this to uncertainties in the peak integration around $M^{+\cdot}$ and $[M-H]^+$ in this photon energy range.

Even with the above mentioned uncertainty in m/z 101, the current data and subsequent analysis has the benefit of incorporating the correction for "hot" electrons, the inclusion of the ion internal energy distribution, and the simultaneous fit of four primary reaction channels (and their time-of-flight distributions). The only significant issue with the current analysis is the reliability of RRKM to successfully extrapolate through a sizable kinetic shift to arrive at the correct E_0. As can be noted from the breakdown diagram in Fig. 3 and the RRKM estimated E_0 values in Table 1, the kinetic shift in the dissociation of the naphthalene cation is on the order of 2.7 eV.

All primary and secondary fragments were considered for the RRKM calculations. First, all four primary channels of dissociation were measured together (as they are formed with the same net observable rate constant, the sum of the individual channel rate constants). This was to allow for the fitting of the asymmetric TOF peak for $C_8H_6^{\cdot+}$ to accurately determine the optimal $\Delta^{\ddagger}S$ values. Figure 19 shows representative mass spectra, illustrating the asymmetry of m/z 102 over a range of energies. The other fragment ions were either too low in abundance or, as was the case with $C_{10}H_7^+$, too close to the parent peak to be able to observe the asymmetric tail.

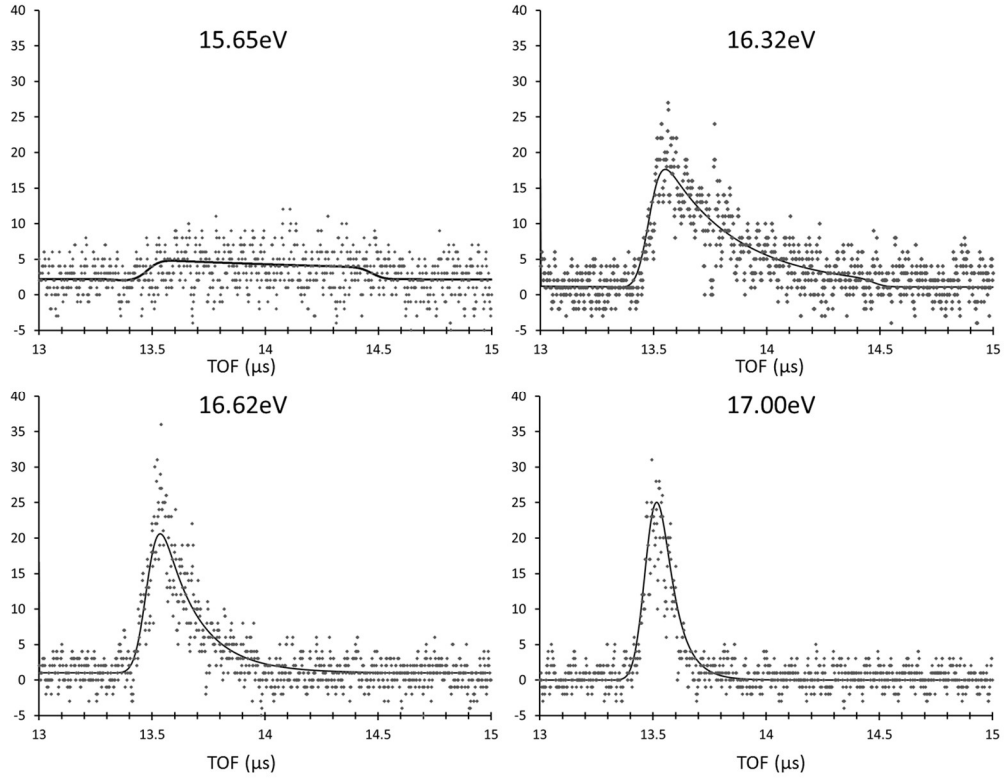

Figure 19: Representative TOF fits calculated during the RRKM fitting of experimental iPEPICO data. The region shown is the $C_8H_6^{+\cdot}$ region, as this peak was the only asymmetric TOF peak available. As the photon energy increases it can be seen that the peak become increasingly Gaussian in shape; at 17.00 eV it is completely Gaussian.

Once the $\Delta^{\ddagger}S$ values were determined for the four primary peaks, they were fixed in order to determine the E_0 values for all six reactions, and the two $\Delta^{\ddagger}S$ for the secondary reactions (reactions (R5) and (R6)). It was not possible to use the TOF peaks to aid in the accurate determination of $\Delta^{\ddagger}S$ as by this point in internal energy, all peaks were Gaussian in shape, meaning that fragmentation processes took place at $k > 10^7$ s^{-1}, i.e. fast on the experimental time scale. Thus the values for R5 and R6 have greater uncertainly associated with them (Table 2).

The theoretical breakdown curve fits can be seen in Figure 18. There is a fair degree of scattering in the experimental data in the higher energy range; therefore the fits in that

region are not quite as precise. As stated, all primary curves (for reaction R1-R4) were fit simultaneously and then only their E_0 values were modified while fitting the secondary reactions (R5 and R6). In all cases the standard deviation, calculated based on the difference between the fitted curve and the experimental data points, is < 3% even with a large degree of scattering for the secondary reactions.

The E_0 and $\Delta^{\ddagger}S$ values estimated from these fits are summarized in Table 1 Table 2, along with experimental and calculated values found in the literature. The formation of $C_{10}H_7^+$ and $C_8H_6^{\cdot+}$ have been studied extensively and literature values for both E_0 and $\Delta^{\ddagger}S$ have been determined using a variety of methods. Only two computational papers were found which had values for E_0 for $C_6H_6^{\cdot+}$ and $C_{10}H_6^{\cdot+}$.[8, 11] These reaction paths were noted by Gotkis *et al.*;[3] however, they stated that for their calculations they neglected the minor channels.[3] For the secondary channels, Laskin et al. measured their energetics using bromonaphthalene as the starting material.[6] It is noteworthy that they detect a third subsequent dissociation channel from the naphthyl cation that is an acetylene loss via a loose transition state.

The iPEPICO data were fit using RRKM theory, an E_0 value of 4.20 ± 0.04 eV was obtained for reaction (R1). This value is in reasonable agreement with those found in the literature, as seen in Table 1. There was a larger difference when the entropies were compared. For reaction (R1), $\Delta^{\ddagger}S_{1000}$ was calculated to be 2 ± 2 J K^{-1} mol^{-1}; which is a much smaller positive value than either of the literature values compared. To test the validity of these values, $\Delta^{\ddagger}S_{1000}$ was fixed in the calculation to literature values and then the activation energies were manipulated to get the best fit possible. The result of this can be seen in Figure 20a.

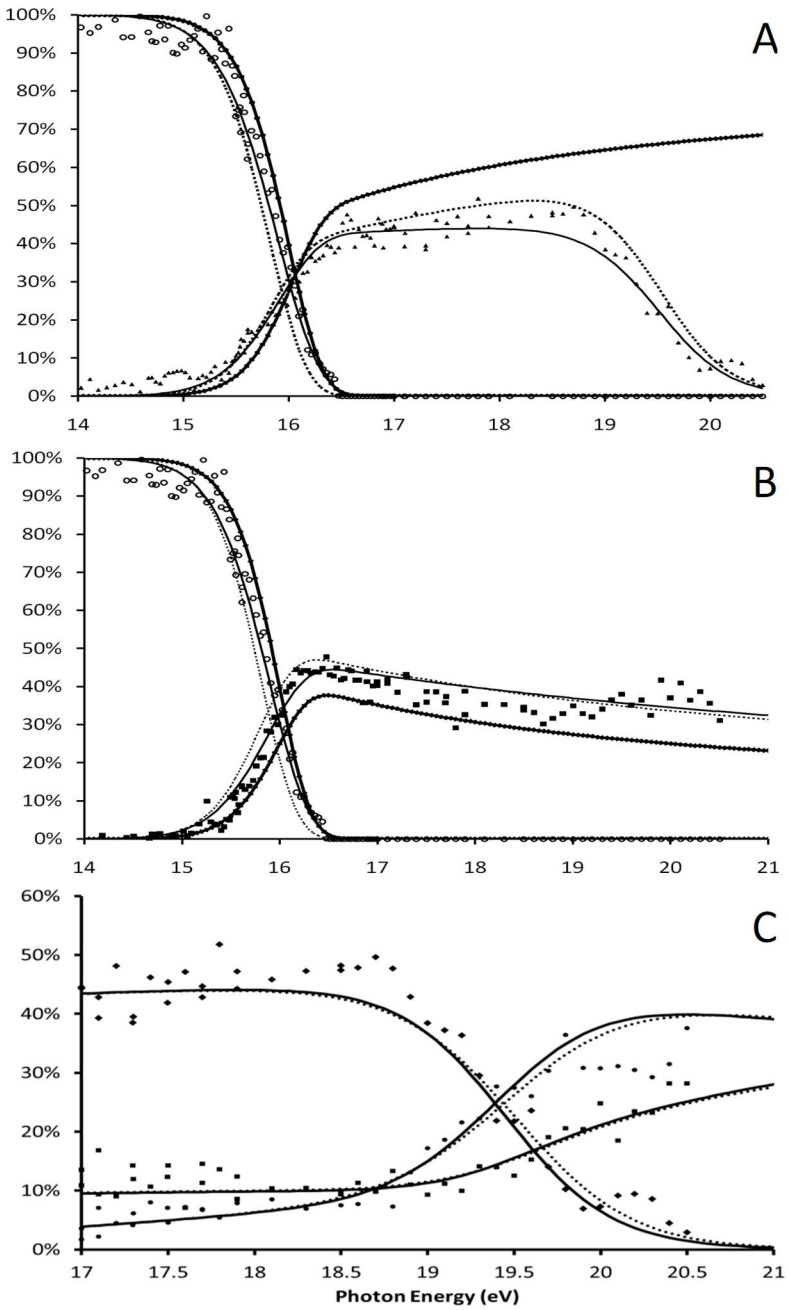

Figure 20: (A) iPEPICO fit of $C_{10}H_8^{+\bullet}$ and $C_{10}H_7^{+}$ using current $\Delta^{\ddagger}S$ values (solid line), reference 4 (dashed line) and reference 6 (solid line with diamond markers); (B) iPEPICO fit of $C_{10}H_8^{+\bullet}$ and $C_8H_6^{+\bullet}$ using current $\Delta^{\ddagger}S$ values (solid line), reference 4 (dashed line) and reference 6 (solid line with diamond markers); (C) iPEPICO fit of $C_{10}H_7^{+}$, $C_{10}H_6^{+\cdot}$ and $C_6H_5^{+}$ using current $\Delta^{\ddagger}S$ values (solid line) and reference 9 (dashed line).

With the original values calculated, the average absolute error per point (Err_{ave}) for $C_{10}H_7^+$ was 2.86%. However, when the calculations were completed with $\Delta^{\ddagger}S_{1000}$ from literature the error was; 5.59% (Gotkis, E_0 = 4.33 eV, $\Delta^{\ddagger}S_{1000}$= 12.5 J K^{-1} mol^{-1}) and 3.53% (Ho, E_0 = 4.49 eV, $\Delta^{\ddagger}S_{1000}$= 23.5 J K^{-1} mol^{-1}) The error values corresponding to Gotkis et al. values are only for the energy range 14-18 eV as it was impossible to get the secondary curves to fit. These results indicate that the presence of reactions (R3)-(R6) have a noticeable impact on the calculated values for $C_{10}H_7^+$. In Ho et al.[1] work done at a single internal energy, the RRKM parameters were constrained to get a strongly positive entropy of activation for the H-loss.

The other major fragmentation pathway is the formation of $C_8H_6^{\cdot+}$ through the loss of acetylene. As the structure was determined to be benzocyclobutadiene, this was the structure chosen for comparison with calculated E_0 and $\Delta^{\ddagger}S_{1000}$ values found in the literature (Table 1). For the activation energy, the literature values reported by Ho et al., Gotkis et al., and Holm et al. are higher than the current values of 4.12 ± 0.05 eV, but the difference is less than 0.5 eV. However, the observed trend in which the formation of $C_8H_6^{\cdot+}$ is slightly lower in energy than that of $C_{10}H_7^+$ was also observed by Holm[12] and Ho.[1] The $\Delta^{\ddagger}S_{1000}$ calculated in this work was 0 ± 2 J K^{-1} mol^{-1}, which is significantly lower than both values cited by Gotkis (35.5 J K^{-1} mol^{-1}) and Ho (14.6 J K^{-1} mol^{-1}) (Table 2). It can be seen though in Figure 20b that while the numbers differ significantly, those calculated in this work fit the experimental data (Err_{ave} =2.73%) better than those calculated using $\Delta^{\ddagger}S_{1000}$ values taken from Gotkis (Err_{ave} =3.41%) and Ho (Err_{ave} = 3.84%). Therefore, when the energetics of $C_{10}H_7^+$ and $C_8H_6^{\cdot+}$ are compared, it is observed that the relative trend predicted by tandem MS is accurate; that the $\Delta S^{\ddagger}$ and activation energy for $C_{10}H_7^+$ are slightly higher within the experimental errors than those for $C_8H_6^+$.

The determination of the kinetic parameters for the formation of $C_6H_6^{+\cdot}$ was more difficult due to its low intensity. A wider range of values yielded a reasonable fit with the experimental data; this led to using the TOF fits more heavily for determining the best value for $\Delta^{\ddagger}S$. As previously discussed, the structure for $C_6H_6^+$ is in all likelihood ionized benzene. Therefore, when the fit resulted in $\Delta^{\ddagger}S_{1000} = 4 \pm 4$ J K^{-1} mol^{-1}, the value was deemed reasonable as the transition state would consist of two bond cleavages without the need for any significant rearrangement. The activation energy was determined to be 4.27 ± 0.07 eV, which is in agreement with the only literature value found for this channel: Dyakov and co-workers calculated E_0 = 4.50 eV at the Gaussian-3 level of theory.[8]

The final primary channel is the formation of $C_{10}H_6^+$, through the loss of H_2. For this channel, the transition state was theorized to consist of the loss of two adjacent hydrogen atoms, which may or may not migrate onto the same carbon atom before dissociating. When the $\Delta^{\ddagger}S$ was calculated to be 11 ± 4 J K^{-1} mol^{-1}, this clearly indicates that the transition state is quite loose; therefore it is unlikely that any rearrangement occurs prior to fragmentation. Dyakov *et al.* calculated the activation energy as 3.25 eV,[8] which is substantially lower than the value determined here as 4.72 ± 0.06 eV. If the tandem MS results are also considered, the iPEPICO results are in agreement with the trend observed, which indicates that the activation energy for $C_{10}H_6^+$ must be higher than that for $C_6H_6^+$. Jolibois and co-workers calculated the barrier to H_2 loss from the 1 and 8 positions of naphthalene (5.76 eV). While their value is higher than those determined in the current work, the relative values calculated for the activation energies for H and H_2 loss (H_2 being 0.59 eV higher than H) are similar to the present results (0.52 eV), and thus this particular mechanism cannot be ruled out as a potential route to H_2 loss.[11]

For the two sequential channels, there was a significant amount of scattering in the experimental data due to low ion intensities. Due to this, there is a higher degree of uncertainty within these values. The first secondary channel, $C_6H_5^+$, would have a similar mechanism to reaction (R3), where two bond cleavages would result in the formation of the phenyl cation. The energetics calculated for this reaction were E_0 = 3.69 ± 0.26 eV and $\Delta^{\ddagger}S_{1000}$= 5 ± 15 J K^{-1} mol^{-1}. Laskin *et al.* also determined the energetics and got values of, E_0 = 4.3 ± 0.2 eV and $\Delta^{\ddagger}S_{1000}$= 26.8 ± 8 J K^{-1} mol^{-1}.[6] They assumed that this reaction is very fast with a first C-C bond cleavage triggered by a charge-site, followed by a hydrogen migration that initiates the second C-C bond cleavage. As with $C_{10}H_7^+$ and $C_8H_6^{+\cdot}$, the iPEPICO breakdown curves were fitted using the literature values to determine if they would fit the experimental data. Figure 20c shows the results of this fit for both secondary channels. If the error of the two fits are compared for $C_6H_5^+$; this work yielded Err_{ave} = 1.93% whereas using the $\Delta^{\ddagger}S$ determined by Laskin Err_{ave} = 1.99%. Absolute unimolecular dissociation rate information in the form of asymmetric fragment TOF peaks would have been invaluable in determining which value is correct.

The final channel, $C_{10}H_6^{+\cdot}$, resulting from the consecutive loss of hydrogen atoms, yielded energetics values of E_0 = 3.25 ± 0.10 eV and $\Delta^{\ddagger}S_{1000}$ = -18 ± 7 J K^{-1} mol^{-1}. Again, the activation energy is reasonable in comparison to literature, Laskin *et al.* reported a value of 4.1 ± 0.2 eV and assumed as well the 1,3-butadyine structure.[6] The $\Delta^{\ddagger}S$ values are significantly different, as they were with $C_6H_5^+$. When literature values were inserted for the $\Delta^{\ddagger}S$ of the calculations, Err_{ave} was 1.73% compared to 1.46% when using the fitted $\Delta^{\ddagger}S$. It should be noted, however, that the relative difference between the two channels are consistent, with $C_{10}H_6^{+\cdot}$ being approximately 25 J K^{-1} mol^{-1} lower in both the reported values

and literature. The extremely negative $\Delta^{\ddagger}S$ value is consistent with the hypothesized structure resulting from the 1,3 H loss from $C_{10}H_8^+$; the molecule would undergo extreme rearrangement to produce the tricyclic structure predicted by calculations as shown in the model in Figure 17.

The consecutive H-loss activation energies provide an initial C-H bond strength in the ion of 405 ± 4 kJ mol^{-1}, and a second sequential C-H bond strength of 309 ± 4 kJ mol^{-1}. These compare to the C-H bond strength in neutral naphthalene (position 1) of 472 ± 14 kJ mol^{-1} derived from electron affinity measurements of the 1-naphthyl radical (combined with ancillary thermochemical data).[13]

The activation energies, combined with the accurate ionization energy of naphthalene (8.1442 ± 0.0009 eV)[14] lead to an appearance energy (AE_{0K}) for the naphthyl cation of 1191 ± 4 kJ mol^{-1}, which in turn leads of an enthalpy of formation for the naphthyl cation, $\Delta_f H^o_0$ = 1148 ± 14 kJ mol^{-1}/ $\Delta_f H^o_{298}$ = 1123 ± 14 kJ mol^{-1} (site of dehydrogenation unspecified) based on the $\Delta_f H^o_{298}$(neutral $C_{10}H_8$) = 150 ± 10 kJ mol^{-1}, and $\Delta_f H^o$(H) = 217.998 ± 0.006 kJ mol^{-1}.[15] Thermal correction was made to the neutral naphthalene and naphthyl cation $\Delta_f H^o_{298}$ values employing calculated vibrational frequencies and standard thermal corrections for the elements in their standard state. This is slightly lower than the estimate of Gotkis et al. of $\Delta_f H^o_0$ = 1176 ± 12 kJ mol^{-1}/ $\Delta_f H^o_{298}$ = 1151 ± 14 kJ mol^{-1} based on their time-dependent photoionization appearance energy study of 1- and 2-bromonaphthalene.[16]

The additional 3.20 eV for the second H-loss (AE_{0K} = 1500 ± 17 kJ mol^{-1}) leads to a product $C_{10}H_6^+$ ion $\Delta_f H^o_0$ =1457 ± 27 kJ mol^{-1} / $\Delta_f H^o_{298}(C_{10}H_6^+)$ =1432 ± 27 kJ mol^{-1}, which

should correspond to structure **7**, the cycloprop[a]indene radical cation. Loss of an H_2 molecule has an AE_{0K} of 12.86 ± 0.06 eV (1241 ± 6 kJ mol^{-1}), leading to what is an upper limit for the $\Delta_f H^o$ of ion **5** (due to the likely presence of a reverse activation barrier) of $\Delta_f H^o_0$ = 1416 ± 16 kJ mol^{-1} / $\Delta_f H^o_{298}$ =1391 ± 16 kJ mol^{-1}. The fact that this is an upper limit (or indeed, a barrier height to the reaction) is suggested by the comparison of the difference in $\Delta_f H^o$ of the ions $C_{10}H_8$ and $C_{10}H_6$ (**5**) with that between C_6H_6 and C_6H_4 (benzyne). The difference between ions $C_{10}H_8$ and $C_{10}H_6$ (**5**) is 455 kJ mol^{-1}, whereas that between C_6H_6 and C_6H_4 (benzyne) is only 337 kJ mol^{-1},[15] and it is difficult to image why the extra ring system in the $C_{10}H_6$ cation would destabilize the product ion relative to $C_{10}H_8^{+\bullet}$ as compared to the benzene system.

4.3 Conclusion

The dissociation of internal energy-selected ionized naphthalene has been investigated with the use of imaging photoelectron photoion coincidence spectroscopy. Along with tandem mass spectrometry, a more complete picture of the fragmentation pathways has emerged, together with reliable values for bond dissociation activation energies and entropies. Often, the derived entropy of activation was the most helpful value in determining the product ion structure in each pathway, reactions (R1) – (R6). The E_0 values for the reactions are (in eV) 4.20 ± 0.04 (R1), 4.12 ± 0.05 (R2), 4.27 ± 0.07 (R3), 4.72 ± 0.06 (R4), 3.69 ± 0.26 (R5) and 3.20 ± 0.13 (R6). The corresponding $\Delta S^{\ddagger}_{1000}$ values derived in the present study are (in J K^{-1} mol^{-1}) 2 ± 2 (R1), 0 ± 2 (R2), 4 ± 4 (R3), 11 ± 4 (R4), 5 ± 15 (R5), -19 ± 11 (R6). The results were shown to be consistent with the ion structures in Figure 17, with the derived entropies playing a large part in suggesting an appropriate final product structure. The derived E_0 value, combined with the previously

reported IE of naphthalene (8.1442 eV) result in an enthalpy of formation for the naphthyl cation, $\Delta_f H^o_0$ = 1148 ± 14 kJ mol^{-1}/ $\Delta_f H^o_{298}$ = 1123 ± 14 kJ mol^{-1}, slightly lower than the previous estimate by Gotkis and co-workers. The derived E_0 for the second H-loss leads to a $\Delta_f H^o$ for the cycloprop[a]indene radical cation of $\Delta_f H^o_0$ = 1457 ± 27 kJ mol^{-1} / $\Delta_f H^o_{298}(C_{10}H_6^+)$ =1432 ± 27 kJ mol^{-1}. The E_0 for the loss of H_2 was demonstrated by thermochemical arguments to likely correspond to a reverse reaction barrier.

4.4 References for Chapter 4.

1. Ho, Y. P.; Dunbar, R. C.; Lifshitz, C., C-H Bond Strength of Naphthalene Ion - a Reevaluation Using New Time-Resolved Photodissociation Results. *J. Am. Chem. Soc.* **1995,** *117*, 6504-6508.

2. Ruehl, E.; Price, S. D.; Leach, S., Single and Double Photoionization Processes in Naphthalene between 8 and 35 Ev. *J. Phys. Chem.* **1989,** *93*, 6312-6321.

3. Gotkis, Y.; Oleinikova, M.; Naor, M.; Lifshitz, C., Time-Independent Mass Spectra and Breakdown Graphs. 17. Naphthalene and Phenanthrene. *J. Phys. Chem.* **1993,** *97*, 12282.

4. Jochims, H.-W. R., H.; Ruhl, E.; Baumgartel, H.; Leach, S., The Photofragmentation of Naphthalene and Azulene Monocations in the Energy Range 7-22 eV. *Chem. Phys.* **1992,** *168*, 159.

5. Jochims, H.-W. R., H.; Ruhl, E.; Baumgartel, H.; Leach, S., Deuterium Isotope Effects in the Photofragmentation of Naphthalene Monocations. *J. Phys. Chem.* **1993,** *97*, 1312.

6. Laskin, J.; Futrell, J., Internal Energy Distributions Resulting from Sustained Off-Resonance Excitation in Fourier Transform Ion Cyclotron Resonance Mass Spectrometry. II. Fragmentation of the 1-Bromonaphthalene Radical Cation. *J. Phys. Chem. A* **2000,** *104*, 5484-5494.

7. Schroeter, K.; Schroder, D.; Schwarz, C., Structures of the C8h6+ Cation Formed Upon Loss of Acetylene from Ionized Naphthalene. *J. Phys. Chem. A* **1999,** *103*, 4174-4181.

8. Dyakov, Y. A.; Mebel, A. M.; Lin, S. H.; Lee, Y. T.; Ni, C. K., Acetylene Elimination in Photodissociation of Neutral Azulene and Its Cation: An Ab Initio and Rrkm Study. *J. Chin. Chem. Soc.* **2006,** *53*, 161-168.

9. Newby, J. J.; MuÌˆller, C. W.; Liu, C.-P.; Zwier, T. S., Probing E/Z Isomerization on the C10H8 Potential Energy Surface with Ultraviolet Population Transfer Spectroscopy. *J. Am. Chem. Soc.* **2010,** *132*, 1611-1620.

10. Gallup, G. A.; Steinheider, D.; Gross, M. L., A Mechanism for Hydrogen Scrambling in Ionized Benzene. *Int. J. Mass Spectrom. Ion Phys.* **1976,** *22*, 185-188.

11. Jolibois, F.; Klotz, A.; F.-X.Gadéa; Joblin, C., Hydrogen Dissociation of Naphthalene Cation : A Theoretical Study. *Astron. & Astrophys.* **2005,** *444*, 629.

12. Holm, A. I. S.; Johansson, H. A. B.; Cederquist, H.; Zettergren, H., Dissociation and Multiple Ionization Energies for Five Polycyclic Aromatic Hydrocarbon Molecules. *J. Chem. Phys.* **2011,** *134*, 044301.

13. Ervin, K. M.; Ramond, T. M.; Davico, G. E.; Schwartz, R. L.; Casey, S. M.; Lineberger, W. C., Naphthyl Radical: Negative Ion Photoelectron Spectroscopy, Franck−Condon Simulation, and Thermochemistry. *J. Phys. Chem. A* **2001,** *105*, 10822-10831.

14. Cockett, M. C. R.; Ozeki, H.; Okuyama, K.; Kimura, K., Vibronic Coupling in the Ground Cationic State of Naphthalene: A Laser Threshold Photoelectron [Zero Kinetic Energy (ZEKE)-Photoelectron] Spectroscopic Study. *J. Chem. Phys.* **1993,** *98*, 7763.

15. Webbook, N. C., *Nist Standard Reference Database Number 69*. National Institute of Standards and Technology: Gaithersburg, MD: 2005.

16. Gotkis, Y.; Naor, M.; Laskin, J.; Lifshitz, C.; Faulk, J. D.; Dunbar, R. C., Time-Resolved Dissociation of Bromonaphthalene Ion Studied by Tpims and Trpd. Heat of Formation of Naphthyl Ion. *J. Am. Chem. Soc.* **1993,** *115*, 7402-7406.

5 1,2-dihydronapthalene and 9,10-dihydrophenanthrene

5.1 Introduction

Molecular H_2 is the most prolific molecular species found in the interstellar medium (ISM).[1] Whereas it has been long recognized that H_2 is formed on dust grains,[2] investigation of the involved mechanisms is still a very active subject of research.[3-4] One popular theory is that polycyclic aromatic hydrocarbons (PAH) may play a role in the formation of H_2 by acting as catalysts.[5] Atomic hydrogen would adsorb onto the surface of the molecules, thus hydrogenating the PAHs, prior to the desorption of H_2.[6-11] This reaction channel demonstrates the importance of investigating the energetics of not only PAHs but modified PAHs as well, such as hydrogenated species.

Our group has previously studied the energetics of naphthalene cation.[12] It is the simplest example of a PAH molecule and as such has been studied quite extensively.[13-15] It is for this reason that naphthalene would be the base structure of the first hydrogenated molecule studied. Hirama et al. determined that there are three sites which are all likely to adsorb the first superhydrogen atom; this represents the only three sites present on the naphthalene structure as seen in Figure 21A. Of all three sites, position 1 is slightly most favourable for the first hydrogen addition.[7] Going one step further, if we also consider the addition of a second hydrogen atom, it has been shown in larger PAHs that the carbon atom on the outer edge immediately adjacent to the substituted carbon (site 2 in Figure 21a) is the most favourable location.[9] This paper also shows the results of 9,10-dihyrophenanthrene, whose structure is similar to that of 1,2-dihydronaphthalene. As, to date, no energetics information has been found relating to the dissociation of either molecule. We are

presenting them together to determine if their similar structures translates to similar dissociation properties as well.

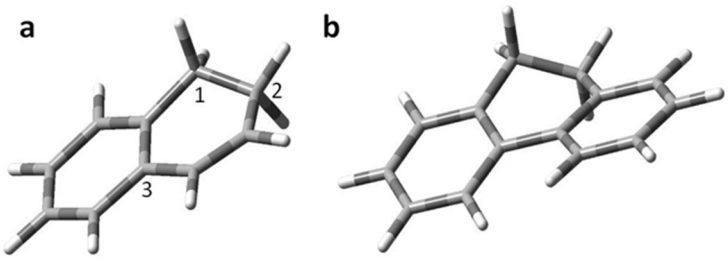

Figure 21: Optimized structures of dihydro-PAHs calculated at B3LYP 6-311G++(d,p) level of theory, the structures are: (a) $C_{10}H_{10}^{+\bullet}$ and (b) $C_{14}H_{12}$, with different carbon sites numbered in order of most favourable site for hydrogen addition.

We have previously obtained the threshold photoelectron spectrum of 1,2-dihydronaphthalene[16] and herein we explore its cation's dissociation reactions and those of 9,10-dihydrophenanthrene cation via mass-analyzed ion kinetic energy spectrometry (MIKES), collision induced dissociation (CID) and metastable ion collision induced dissociation (MI-CID) experiments as well as imaging photoelectron-photoion coincidence (iPEPICO) experiments. The latter technique was performed at the VUV beamline of the Swiss Light Source (SLS) which selects ions as a function of their internal energy with 2 meV photon resolution and measures dissociation rates within the 10^3-10^7 s^{-1} range. This experimental set-up includes a dual acceleration zone. Ions dissociating with the above range of rate constants will do so in the second, low field, region of the acceleration zone resulting in asymmetric time of flight profiles for fragment ions. By fitting the breakdown curves as well as the asymmetric time-of-flight profiles, kinetic modeling of the dissociative ionization processes can be achieved. This allows an accurate determination of barrier heights and entropies of activation that have an impact on dissociation and are useful

parameters for the atmospheric, combustion or interstellar chemistry models to postulate pathways of aromatic formation by hydrogen-abstraction and C_2H_2-addition; as well as the possible catalytic role of PAHs in the ISM.

5.2 Results and discussion

5.2.1 1,2-Dihydronaphthalene: tandem mass spectrometry.

Figure 22a-c show MIKES spectra for the dissociation of 1,2-dihydronaphthalene (DHN, $C_{10}H_{10}^{+\bullet}$) and for its sequential dissociation after the loss of the first hydrogen atom ($C_{10}H_9^+$) and second H atom ($C_{10}H_8^+$).

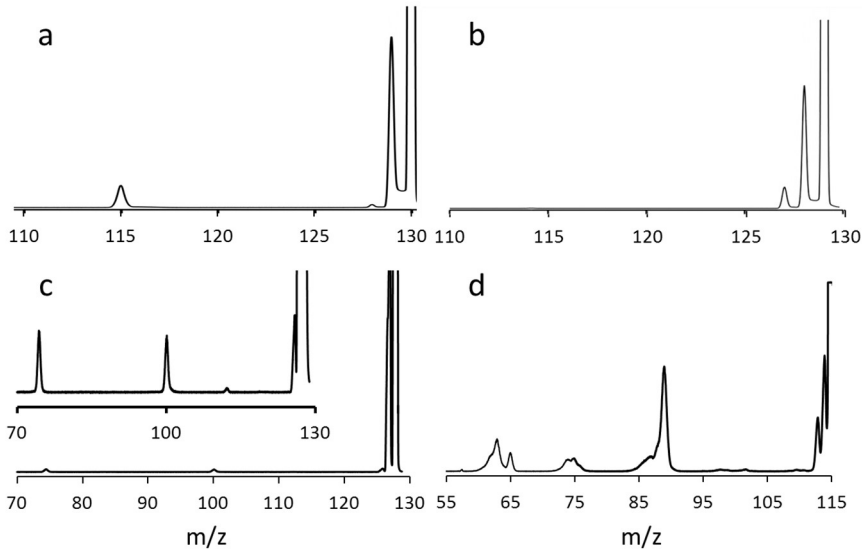

Figure 22: MIKES spectra for various degrees of dehydrogenation of 1,2-dihydronaphthalene; (a) 1,2-dihydronaphthalene (m/z = 130), (b) 1,2-dihydronapthalene-H (m/z = 129), (c) 1,2-dihydronapthalene-2H (m/z = 128) with an insert showing the same spectrum magnified to show the presence of peaks at m/z = 102 and 78, (d) CID mass spectrum of source generated $C_9H_7^+$ from 1,2-dihydronaphthalene (m/z 115)

$C_{10}H_{10}^{+\bullet}$ exhibits two distinct primary dissociation channels, which correspond to reactions R1 and R2;

$$C_{10}H_{10}^{+\bullet} \rightarrow C_{10}H_9^+ + H^\bullet \ (m/z = 129) \qquad (R1)$$

$$C_{10}H_{10}^{+\bullet} \rightarrow C_9H_7^+ + CH_3^\bullet \ (m/z = 115) \qquad (R2)$$

There are also two sequential channels which consist of hydrogen loss from $C_{10}H_9^+$, reactions R3 and R4.

$$C_{10}H_9^+ \rightarrow C_{10}H_8^{+\bullet} + H^\bullet \ (m/z = 128) \qquad (R3)$$

$$C_{10}H_9^+ \rightarrow C_{10}H_7^+ + H_2 \ (m/z = 127) \qquad (R4)$$

The most probable structures for reactions R1-R4 are shown in Figure 23.

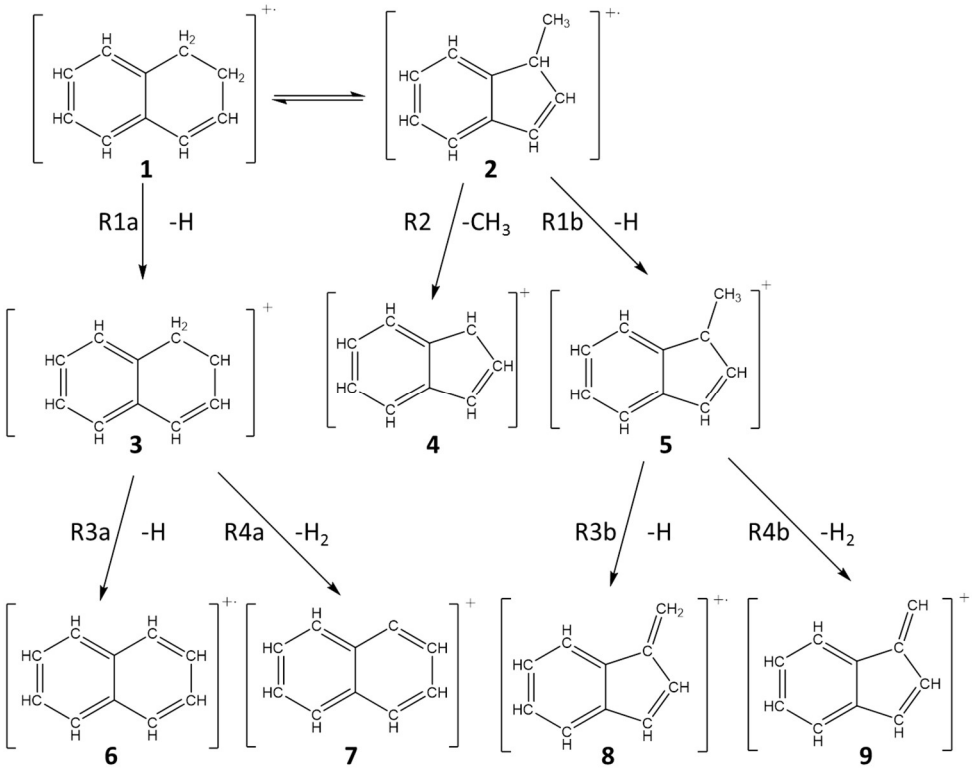

Figure 23: Fragmentation model for 1,2-dihydronaphtalene, outlining most probable structures for reactions 1-4.

For reaction R2, the product ion structure assigned was that of indenyl cation **4**. Indenyl was determined to be the most stable structure as compared to other polycyclic and open structures calculated, as seen in Table 3.

Table 3: Comparison of energies calculated at the B3LYP/6-311+G(d,p) level of theory for the formation of four structures of $C_9H_7^+$ from 1,2-dihydronaphthalene (R2).

$C_9H_7^+$ isomer	ΔE (eV)
indenyl	2.155
tropylacetylene	3.084
tropylcyclobutadiene	3.988
cyclononapentaene	6.060

Thus, included in Figure 23 is the isomerisation of DHN to ionized methylindene (**2**), which itself can undergo H (R1b) and CH_3 loss (R2). In Figure 22d, the CID mass spectrum of m/z 115 demonstrates that the primary fragment appeared at m/z 89, which corresponds to a loss of C_2H_2 from the indenyl cation. This assignment of the indenyl structure is in agreement with work done by Dass and Gross who determined that all $C_{10}H_{10}^{+\bullet}$ isomers produce the same fragment ions after rearranging to a common structure.[17]

While fitting the iPEPICO data, it was observed that there are two competing channels for reaction R1, a low energy channel and a high energy channel. If the isomerisation is considered, then there are two plausible sources for H-loss, the hydrogens attached to the sp3-carbons on the dihydro- structure (R1a) resulting in protonated naphthalene (**3**), and the solitary hydrogen attached to the sp3-carbon on the indene ring of methyl indene (R1b) giving structure **5**.

In the iPEPICO section, it will be shown that all the sequential fragments come from protonated naphthalene (**3**). Starting from protonated naphthalene (**3**), losing a hydrogen atom would likely yield the naphthalene structure **6**. In the case of H_2 loss, the predicted structure is **7**, reported previously by West et al. as the structure of the naphthalene radical cation after the loss of a hydrogen atom.[12] Both of these channels result in the restoration of the planar nature of the molecule and the elimination of sp^3 carbon sites.

MI-CID results indicate that when using source generated ions, there is sufficient energy to see evidence of fragmentation other than from **3.** Starting from **5**, the second sequential H-loss reaction would be the loss of a sp^3-H from the methyl group (R3b) to make 1-methyleneindene (**8)** due to the lower energy requirement. In the case of H_2 loss from **5**, both hydrogen atoms would come from the methyl carbon (R4b) to make **9**. Figure 24 shows a comparison of the MI-CID mass spectra of $C_{10}H_7^+$ ions from 1,2-dihydronaphthalene (**7** and/or **9**) and from naphthalene (**7**).

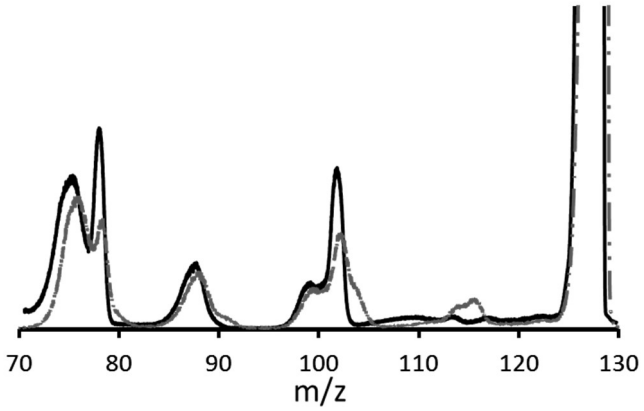

Figure 24: Comparison of the CID mass spectrum of m/z = 127 ($C_{10}H_7^+$) generated from metastable H_2 loss from source generated $C_{10}H_9^+$ ions from 1,2-dihydronaphthalene (broken grey curve, compounds 7 and 9) and from metastable H loss from source generated naphthalene ions (solid black curve- compound **7** only).

All of the features characteristic of structure **7** appear in both traces, with additional peaks present (around 115) assigned to **9.** This indicates the likelihood of a mixture of $C_{10}H_9^+$ ion structures being formed in the ion source of the mass spectrometer for 1,2-dihydronaphthalene. So, both **3** and **5** are formed in the decomposition of high internal energy molecular ions.

5.2.2 1,2-Dihydronaphthalene: iPEPICO spectrometry.

iPEPICO experiments were conducted for photon energies ranging from 10 to 17 eV. All fragments observed in the tandem mass spectrometry experiments for $C_{10}H_{10}^{+\bullet}$ and $C_{10}H_9^+$ were observed, with the sequential channels growing in at approximately 14.3 eV. Figure 25 shows the experimental breakdown curves for all reaction channels.

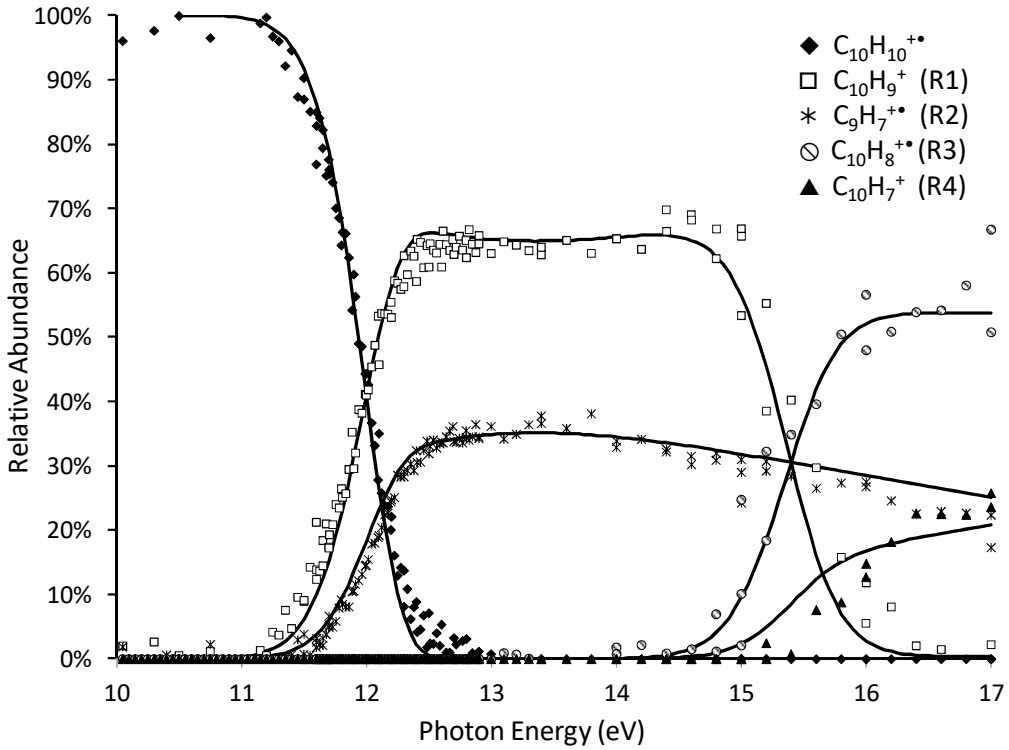

Figure 25: Experimental iPEPICO breakdown curve for the 1,2-dihydronapthalene radical cation over the photon energy range of 10-17 eV. The reaction number for each product channel has been included in parentheses. Calculated fits are overlaid. Derived energetic and entropic parameters can be found in Table 4.

Due to the complex nature of the primary channels, they were fit first while ignoring the sequential channels. The breakdown curves corresponding to the three primary channels were fit together with the asymmetric TOF peak shapes for $C_9H_7^+$ (see computational methods), the latter to aid in the determination of $\Delta^{\ddagger}S$ (the tightness of the transition state). As will be shown later in the section, the sequential channels were fit using a single well model where only R1a is responsible for all sequential dissociations. The fitted breakdown curves can be seen in Figure 25, whereas the fitting of the asymmetric TOF peaks for $C_9H_7^+$ can be seen in Figure 26.

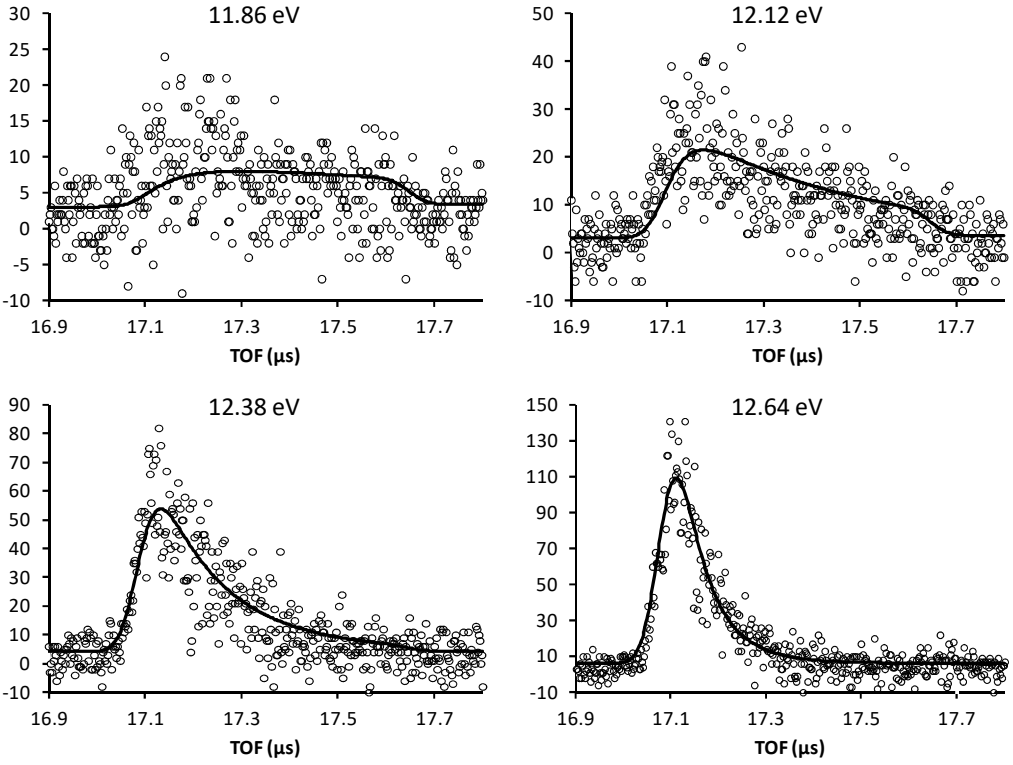

Figure 26: Representative TOF fits, for 1,2-dihydronapthalene, calculated during the RRKM fitting of experimental iPEPICO data. The region shown is the $C_9H_7^+$ region, as this peak was the only asymmetric TOF peak which was not obscured due to its proximity to other peaks. As photon energy increases, it can be seen that the peak becomes increasingly Gaussian in shape.

TOF fitting was only used for the primary channels since all channels exhibit a Gaussian peak shape above 13.4 eV, when the rate constant for dissociation of the precursor ion is greater than 10^6 s^{-1}. The resulting E_0 and $\Delta^{\ddagger}S$ are shown in Table 4.

As stated previously, the primary channels come from two isomers, therefore not only was it necessary to fit the energetics of dissociation, the energy barrier between the two wells also had to be estimated at least. A variety of barriers were used to test the sensitivity of the model in deriving the various dissociation energies and the results are shown in Figure A2 in the appendix. When the isomerisation barrier height was varied between 1.5-2.0 eV, there was very little change in E_0 for all the affected channels. The E_0 values reported in Table 4 are for the average of these values as there is no way to say for certain where exactly the isomerisation barrier lies.

Table 4: Calculated reaction endothermicities and fitted 0K activation energies and entropies of activation for reactions 1-4 of 1,2-dihydronaphthalene.

	B3-LYP/ 6-311++G(d,p)	**RRKM Fit**	
	ΔE (eV)	E_0 (eV)	$\Delta^{\ddagger}S_{1000K}$ (J K^{-1} mol^{-1})
(R1a) $C_{10}H_{10}^{+\bullet} \rightarrow \cdot C_{10}H_9^+ + H$	1.99	2.44 ± 0.10	27 ± 14
(R1b) $C_{10}H_{10}^{+\bullet} \rightarrow \cdot C_{10}H_9^+ + H$	2.39	2.22 ± 0.05	-11 ± 5
(R2) $C_{10}H_{10}^{+\bullet} \rightarrow \cdot C_9H_7^+ + CH_3$	2.24	2.57 ± 0.12	18 ± 11
(R3) $C_{10}H_9^+ \rightarrow \cdot C_{10}H_8^{+\bullet} + H$	3.07	2.72 ± 0.19	9 ± 17
(R4) $C_{10}H_9^+ \rightarrow \cdot C_{10}H_7^+ + H_2$	3.01	2.85 ± 0.10	9 ± 7

The E_0 values for these two competing H loss processes are 2.44 ± 0.10 eV and 2.22 ± 0.05 eV for R1a and R1b respectively. This could indicate that, based solely on E_0, the sequential channels are likely to come from 1-methylindene (R1b). However, when $\Delta^{\ddagger}S$ is factored in, 27 ± 14 J K^{-1} mol^{-1} (R1a) and -11 ± 5 J K^{-1} mol^{-1}(R1b), it can be seen that

reaction R1a quickly becomes the dominant fragmentation channel. This relationship is illustrated in Figure 27; at the appearance energy of the sequential channels, at approximately 14 eV, there is very little contribution from R1b. The energetics extracted for R2 were 2.57 ± 0.12 eV and 18 ± 11 J K^{-1} mol^{-1}, for E_0 and $\Delta^{\ddagger}S$ respectively.

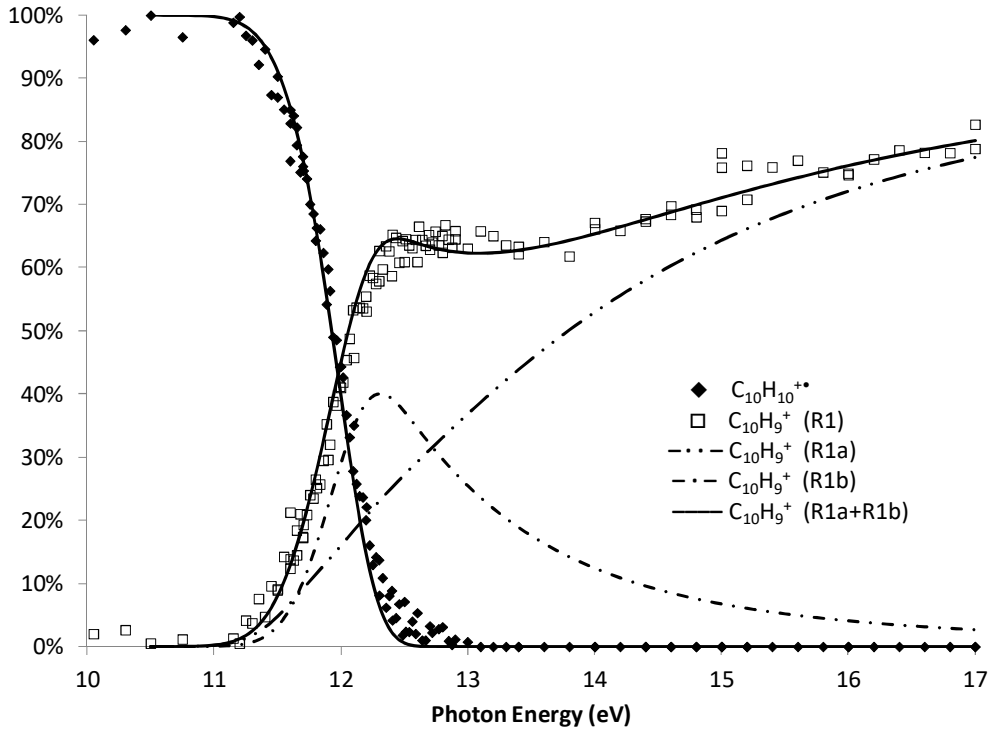

Figure 27: Experimental breakdown diagram for the H loss fragmentation channel for 1,2-diydronaphthalene (R1) over the photon energy range of 10-17 eV. Calculated fits explicitly showing R1a and R1b are overlaid as well as their summation to fit the data.

Due to the assumption that only structure **3** dissociates further, the assignment of the sequential channels becomes quite straightforward. As was alluded to earlier, this assumption allowed for the fitting of these channels using a single-well approximation. For R3, a literature value (calculated at the B3LYP/6-311++G(d,p) level of theory) for the loss of a hydrogen atom from protonated naphthalene (protonated in the 1 position) was found to

be 2.71 eV which is in excellent agreement with the present RRKM value of 2.72 ± 0.19 eV.[18] This supports the current results that R3 is only produced from the protonated naphthalene cation. The loss of H_2 from protonated naphthalene was calculated at the same level of theory to be 3.02 eV. This is similar to the present RRKM value 2.85 ± 0.10 eV. The RRKM $\Delta^{\ddagger}S$ values for R3 and R4 are 9 ± 17 and 9 ± 7 $JK^{-1}mol^{-1}$. It was not possible to find any literature values with which to compare; however, as these channels result in the loss of H and H_2 presumably by bond cleavage reactions, a slightly positive $\Delta^{\ddagger}S$ is not unexpected.

5.2.3 9,10-Dihydrophenanthrene: tandem mass spectrometry.

Figure 28 shows the MIKES spectrum for the dissociation of 9,10-dihydrophenanthrene (DHP, $C_{14}H_{12}^{+\bullet}$).

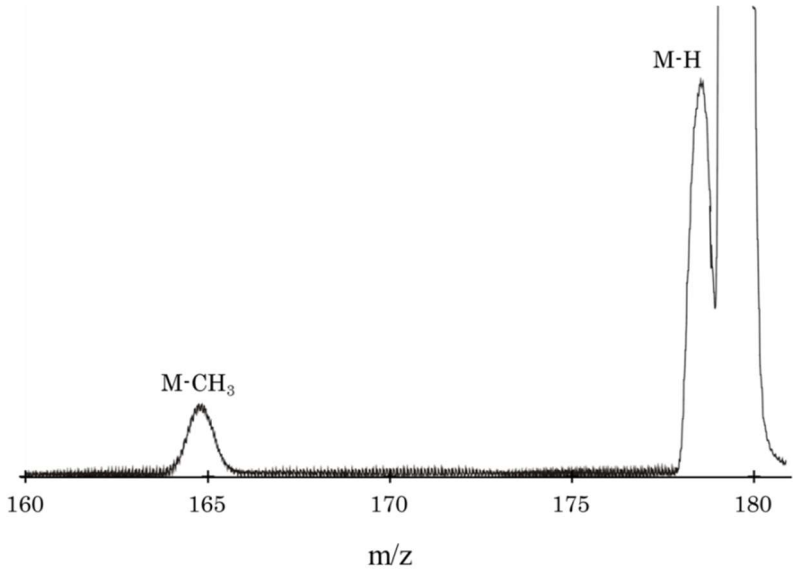

Figure 28: MIKES spectrum of 9,10-dihydrophenanthrene. Only two metastably generated fragments are observed, corresponding to the loss of hydrogen (m/z 179) and the loss of methyl radical (m/z 165).

Similar to 1,2-dihydronaphthalene, only two fragments are present; one resulting from the loss of hydrogen ($C_{14}H_{11}^+$) as well as the loss of a methyl radical ($C_{13}H_9^+$). These fragments correspond to reactions R5 and R6;

$$C_{14}H_{12}^{+\bullet} \rightarrow C_{14}H_{11}^+ + H^\bullet \ (m/z = 179) \qquad (R5)$$

$$C_{14}H_{12}^{+\bullet} \rightarrow C_{13}H_9^+ + CH_3^\bullet \ (m/z = 165) \qquad (R6)$$

The predicted structures for these fragments are shown in Figure 29.

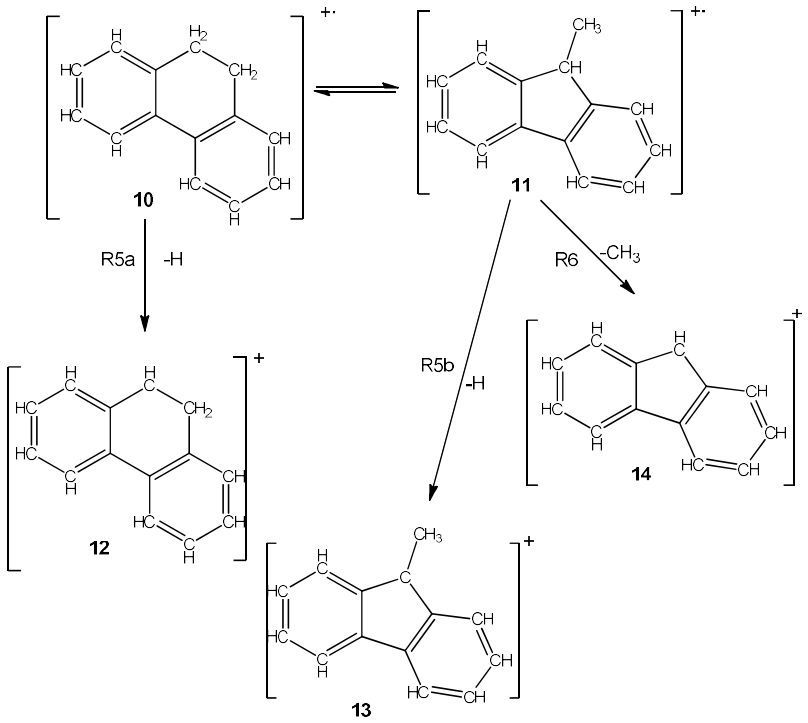

Figure 29: Fragmentation model for 9,10-dihydrophenanthrene, outlining the most probable structures for reactions 5-6.

No literature was found for the fragmentation of ionized 9,10-dihydrophenanthrene, so the structures are based on those predicted for ionized 1,2-dihydronaphthalene as both molecules have similar starting structures and, as will be discussed later, the behaviour of

the two systems are comparable. Reaction R6 was assigned the fluorenyl structure (**11**), based partially on the results from calculations for 1,2-dihydronaphthalene where the indenyl structure was determined to be the most stable. Thus, the isomerisation of DHP to 9-methylfluorene must take place during the unimolecular chemistry of DHP. To test this assumption, the MI-CID mass spectra for m/z 165 was compared between the methyl loss from 9,10-dihydrophenanthrene and the hydrogen loss from fluorene. These results can be seen in Figure 30 which shows perfect agreement between the two mass spectra.

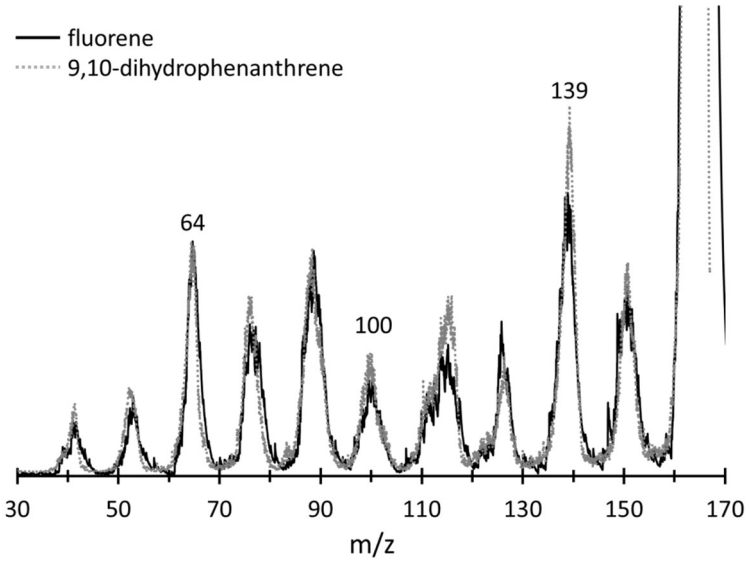

Figure 30: Comparison of m/z = 165 generated by the methyl loss from (broken grey curve) 9,10-dihydrophenanthrene and by the hydrogen loss from fluorene ($C_{13}H_{10}^{+}$) (solid black curve).

This indicates that m/z 165 from both molecules result in the same structure. Since fluorene only lost a hydrogen atom it is likely that the resulting structure would be very similar to that of the precursor ion.

As was observed with ionized dihydronaphthalene, there are two possible channels for H atom loss. Thus, reaction R5 has been split into two competing channels, a channel due to

loss of H from an sp^3 carbon on DHP (R5a) to form **12** and one due to loss of H from 9-methylfluorene (R5b) to form **13**.

5.2.4 9,10-Dihydrophenanthrene: iPEPICO spectrometry.

iPEPICO experiments were conducted for photon energies ranging from 10 – 17 eV. All fragments observed in the tandem mass spectrometry experiments for $C_{14}H_{12}^{+\bullet}$ were observed; there were no consecutive reaction channels observed in the given energy range. Figure 31 shows the experimental and fitted breakdown curves for the three reaction channels.

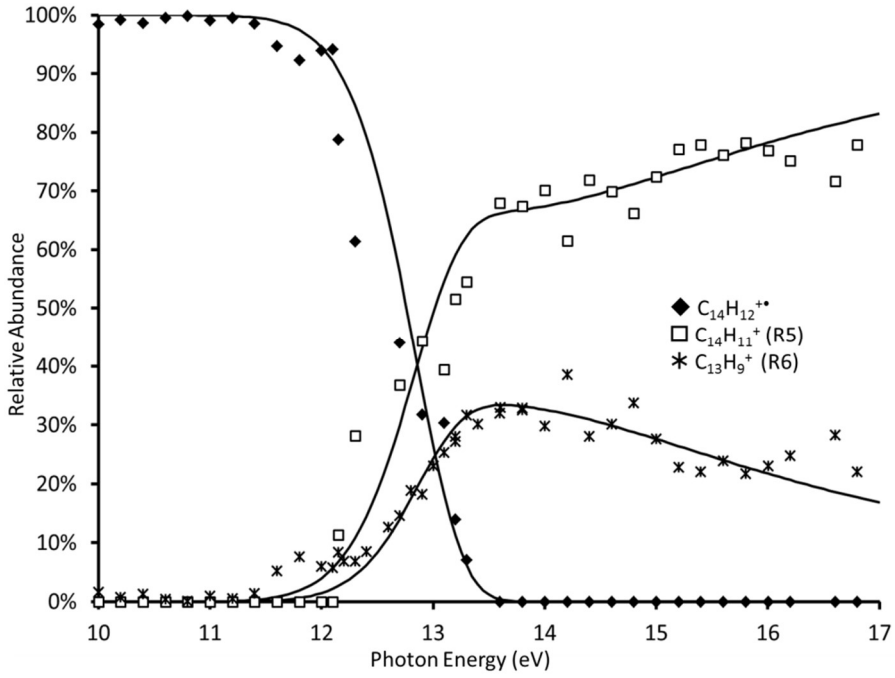

Figure 31: Experimental breakdown curve for the 9,10-dihydrophenanthrene radical cation over the photon energy range of 10-17 eV. The reaction number for each product channel has been included in parentheses. Calculated fits are overlaid. Derived energetic and entropic parameters can be found in Table 5.

TOF fitting of the $C_{13}H_9^+$ peak was used to aid in the assignment of the reactions channels, similarly to 1,2-dihydronaphthalene (Figure A3). There is a hint of a second, fast component on the TOF distributions as shown in Figure 31, which would indicate that an isomerisation pathway opens up at or close to the dissociation threshold. The data quality is insufficient to attempt fitting a two-well model to model the dissociation. The RRKM E_0 and $\Delta^{\ddagger}S$ values are shown in Table 5.

Table 5: Calculated reaction endothermicities and 0K activation energies and entropies of activation for reactions R5 and R6 of 9,10-dihydrophenanthrene.

	B3-LYP/ 6-311++G(d,p)	**RRKM Fit**	
	ΔE (eV)	E_0 (eV)	$\Delta^{\ddagger}S$ (J K^{-1} mol^{-1})
(R5a) $C_{14}H_{12}^{+\bullet} \rightarrow C_{14}H_{11}^{+} + H$	2.23	2.37 ± 0.12	18 ± 19
(R6) $C_{14}H_{12}^{+\bullet} \rightarrow C_{13}H_9^{+} + CH_3$	1.98	2.38 ± 0.15	-3 ± 15

When fitting reaction R5 it quickly became apparent that it was not necessary to fit the H loss using two channels as was done with 1,2-dihydronaphthalene. Two distinct reactions were necessary, however, to fit R6 correctly, and this was taken to be evidence of the need to incorporate an isomerisation reaction to methylfluorene. As done previously, a range of isomerisation barriers were used for the fitting to determine how sensitive the channels are to isomerisation (Figure A4). For R5, we obtained an E_0 value of 2.37 ± 0.12 and a $\Delta^{\ddagger}S$ value of 18 ± 19 $JK^{-1}mol^{-1}$. While there is no literature data for comparison, these values are in between those found for R1a and R1b in 1,2-dihydronaphthalene. The final reaction channel for 9,10-dihydrophenanthrene is reaction R6 at E_0 2.38 ± 0.15 eV and $\Delta^{\ddagger}S$ -3 ± 15 $JK^{-1}mol^{-1}$.

5.3 Conclusion

Comparing the two molecules presented in this paper, it can be seen that both size and ring geometry plays a role in the energetics of the dissociation channels investigated. While molecular size has little effect on the C-H bond dissociation energy of ionized PAHs, their energy remaining between 4.60 - 4.65 eV when increasing in size from benzene through naphthalene to phenanthrene;[19] as soon as the molecule is protonated, the size effect becomes apparent with the bond dissociation energy decreasing as the ring system expands, starting at 3.29 eV for protonated benzene and decreasing to 2.71eV for protonated naphthalene and decreasing further to 2.57 eV for protonated phenanthrene.[18] This trend can be extrapolated even further to the dihydro-PAHs when the C-H bond dissociation energies determined in this work are considered; 2.44 ± 0.10 for 1,2-dihydronaphthalene (R1a) and 2.37 ± 0.10 eV for 9,10-dihydrophenanthrene (R5). The presence of a second sp^3 carbon site has further decreased the C-H bond dissociation energy to facilitate the restoration of the unaltered PAH ion.

It is interesting to note that at no point is the loss of H_2 observed from 9,10-dihydrophenanthrene cation, and only as a secondary channel from 1,2-dihydronaphthalene cation. This is in keeping with what has previously been reported in the literature where the loss of H_2 is mainly observed from neutral and protonated species, such as protonated 1,2-dihydronaphthalene,[10] 9,10-dihydrophenanthrene[20] as well as protonated PAHs, but not from radical cations.[18] As a result, it may be unlikely that small PAHs catalyze H_2 formation in ionic environments, in which H + H addition is more likely to result in isomerisation and methyl group formation.

No direct comparisons can be made for the secondary channels from ionized 1,2-dihydronaphthalene (R3 and R4) since these channels were not observed in the iPEPICO spectra of ionized 9,10-dihydrophenanthrene in the studied energy range. The energetics measured, 2.72 ± 0.19 eV (R3) and 2.85 ± 0.10 eV (R4), are in good agreement with calculated values found in the literature.[18] And while there were no literature values found for $\Delta^{\ddagger}S$, the values of 9 ± 17 J K^{-1} mol^{-1} (R3) and 9 ± 7 J K^{-1} mol^{-1} (R4) are reasonable for bond cleavage reactions involving little to no reverse energy barrier.

5.4 References for Chapter 5

1. Carruthers, G. R., Rocket Observation of Interstellar Molecular Hydrogen. *ApJL* **1970,** *161*, L81.

2. Gould, R. J. a. S., E. E., The Interstellar Abundance of the Hydrogen Molecule. I. Basic Processes. *ApJL* **1963,** *138*, 393-407.

3. Lemaire, J. L.; Vidali, G.; Baouche, S.; Chehrouri, M.; Chaabouni, H.; Mokrane, H., Competing Mechanisms of Molecular Hydrogen Formation in Conditions Relevant to the Interstellar Medium. *The Astrophysical Journal Letters* **2010,** *725*, L156.

4. Cazaux, S. M., S.; Spaans, M. and Allouche, A., When Sticking Influences H2 Formation. *Astronomy & Astrophysics* **2011,** *535*, A27-A36.

5. Joblin, C.; Tielens, A. G. G. M., *PAHs and the Universe: A Symposium to Celebrate the 25th Anniversary of the Pah Hypothesis*. EAS Publications Series: 2011; Vol. 46.

6. Cassam-Chenaï, P.; Pauzat, F.; Ellinger, Y., Is Stripping of Polycyclic Aromatic Hydrocarbons a Route to Molecular Hydrogen? In *Molecules and Grains in Space, 50th International Meeting of Physical Chemistry*, Nenner, I., Ed. American Institute of Physics Press: Mont Sainte-Odile, France, 1994; Vol. 312, p 543.

7. Hirama, M.; Tokosumi, T.; Ishida, T.; Aihara, J.-i., Possible Molecular Hydrogen Formation Mediated by the Inner and Outer Carbon Atoms of Typical PAH Cations. *Chem. Phys.* **2004,** *305*, 307-316.

8. Bauschlicher, C. W., The Reaction of Polycyclic Aromatic Hydrocarbon Cations with Hydrogen Atoms: The Astrophysical Implications. *The Astrophysical Journal Letters* **1998,** *509*, L125.

9. Rauls, E.; Hornekær, L., Catalyzed Routes to Molecular Hydrogen Formation and Hydrogen Addition Reactions on Neutral Polycyclic Aromatic Hydrocarbons under Interstellar Conditions. *The Astrophysical Journal* **2008,** *679*, 531.

10. Vala, M.; Szczepanski, J.; Oomens, J.; Steill, J. D., H2 Ejection from Polycyclic Aromatic Hydrocarbons: Infrared Multiphoton Dissociation Study of Protonated 1,2-Dihydronaphthalene. *J. Am. Chem. Soc.* **2009,** *131*, 5784-5791.

11. Thrower, J. D.; Jørgensen, B.; Friis, E. E.; Baouche, S.; Mennella, V.; Luntz, A. C.; Andersen, M.; Hammer, B.; Hornekær, L., Experimental Evidence for the Formation of Highly Superhydrogenated Polycyclic Aromatic Hydrocarbons through H Atom Addition and Their Catalytic Role in H2 Formation. *The Astrophysical Journal* **2012,** *752*, 3.

12. West, B.; Joblin, C.; Blanchet, V.; Bodi, A.; Sztáray, B.; Mayer, P. M., On the Dissociation of the Naphthalene Radical Cation: New iPEPICO and Tandem Mass Spectrometry Results. *J. Phys. Chem. A* **2012,** *116*, 10999-11007.

13. Ho, Y. P.; Dunbar, R. C.; Lifshitz, C., C-H Bond Strength of Naphthalene Ion - a Reevaluation Using New Time-Resolved Photodissociation Results. *J. Am. Chem. Soc.* **1995,** *117*, 6504-6508.

14. Laskin, J.; Futrell, J., Internal Energy Distributions Resulting from Sustained Off-Resonance Excitation in Fourier Transform Ion Cyclotron Resonance Mass Spectrometry. II. Fragmentation of the 1-Bromonaphthalene Radical Cation. *J. Phys. Chem. A* **2000,** *104*, 5484-5494.

15. Gotkis, Y.; Oleinikova, M.; Naor, M.; Lifshitz, C., Time-Independent Mass Spectra and Breakdown Graphs. 17. Naphthalene and Phenanthrene. *J. Phys. Chem.* **1993,** *97*, 12282.

16. Mayer, P. M.; Blanchet, V.; Joblin, C., Threshold Photoelectron Study of Naphthalene, Anthracene, Pyrene, 1,2-Dihydronaphthalene, and 9,10-Dihydroanthracene. *J. Chem. Phys.* **2011,** *134*, 244312.

17. Dass, C.; Gross, M. L., A Mass-Spectrometry Mass-Spectrometry Investigation of the Nature of [C10H10]+, [C9H7]+ and [C10H8]+ Gas-Phase Ions. *Org. Mass Spectrom.* **1983,** *18*, 542-546.

18. Kapinus, V. A. Photophysical Properties of Protonated Aromatic Hydrocarbons. California Institute of Technology, 2004.

19. Fujiwara, K.; Harada, A.; Aihara, J.-i., CH Bond Dissociation Energies of Polycyclic Aromatic Hydrocarbon Molecular Cations: Theoretical Interpretation of the (M-1)+ Peak in the Mass Spectra. *J. Mass Spectrom.* **1996,** *31*, 1216-1220.

20. Szczepanski, J.; Oomens, J.; Steill, J. D.; Vala, M. T., H2 Ejection from Polycyclic Aromatic Hydrocarbons: Infrared Multiphoton Dissociation Study of Protonated Acenaphthene and 9,10-Dihydrophenanthrene. *The Astrophysical Journal* **2011,** *727*, 12.

6 Anthracene

6.1 Introduction

There has been some work previously conducted on the anthracene radical cation and its isomer, the phenanthrene radical cation. Ling *et al.* completed a thorough study of their fragmentation which included both experimental results outlining the dissociation and theoretical calculations for the determination of the molecular structure for the fragment ions.[1-2] In one study, photoionization results were used to determine the main dissociation channels for the two $C_{14}H_{10}^{+\cdot}$ ions: H-loss, 2H and H_2 loss, acetylene loss as well as larger organic neutral losses (C_3H_3 and C_4H_2) and these reactions are also observed as sequential losses from larger fragments. They were able to determine kinetic data (activation energies and entropies of activation) for all reactions using RRKM fitting.[1] In the same paper, mass-analyzed ion kinetic energy spectrometry (MIKES) results were also discussed, primarily focusing on the dished top peak shape observed for $C_{12}H_8^{+\cdot}$. This result led to the presumption that the acetylene loss channel was defined by a tight transition state and large reverse energy barrier which would explain the kinetic energy release observed. Another observation was that both anthracene and phenanthrene possessed this same dished top peak, the authors describing them as indistinguishable, and therefore it was assumed likely that ionized anthracene first isomerised to ionized phenanthrene prior to C_2H_2 loss. Their other study focused on elucidating the structure of the $C_{12}H_8^{+\cdot}$ fragment through computational modelling.[2] Six different structures were proposed and their dissociation energies were calculated at two different levels of theory (B3LYP/cc-pVDZ and B3PW91/cc-pVDZ) and the energies were then compared to the experimental results. Based on this comparison, it

was determined that the likely structure of $C_{12}H_8^{+\cdot}$ would be that of ionized biphenylene, which supports the assumption that both anthracene and phenanthrene radical cations would have to isomerise to a common structure, in this case ionized phenanthrene, prior to dissociation. Based on the results found by Ling, Johansson *et al*. did further high energy collision-induced dissociation (CID) experiments as well as calculations to determine the reaction surface starting from the anthracene radical cation to three of the structures predicted by Ling: taking acetylene from an outer ring to form ionized ethynylnaphthalene, the formation of ionized biphenylene via phenanthrene ions and also calculating the formation of acenaphthylene ions (the lowest energy structure from Ling et al.) from ionized phenanthrene.[3] They stated that that since acenaphthylene had the lowest reaction barrier, it should be the most heavily weighted structure for this reaction, but all the structures proposed were close enough in energy that they might also contribute.

As the molecular weight of the PAHs increases, their vapour pressures generally decrease, making it progressively more difficult to explore the dissociative photoionization of large PAHs with techniques such as iPEPICO, though molecules as large as $C_{42}H_{18}$ have been studied by high temperature evaporation.[4] Atmospheric pressure chemical ionization (APCI) is an alternative approach to the production of gas-phase ions of non-polar compounds such as anthracene. When coupled with a triple-quadruple mass spectrometer, energy resolved collision-induced dissociation mass spectrometry can be employed, and modeled, to derive similar information: fragmentation pathways and unimolecular reaction energetics and entropies, derived by modeling the experimental data with statistical rate theories such as RRKM theory.[5-8] Once RRKM *k(E)* values are obtained, branching ratios as a function of ion internal energy can be calculated. Our previous work in this area

employed a simple model in which the post-collision ions are assigned an effective temperature depending on the centre-of-mass collision energy, and thus a "thermal" internal energy distribution, according to the relationship in equation 3.5. This is clearly the "Achilles heel" of the present model and thus we previously only attempted to derive relative energetics and entropies for the systems under study. One of our goals in this study is to compare the results of the modeling of iPEPICO fragmentation data with those from the modeling of the CID breakdown curves to determine the consistency between the two approaches for studying these ions, and the suitability of the internal energy distribution approximation being made in our model, the basic question being: just how similar to a Boltzmann distribution is the post-collision internal energy distribution of the ions in this study?

Numerous qualitative and quantitative approaches have been described to address this issue depending on the nature of the experiment.[9] The most successful have been for slow-heating methods such as CID performed in ion traps,[10-17] CID and surface-induced dissociation in FT-ICR[18-24] and single–collision threshold measurements.[25-27] A number of studies have explored this relationship under multiple collision conditions in a quadrupole collision cell.[28-31] While there is no evidence for the linear scaling of the effective temperature with E_{com} shown in Eq. 1, it may still be a reasonable first-order approximation thanks to the small absolute range of E_{com} exhibited in the breakdown diagram. Knyazev and Stein[32-33] have recently demonstrated that post-collision ion internal energy distributions can indeed be non-Boltzmann in character. In their reported case for the small benzylammonium ion, the P(E) of the ions at E_{lab} = 10 eV (E_{com} = 2.7 eV) appears more like a pure Boltzmann distribution shifted up along the internal energy axis (Fig. 6 in ref. 35).

The discrepancy between the modeled distribution and a thermal distribution increased with increasing collision energy. This would clearly draw into doubt our use of a thermal distribution to approximate the P(E) of ionized anthracene. In the end, this assumption in our model will be tested by determining if a suitable fit to the experimental data can be obtained, and if that fit results in acceptable kinetic values of E_0 and $\Delta^{\ddagger}S$, when compared to the iPEPICO results.

If APCI-CID is shown to be a suitable alternative, it opens the door for the study of larger molecules which cannot currently be investigated using iPEPICO due to volatility issues. Such molecules- are of great interest in the astrochemical field as they are the most likely candidates to be found in the actual interstellar environment due to their photostability.[34]

The threshold photoelectron spectrum for anthracene has been obtained previously.[35] The potential structures for the fragmentation of the anthracene radical cation are proposed based on mass-analyzed ion kinetic energy spectrometry (MIKES) results, both from the current research and from literature.[1] Both iPEPICO and APCI-CID results are being presented together; first the iPEPICO results are discussed and compared to literature to get an idea on the accuracy of the values obtained, followed by the APCI-CID results to see how the values compare for the determination of the validity of technique.

6.2 Results and discussion

6.2.1 MIKES mass spectrometry

MIKES experiments revealed three reactions (R1-3) for the unimolecular dissociation of the anthracene radical cation and its H-loss product ion:

$$C_{14}H_{10}^{+\cdot} \rightarrow C_{14}H_9^+ + H \quad \text{(R1)}$$

$$C_{14}H_9^+ \rightarrow C_{14}H_8^{+\cdot} + H \quad \text{(R2)}$$

$$C_{14}H_{10}^{+\cdot} \rightarrow C_{12}H_8^{+\cdot} + C_2H_2 \quad \text{(R3)}$$

These results were in keeping with what was found previously for the naphthalene radical cation.[36] The peaks for both $C_{14}H_9^+$ and $C_{14}H_8^{+\cdot}$ were Gaussian in shape, whereas our observed peak for $C_{12}H_8^{+\cdot}$ was broader with a dished top. This peak shape is supported by the results of Ling and Lifshitz who observed a similar metastable peak shape in their experiments.[1] Both results are indicative of a reverse energy barrier for this channel and that the transition state for reaction R3 would likely correspond to a rearrangement reaction, and thus an entropically unfavorable "tight" transition state.

Assigning product ion structures for reactions R1 and R2 was quite straightforward. The fragmentation map, with all proposed structures, is shown in Figure 32.

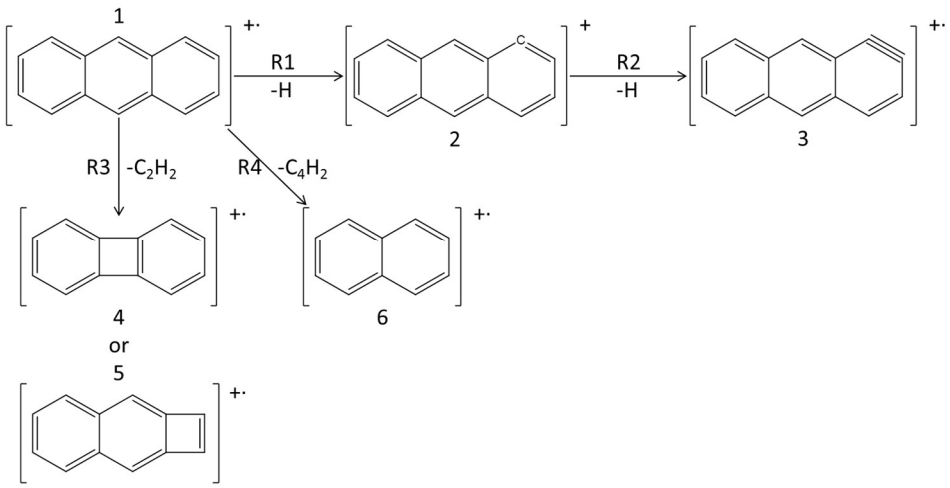

Figure 32: Reaction scheme for the unimolecular dissociation of anthracene radical cation. Reactions R1-3 were observed via MIKES and iPEPICO experiments while reactions R1, 2 and 4 were observed only in APCI experiments.

In the previous study of the naphthalene radical cation, it was shown that due to hydrogen scrambling, all hydrogen sites are equally likely to be dehydrogenated.[36] For this reason, structures **2** and **3** were assigned to $C_{14}H_9^+$ and $C_{14}H_8^{+\cdot}$. The structure assignment for $C_{12}H_8^{+\cdot}$ has undergone more debate. As stated, based on the shape of the metastable peak, and the indication of a reverse activation energy barrier,[1] it is likely that the structure will involve some degree of rearrangement. However, Ling and Lifshitz derived a $\Delta^{\ddagger}S$ of over 50 J K^{-1} mol^{-1} from their kinetic modeling, indicative of a loose transition state. Ling, Martin and Lifshitz calculated six potential product ions, covering both open and closed ring structures, at two different levels of theory (B3LYP/cc-PVDZ and B3PW91/cc-pVDZ).[2] They compared the calculated dissociation energies with experimental values in order to determine which structure was the most probable. The results determined that, while acenaphthylene (**6**) was the lowest energy structure, biphenylene (**4**) was closest to the experimental dissociation energies. Cyclobuta[b]naphthalene (**5**), the analogous product ion to that for C_2H_2 loss from ionized naphthalene, was excluded because its calculated energy

was too high. These results inspired another study, conducted by Johansson et al., which explored the potential energy surface for acetylene loss from the anthracene radical cation.[3] The product structures explored were; 2-ethynylnaphthalene (**7**), biphenylene (**4**) and acenaphthylene (**6**), with cyclobuta[b]naphthalene (**5**) not being considered due to the conclusions drawn by Ling et al. [2] All calculations were conducted at the B3-LYP/6-311++G(2d,p) level of theory. The results for 2-ethynylnaphthalene (**7**), which had already been ruled out due to the dished peak shape from Ling's MIKES study,[1] indicate that the highest lying transition state towards its formation is at 4.99 eV. For the biphenylene ion structure (**4**), where anthracene first isomerizes to phenanthrene, the highest point on the potential energy surface was calculated to be 5.64 eV, whereas the energy requirement for isomerisation was 4.89 eV. For the formation of acenaphthylene (**6**), which was only calculated from the phenanthrene precursor ion, the maximum energy was 4.95 eV. Based on these results, there are a few problems with choosing a final structure. Both the formation of acenaphthylene (**6**) and biphenylene (**4**) require the isomerisation of the anthracene radical cation to the phenanthrene radical cation. Since the formation of acenaphthylene was calculated to be more than 0.5 eV lower in energy than required for biphenylene, based on these calculations, the likelihood of forming the latter is should be quite low. Another problem, which will become apparent in the next section, is that when fitting the current experimental data, all three energies calculated by Johansson et al. (4.99, 5.64 and 4.95 eV)[3] are significantly higher than what was determined from the iPEPICO results (~4.2 eV). In the end, two structures are presented here as possible structures for $C_{12}H_8^{+\cdot}$, biphenylene (**4**) and cyclobuta[b]naphthalene (**5**). These structures were chosen based on the results of the naphthalene radical cation study where it was determined that

acetylene loss in this system resulted in the formation of benzocyclobutene, and both these proposed structures are analogous.[36] Neither the Ling study nor that by Johansson firmly rule out either possibility, and both are in keeping with the current observations.

6.2.2 iPEPICO

iPEPICO experiments were conducted over a photon energy range of 15 – 22 eV. The fragments observed correspond to reactions R1-3 from the MIKES results, the consecutive H loss (R2) appears at around 17 eV as seen in Figure 33.

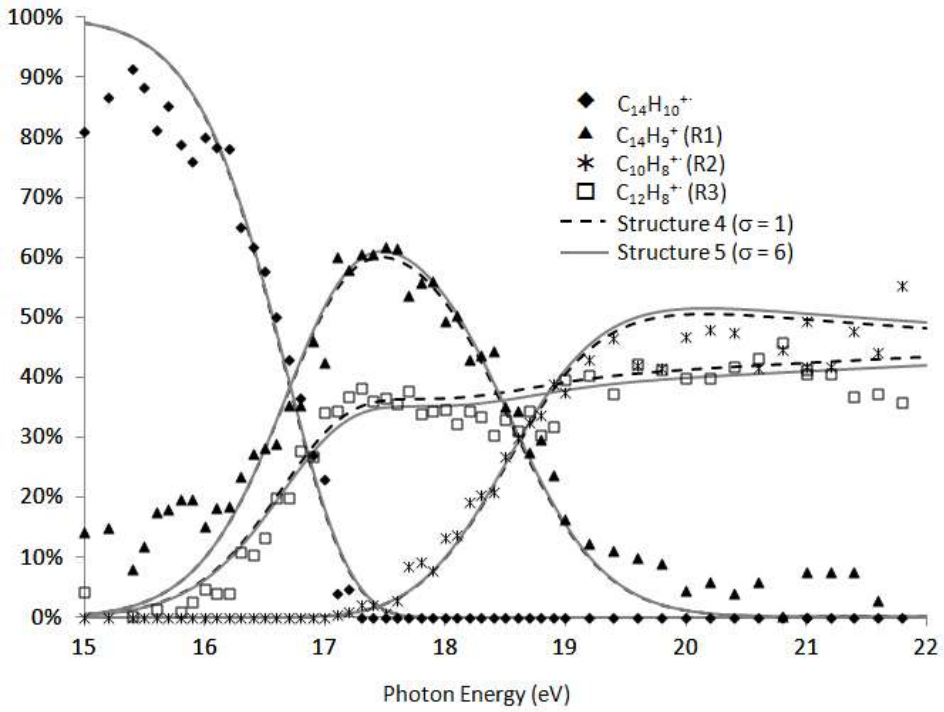

Figure 33: iPEPICO breakdown diagram and fitting illustrating the effect of using structure 4 (black broken line) versus structure 5 (solid grey line) for the calculation of $C_{12}H_8^{+\bullet}$.

Similarly to what was observed for the naphthalene radical cation, there was a rise in intensity observed for reaction R2, which could be attributed to acetylene loss from

$C_{14}H_9^+$.[36] However, the change is quite subtle and therefore it was not possible to fit this channel reliably and is thus not included in this discussion.

A technique similar to that used in the naphthalene radical cation fitting was employed here: the primary channels were fit first, using both the experimental breakdown curves and the asymmetric TOF peaks for $C_{12}H_8^{+\cdot}$, followed by the fitting for the sequential dehydrogenation channel, R2.[36] The results of the fitting can be seen in Figure 33, with the calculated curves superimposed on the experimental data. The asymmetric TOF fits for $C_{12}H_8^{+\cdot}$ can be seen in Figure A3 of appendix to demonstrate the quality of the fitting. The kinetic data, E_0 and $\Delta^{\ddagger}S$, extracted from these fits are summarized in Table 6 and Table 7.

Table 6: 0K activation energies (E_0/eV) determined by iPEPICO and APCI-CID experiments as well as comparison to literature values.

		iPEPICO[a]	iPEPICO[b]	APCI-CID[a]	APCI-CID[b]	literature[c]
$C_{14}H_{10}^{+\cdot} \rightarrow C_{14}H_9^+ + H$	(R1)	4.28 ± 0.29	4.28 ± 0.30	4.55 ± 0.10	4.55 ± 0.10	4.38 ± 0.1
$C_{14}H_9^+ \rightarrow C_{14}H_8^{+\cdot} + H$	(R2)	2.71 ± 0.19	2.71 ± 0.20	---	---	2.85 ± 0.2
$C_{14}H_{10}^{+\cdot} \rightarrow C_{12}H_8^{+\cdot} + C_2H_2$	(R3)	4.21 ± 0.30	4.19 ± 0.30	4.18 ± 0.10	4.17 ± 0.06	4.50 ± 0.1
$C_{14}H_{10}^{+\cdot} \rightarrow C_{10}H_8^{+\cdot} + C_4H_2$	(R4)	---	---	4.87 ± 0.30		4.46 ± 0.1

[a] experiments assuming structure (**5**)
[b] experiments assuming structure (**4**)
[c] literature values obtained by Ling and Lifshitz[1]

Table 7: Entropy of activation ($\Delta^{\ddagger}S$/JK^{-1}mol^{-1}) determined by iPEPICO and APCI-CID experiments as well as comparison to literature values.

		iPEPICO[a]	iPEPICO[b]	APCI-CID[a]	APCI-CID[b]	literature[c]
$C_{14}H_{10}^{+\cdot} \rightarrow C_{14}H_9^+ + H$	(R1)	12 ± 15	13 ± 15	13 ± 2	13 ± 2	24.7 ± 4
$C_{14}H_9^+ \rightarrow C_{14}H_8^{+\cdot} + H$	(R2)	0 ± 15	1 ± 15	---	---	-8.4 ± 8
$C_{14}H_{10}^{+\cdot} \rightarrow C_{12}H_8^{+\cdot} + C_2H_2$	(R3)	7 ± 10	22 ± 10	-1 ± 6	12 ± 3	53.6 ± 4
$C_{14}H_{10}^{+\cdot} \rightarrow C_{10}H_8^{+\cdot} + C_4H_2$	(R4)	---	---	23 ± 8	23 ± 8	8.4 ± 4

[a] experiments assuming structure (**5**)
[b] experiments assuming structure (**4**)
[c] literature values obtained by Ling and Lifshitz.[1]

For reaction R1, the values obtained for E_0 and $\Delta^{\ddagger}S$, 4.28 ± 0.29 eV and 12 ± 15 J K^{-1} mol^{-1}, respectively, are in quite good agreement with the results for the equivalent channel

from the naphthalene radical cation (4.20 ± 0.04 eV and 2 ± 2 J K^{-1} mol^{-1}).[36] This agrees with previous observations that all PAHs of similar design (in this case catacondensed) will have similar chemical properties.[37] The positive value for $\Delta^{\ddagger}S$ is also in keeping with the nature of the reaction being a simple bond cleavage which should require minimal molecular rearrangement. These values are also found to be in good agreement with those in the literature, 4.38 ± 0.1 eV and 24.7 ± 4 J K^{-1} mol^{-1} from Ling and Lifshitz, respectively, with good overlap between the two sets when uncertainties are taken into account.[1]

The values obtained here for R2, E_0 of 2.71 ± 0.19 eV and $\Delta^{\ddagger}S$ of 0 ± 15 J K^{-1} mol^{-1}, are again in keeping with the results found by Ling (2.85 ± 0.2 eV and -8.4 ± 8 $JK^{-1}mol^{-1}$). Unlike reaction R1, these values are not quite as close to those determined for the naphthalene radical cation (3.20 ± 0.13 eV and −19 ± 11 J K^{-1} mol^{-1} for E_0 and $\Delta^{\ddagger}S$, respectively).[36] Our previous work, which looked at 1,2-dihydronaphthalene and 9,10-dihydrophenanthrene radical cations, showed that when deviations from the unadulterated PAHs brings about structural changes that affect the C-H bond dissociation energies.[38]

The highest energy dissociation reaction observed using iPEPICO was R3, the acetylene loss channel. This is the channel which possessed the greatest difficulty in determining the kinetic values due to the uncertainty in the reaction symmetry. As a result, two models were fit, corresponding to the formation of structures **4** and **5** (the two proposed fits are shown in Figure 2). While R3 for each possibility has very different reaction symmetry, 6 versus 1, there is no notable difference in the quality of the fitting results. The curves are indistinguishable below16.5 eV, as are their asymmetric TOF fits for the $C_{12}H_8^{+\cdot}$ peak. The derived activation energies for the two models are essentially identical (4.19 ± 0.3 eV to form structure **4**, compared to 4.21 ± 0.3 eV to form **5**). There is a minor

difference suggested when the entropies of activation are compared, 7 ± 10 J K^{-1} mol^{-1} for structure **5** and 22 ± 10 J K^{-1} mol^{-1} for structure **4**. Ling et al. used the biphenylene structure for their calculations and obtained a $\Delta^{\ddagger}S$ value of 53.6 ± 4 J K^{-1} mol^{-1}, which is significantly higher than our results for biphenylene.[1] The discrepancy continues when the activation energies are compared as the value obtained by Ling (4.50 ± 0.1 eV) is again substantial higher than either value obtained here. There is a well-known interplay between E_0 and $\Delta^{\ddagger}S$ in fitting experimental data, and the added constraint of fitting the asymmetric TOF peaks in our data further constrains the possible values for these two parameters, adding confidence to our results.

C_2H_2 loss from ionized naphthalene to form ionized benzocyclobutadiene was found to have E_0 and $\Delta^{\ddagger}S$ values of 4.12 ± 0.05 eV and 0 ± 2 J K^{-1} mol^{-1},[36] respectively, which agree better with the present results forming ion **5** (especially the entropy). A tighter transition state is also more consistent with a large reverse energy barrier as suggested by the shape of the metastable fragment ion peak in the MIKES experiment. All of this suggests that the final product from the loss of C_2H_2 from ionized anthracene is actually the cyclobuta[b]naphthalene ion (**5**).

6.2.3 APCI-CID Mass Spectrometry

Collision-induced dissociation (CID) experiments were conducted over a center-of-mass collision energy range of 2.5-9.0 eV. In addition to reactions R1 and R3, loss of the larger C_4H_2 moiety was also observed:

$$C_{14}H_{10}^{+\cdot} \rightarrow C_{10}H_8^{+\cdot} + C_4H_2 \qquad \text{(R4)}$$

For this study we limited the analysis to the primary reactions from the molecular ion and did not explore the sequential reaction, R2. The intensity of the peak due to $[M-2H]^{+\cdot}$ was simply added into the $[M-H]^{+}$ intensity. The breakdown curves generated for reactions R1, R3 and R4 are shown in Figure 34, with the extracted E_0 and $\Delta^{\ddagger}S$ summarized in Table 6 and Table 7 respectively. Looking at Figure 34, it can be seen that the CID experiments produced well defined breakdown curves which made fitting the data possible with a fair degree of confidence. The alpha value determined was 400 KeV, which allows for the determination of the effective temperature of the post-collision ions at each centre-of-mass collision energy.

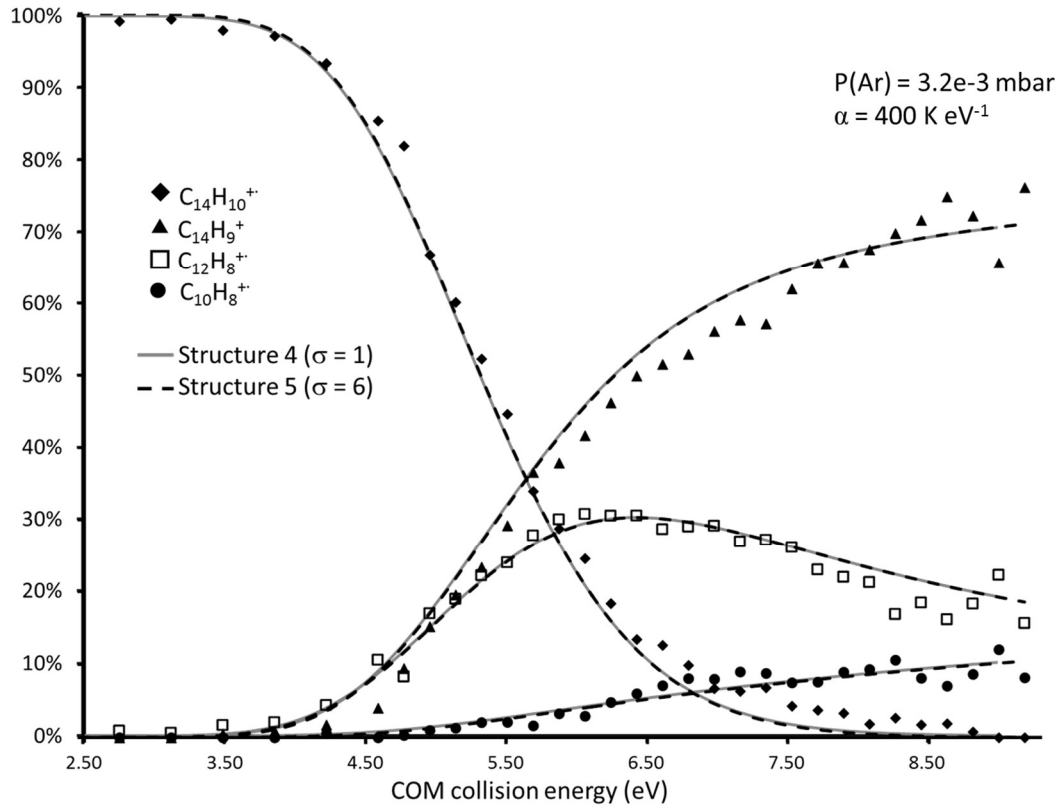

Figure 34: APCI/CID breakdown diagram and fitting illustrating the effect of using structure 4 (black broken line) versus structure 5 (solid grey line) for the calculation of $C_{12}H_8^{+\bullet}$. Pressure and corresponding alpha value are also given.

Reaction R1 gave E_0 and $\Delta^{\ddagger}S$ values of 4.55 ± 0.10 eV and 13 ± 4 J K^{-1} mol^{-1}, respectively. These values are within the uncertainty of the iPEPICO data reported herein. When the results are compared to literature, it can be seen that the activation energy determined by Ling is equally close to the CID results as to the iPEPICO ones. The $\Delta^{\ddagger}S$ values deviate more when compared to literature but they are still in keeping with iPEPICO results. Reaction R4 can only be compared to literature results as there was insufficient ion intensity for this channel to produce a fit in the iPEPICO experiment. The activation energy was determined to be 4.87 ± 0.30 eV which is in good agreement with the value determined by Ling of 4.46 ± 0.1 eV.[1] There is again a larger difference when comparing $\Delta^{\ddagger}S$, CID results yielded a value of 23 ± 10 J K^{-1} mol^{-1} compared to 8.4 ± 4 J K^{-1} mol^{-1}.[1] Nevertheless, both results indicate that the transition state is loose, which helped us assign the product structure as the naphthalene radical cation (**8**). The anthracene dissociative photoionization activation energies can be compared to those for ionized naphthalene. In $C_{10}H_8^+$, C_4H_2 loss required only 0.15 eV more energy than C_2H_2 loss, while in this case it requires an extra 0.69 eV. The difference between these values, 0.54 eV, is likely due to a larger barrier for H-transfer due to the more delocalized charge in anthracene.

The last reaction to consider is R2. Once again, due to the ambiguity of the results from the iPEPICO fit, two different models are proposed corresponding to structures (**4**) and (**5**). Looking at structure (**5**), which was not discussed by Ling, it can be seen that the activation energy is very close to that determined for the same model for the iPEPICO results (4.18 ± 0.10 eV versus 4.21 ± 0.30 eV). The $\Delta^{\ddagger}S$ values are also similar (-1 ± 3 J K^{-1} mol^{-1} for the CID fit and 7 ± 10 J $K^{-1}mol^{-1}$ from iPEPICO). Considering structure (**4**), the values obtained were E_0 4.17 ± 0.06 eV and $\Delta^{\ddagger}S$ of 12 ± 3 $JK^{-1}mol^{-1}$. The difference in the

activation energy is negligible, which was also observed when the two models were compared for the iPEPICO results. Since all four models were able to give very good fits for the two sets of experimental data, there is some confidence in this value. $\Delta^{\ddagger}S$ also shows a similar trend in that, when switching from a reaction degeneracy value of 6 to 1 (switching between structure **5** to **4**) the value for $\Delta^{\ddagger}S$ increases. Both systems saw an increase of ~14 J K^{-1} mol^{-1}, which still falls short of the value determined by Ling *et al.* (53.6 ± 4 J K^{-1} mol^{-1}).[1]

Admittedly, our feeling at the start of study was that the assignment of an effective temperature to the post-collision ions would not result in adequate fits to the experimental data. However, surprisingly, this turned out not to be the case. Our previous work has been focussed on the relative energetics and entropics for dissociating systems involving non-covalent interactions, and this is the first time the simple model described above has been validated against reliable iPEPICO data. It appears that whatever the post-collision internal energy distribution is in these experiments, the shape of the resulting distribution function at least appears similar to a Boltzmann distribution.

6.3 Conclusion

The dissociation of the anthracene radical cation has been investigated using two different techniques, imaging photoelectron photoion coincidence spectrometry and atmospheric pressure chemical ionization – collision induced dissociation mass spectrometry. The combination of these methods has allowed for a detailed picture of the fragmentation channels. The results from the iPEPICO fitting for reactions R1-3 are: E_0 (in eV) values of 4.28 ± 0.30 (R1), 2.71 ± 0.20 (R2) and 4.20 ± 0.30 (average of R3) while the $\Delta^{\ddagger}S$ values (in J K^{-1} mol^{-1}) of 12 ± 15 (R1), 0 ± 15 (R2) and either 7 ± 10 (using structure **5** for R3) or 22 ± 10 (using structure **4** for R3). The results for the APCI-CID

results are similar; the E_0 (in eV) values are 4.55 ± 0.10 (R1), 4.87 ± 0.30 (R4) and 4.18 ± 0.30 (average of R3) while the $\Delta^{\ddagger}S$ values (in J K^{-1} mol^{-1}) are 13 ± 2 (R1), 23 ± 8 (R4) and either -1 ± 6 (using structure **5** for R3) or 12 ± 3 (using structure **4** for R3). In both cases, using either **4** or **5** gave excellent breakdown diagrams fits but the $\Delta^{\ddagger}S$ values for forming **5** are more consistent with a large reverse energy barrier as suggested by the shape of the metastable fragment ion peak in the MIKES experiment. All of this suggests that the final product from the loss of C_2H_2 from ionized anthracene is actually the cyclobuta[b]naphthalene ion (**5**).

One of the goals of this study was to determine if the APCI-CID method would be reliable to continue the dissociation study of larger PAHs. In the two reactions R1 and R3, observed by both techniques, the results were internally consistent between the two methods. Since the APCI-CID method has fewer size restrictions for the molecules it can study, it may be a viable alternative for larger and less volatile systems. Further experiments are underway in which the CID-based model will be tested against iPEPICO data to explore the post-collision internal energy distribution more fully.

6.4 References for Chapter 6

1. Ling, Y.; Lifshitz, C., Time-Dependent Mass Spectra and Breakdown Graphs. 21. C14H10 Isomers. *J. Phys. Chem. A* **1998,** *102*, 708-716.
2. Ling, Y.; Martin, J. M. L.; Lifshitz, C., Energetics of Acetylene Loss from C14H10+ Cations: A Density Functional Calculation. *J. Phys. Chem. A* **1997,** *101*, 219-226.
3. Johansson, H. A. B.; Zettergren, H.; Holm, A. I. S.; Haag, N.; Nielsen, S. B.; Wyer, J. A.; Kirketerp, M.-B. S.; Støchkel, K.; Hvelplund, P.; Schmidt, H. T.*, et al.*, Unimolecular Dissociation of Anthracene and Acridine Cations: The Importance of Isomerization Barriers for the C2H2 Loss and HCN Loss Channels. *J. Chem. Phys.* **2011,** *135*, 1-8.

4. Zhen, J.; Paardekooper, D. M.; Candian, A.; Linnartz, H.; Tielens, A. G. G. M., Quadrupole Ion Trap/Time-of-Flight Photo-Fragmentation Spectrometry of the Hexa-Peri-Hexabenzocoronene (Hbc) Cation. *Chem. Phys. Lett.* **2014,** *592*, 211-216.

5. Comeau, A. N.; Renaud, J. B.; Mironov, G. G.; Berezovski, M. V.; Mayer, P. M., Investigating the Relationship between the Gas-Phase Conformations and Dissociation Energetics of Peptide–Saccharide Complexes. *Int. J. Mass spectrom.* **2012,** *316–318*, 31-39.

6. Mayer, P. M.; Martineau, E., Gas-Phase Binding Energies for Non-Covalent a[Small Beta]-40 Peptide/Small Molecule Complexes from CID Mass Spectrometry and RRKM Theory. *PCCP* **2011,** *13*, 5178-5186.

7. Renaud, J. B.; Martineau, E.; Mironov, G. G.; Berezovski, M. V.; Mayer, P. M., The Collaborative Role of Molecular Conformation and Energetics in the Binding of Gas-Phase Non-Covalent Polymer/Amine Complexes. *PCCP* **2012,** *14*, 165-172.

8. Renaud, J. B.; Overton, S.; Mayer, P. M., Energy and Entropy at Play in Competitive Dissociations: The Case of Uneven Positional Dissociation of Ionized Triacylglycerides. *Int. J. Mass spectrom.* **2013,** *352*, 77-86.

9. Mayer, P. M.; Poon, C., The Mechanisms of Collisional Activation of Ions in Mass Spectrometry. *Mass Spec. Rev.* **2009,** *28*, 608-639.

10. Asano, K. G.; Goeringer, D. E.; Butcher, D. J.; McLuckey, S. A., Bath Gas Temperature and the Appearance of Ion Trap Tandem Mass Spectra of High-Mass Ions. *Int. J. Mass spectrom.* **1999,** *190/191*, 281-293.

11. Asano, K.; Goeringer, D.; McLuckey, S., Dissociation Kinetics in the Quadrupole Ion Trap. *Proceeding of the 46th Conference for the American Society for Mass Spectrometry* **1998**.

12. Goeringer, D. E.; McLuckey, S. A., Evolution of Ion Internal Energy During Collisional Excitation in the Paul Ion Trap: A Stochastic Approach. *J. Chem. Phys.* **1996,** *104*, 2214-2221.

13. Hart, K. J.; McLuckey, S. A., Relative Dissociation Energy Measurements Using Ion Trap Collisional Activation. *J. Am. Soc. Mass Spectrom.* **1994,** *5*, 250-259.

14. Asano, K. G.; Butcher, D. J.; Goeringer, D. E.; McLuckey, S. A., Effective Ion Internal Temperatures Achieved Via Boundary Activation in the Quadrupole Ion Trap: Protonated Leucine Enkephalin. *J. Mass Spectrom.* **1999,** *34*, 691-698.

15. Goeringer, D. E.; Asano, K. G.; McLuckey, S. A., Ion Internal Temperature and Ion Trap Collisional Activation: Protonated Leucine Enkephalin. *Int. J. Mass spectrom.* **1999,** *182/183*, 275-288.

16. Goeringer, D. E.; Duckworth, D. C.; McLuckey, S. A., Collision-Induced Dissociation in Quadrupole Ion Traps: Application of a Thermal Model to Diatomic Ions. *J. Phys. Chem. A* **2001,** *105*, 1882-1889.

17. Goeringer, D. E.; McLuckey, S. A., Kinetics of Collision-Induced Dissociation in the Paul Trap: A First-Order Model. *Rapid Commun. Mass Spectrom.* **1996,** *10*, 328-334.

18. Laskin, J.; Futrell, J. H., Collisional Activation of Peptide Ions in FT-ICR Mass Spectrometry. *Mass Spec. Rev.* **2003,** *22*, 158– 181.

19. Laskin, J.; Futrell, J. H., Activation of Large Ions in FT-ICR Mass Spectrometry. *Mass Spec. Rev.* **2005,** *24*, 135– 167.

20. Laskin, J.; Byrd, M.; Futrell, J., Internal Energy Distributions Resulting from Sustained Off-Resonance Excitation in FTMS. I. Fragmentation of the Bromobenzene Radical Cation. *Int. J. Mass spectrom.* **2000,** *195/196*, 285-302.

21. Laskin, J.; Denisov, E.; Futrell, J., A Comparative Study of Collision-Induced and Surface-Induced Dissociation. 1. Fragmentation of Protonated Dialanine. *J. Am. Chem. Soc.* **2000,** *122*, 9703-9714.

22. Laskin, J.; Denisov, E.; Futrell, J., Fragmentation Energetics of Small Peptides from Multiple-Collision Activation and Surface-Induced Dissociation in FT-ICR MS. *Int. J. Mass spectrom.* **2002,** *219*, 189-201.

23. Nesatyy, V. J.; Laskin, J., Dissociation of Noncovalent Protein Complexes by Triple Quadrupole Tandem Mass Spectrometry: Comparison of Monte Carlo Simulation and Experiment. *Int. J. Mass spectrom.* **2003,** *221*, 245-262.

24. Laskin, J.; Futrell, J., Internal Energy Distributions Resulting from Sustained Off-Resonance Excitation in Fourier Transform Ion Cyclotron Resonance Mass Spectrometry. Ii. Fragmentation of the 1-Bromonaphthalene Radical Cation. *J. Phys. Chem. A* **2000,** *104*, 5484-5494.

25. Bastian, M. J.; Dressler, R. A.; Levandier, D. J.; Murad, E.; Muntean, F.; Armentrout, P. B., Low Energy CID and PD Studies of the (N2O,H2O)+ Cluster Ion. *J. Chem. Phys.* **1997,** *106*, 9570-9579.

26. Muntean, F.; Armentrout, P. B., Guided Ion Beam Study of Collision-Induced Dissociation Dynamics: Integral and Differential Cross Sections. *J. Chem. Phys.* **2001,** *115*, 1213-1228.

27. Ervin, K. M.; Armentrout, P. B., Translational Energy Dependence of $Ar^+ + XY \rightarrow Arx^+ + Y$ ($XY=H_2,D_2,HD$) from Thermal to 30 eV C.M. *J. Chem. Phys.* **1985,** *83*, 166-189.

28. Kenttamaa, H. I.; Cooks, R. G., Internal Energy Distributions Acquired through Collisional Activation at Low and High Energies. *Int. J. Mass Spectrom. Ion Processes* **1985,** *64*, 79-83.

29. Emilio Martínez-Núñez; Fernández-Ramos, A.; Vázqueza, S. A.; Marques, J. M. C.; Xue, M.; Hase, W. L., Quasiclassical Dynamics Simulation of the Collision-Induced Dissociation of $Cr(CO)_6^+$ with Xe. *J. Chem. Phys.* **2005,** *123*, 154311.

30. Douglas, D. J., Applications of Collision Dynamics in Quadrupole Mass Spectrometry *J. Am. Soc. Mass Spectrom.* **1998,** *9*, 101-113

31. Wysocki, V. H.; Kenttamaa, H. I.; Cooks, R. G., Internal Energy Distributions of Isolated Ions after Activation by Various Methods. *Int. J. Mass Spectrom. Ion Processes* **1987,** *75*, 181-208.

32. Knyazev, V. D.; Stein, S. E., Monte Carlo/RRKM/Classical Trajectories Modeling of Collisional Excitation and Dissociation of N-Butylbenzene Ion in Multipole Collision Cells of Tandem Mass Spectrometers. *J. Phys. Chem. A* **2010,** *114*, 6384-6393.

33. Knyazev, V. D.; Stein, S. E., Classical Trajectories and Rrkm Modeling of Collisional Excitation and Dissociation of Benzylammonium and Tert-Butyl Benzylammonium Ions in a Quadrupole-Hexapole-Quadrupole Tandem Mass Spectrometer. *J. Am. Soc. Mass. Spectrom.* **2010,** *21*, 425-439.

34. Mennella, V.; Hornekær, L.; Thrower, J.; Accolla, M., The Catalytic Role of Coronene for Molecular Hydrogen Formation. *ApJL* **2012,** *745*, L2.

35. Mayer, P. M.; Blanchet, V.; Joblin, C., Threshold Photoelectron Study of Naphthalene, Anthracene, Pyrene, 1,2-Dihydronaphthalene, and 9,10-Dihydroanthracene. *J. Chem. Phys.* **2011,** *134*, 244312.

36. West, B.; Joblin, C.; Blanchet, V.; Bodi, A.; Sztáray, B.; Mayer, P. M., On the Dissociation of the Naphthalene Radical Cation: New iPEPICO and Tandem Mass Spectrometry Results. *J. Phys. Chem. A* **2012,** *116*, 10999-11007.

37. Fujiwara, K.; Harada, A.; Aihara, J.-i., CH Bond Dissociation Energies of Polycyclic Aromatic Hydrocarbon Molecular Cations: Theoretical Interpretation of the (M-1)+ Peak in the Mass Spectra. *J. Mass Spectrom.* **1996,** *31*, 1216-1220.

38. West, B.; Joblin, C.; Blanchet, V.; Bodi, A.; Sztáray, B.; Mayer, P., The Dynamics of Hydrogen and Methyl Radical Loss from Ionized Dihydro-Polycyclic Aromatic Hydrocarbons: A Tandem Mass Spectrometry and Imaging-PEPICO Study of Dihydronaphthalene and Dihydrophenanthrene. *J. Phys. Chem. A* **2014,** *118*, 1807-1816.

7 PAH fragments

7.1 Introduction

Two sets of isomers were originally chosen for this study, in which each isomeric pair contains one closed-ring ion and one with a carbon chain. Benzocyclobutadiene (closed-ring) and ethynylbenzene (open) $C_8H_6^{+\cdot}$ ions are possible fragment candidates resulting from the loss of C_2H_2 from the naphthalene cation. There has been some dispute as to which is formed in the dissociative photoionization of naphthalene, and whichever it is, it may well be an abundant molecular ion in ISM. While it was possible to obtain ethynylbenzene commercially, benzocyclobutene was selected as a potential precursor to benzocyclobutadiene, an inherently unstable molecule.[1] The second set of isomer samples was chosen to map out the photoionization dynamics of the $C_9H_7^{+\cdot}$ structure: indene and 1-propynlbenzene. As will be shown in the following sections, the original intent was not possible due to the energy requirements to form the benzocyclobutadiene ion, therefore the four molecules to be compared will be the ones listed in Figure 34: 1-ethynylbenzene, benzocyclobutene, 1-propynylbenzene and indene.

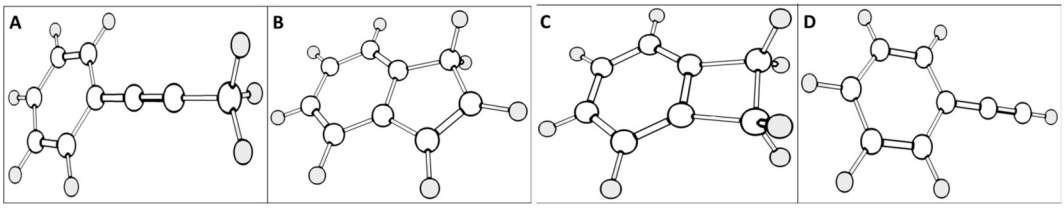

Figure 35: 3D representation of the radical cations used in this work as calculated using B3LYP 6-311G+(d,p) ; A) 1-propynylbenzene, B) indene, C) benzocyclobutene and D) 1-ethynylbenzene.

In this chapter we investigate the threshold photoelectron spectra and unimolecular dissociation of the four molecules mentioned above by imaging photoelectron-photoion coincidence (iPEPICO) spectroscopy. In these experiments, conducted on the VUV beamline at the Swiss Light Source (SLS), internal energy selected parent ions were prepared with 2 meV energy resolution and we measured the threshold photoelectron spectra as well as the fragmentation channels and the corresponding unimolecular dissociation rates in the 10^3-10^7 s^{-1} range. By modeling the fractional parent and daughter ion abundances plotted as a function of the photon energy in the breakdown diagram simultaneously with the measured dissociation rates curves, it is possible to determine the dissociation thresholds for each of the fragment ions. As in our previous studies, the breakdown curves and their asymmetric time-of-flight profiles were fit, which allowed for the kinetic modeling of the dissociative ionization processes, and yielded accurate barriers heights and entropies of activation for each of the channels.

7.2 Results and Discussion

7.2.1 Threshold Photoelectron Spectra

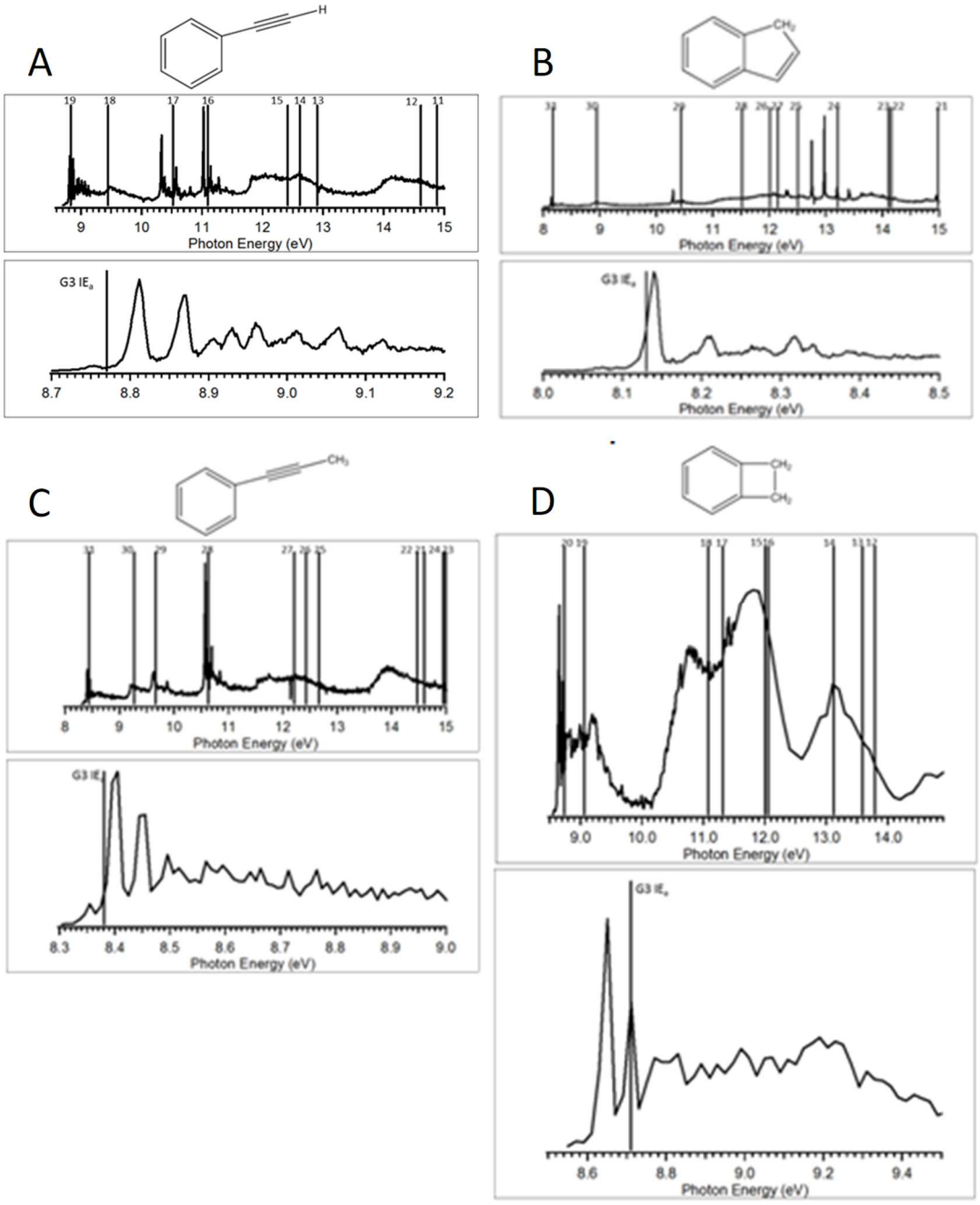

Figure 36: Threshold photoelectron spectra with molecular orbital vertical ionization energies from the OVGF calculations shown as dark vertical lines and the G3 calculated adiabatic IE is shown as a grey vertical line for: (A) ethynylbenzene, (B) indene, (C) propynylbenzene and (D) benzocyclobutene.

The threshold photoelectron spectra (TPES) for the four molecules (Figure 35) are found in Figure 36. In each figure the total TPES from threshold to 15 eV photon energy is shown, along with the vertical molecular orbital ionization energies from the OVGF calculations. Note that the MO numbering is taken from the base Hartree-Fock calculations and refer to the outer-valence orbitals only. Perturbation treatment sometimes re-orders the MOs. In each figure are also presented expansions of regions of the TPES that contain vibrational structure. The threshold region expansion also displays the G3 calculated adiabatic ionization energy (IE_a). The MOs assigned to the experimental spectra are listed in Table 8 Table 11.

Table 8: Comparison of experimental and OVGF/cc-pVQZ molecular orbital vertical ionization energies for 1-ethynylbenzene (C_{2v} symmetry).

MO	Sym	TPES	OVGF	Pole Strength
11	A1	14.1-14.7	14.878	0.871
12	B2		14.608	0.874
13	B1	11.80-	12.898	0.804
14	A1	12.6	12.609	0.888
15	B2		12.414	0.892
16	B1	11.02	11.092	0.87
17	B2	10.32	10.514	0.887
18	A2	9.48	9.446	0.887
19	B1	8.82	8.828 (8.77)[a]	0.891

[a] G3 level calculation

Table 9: Comparison of experimental and OVGF/cc-pVQZ molecular orbital vertical ionization energies for benzocyclobutene (C_{2v} symmetry).

MO	Sym	TPES	OVGF	Pole Strength
12	B2	13.4-14.1	13.786	0.878
13	A1		13.582	0.881
14	A2	13.10	13.115	0.900
15	B1	11.38-12.0	11.995	0.817
16	A1		12.053	0.896
17	B2	10.60-	11.312	0.895
18	A1	11.00	11.08	0.899
19	A2	9.19	9.06	0.891
20	B1	8.65	8.734 (8.70)[a]	0.893

[a] G3 level calculation

Table 10: Comparison of experimental and OVGF/cc-pVQZ molecular orbital vertical ionization energies for 1-propynylbenzene (C_S symmetry).

MO	Sym	TPES	OVGF	Pole Strength
21	A'	13.8-14.5	14.600	0.872
22	A'		14.465	0.874
23	A"		14.993	0.889
24	A'		14.943	0.892
25	A"	11.54-	12.656	0.802
26	A'	12.60	12.427	0.886
27	A'		12.208	0.891
28	A"	10.57	10.623	0.873
29	A'	9.62	9.657	0.888
30	A"	9.23	9.267	0.885
31	A"	8.40	8.440 (8.38)[a]	0.89

[a] G3 level calculation

Table 11: Comparison of experimental and OVGF/cc-pVQZ molecular orbital vertical ionization energies for indene (C_S symmetry).

MO	Sym	TPES	OVGF	Pole Strength
21	A'	14.95	14.982	0.841
22	A'	13.5-14.5{	14.147	0.875
23	A'		14.102	0.871
24	A'	12.75	13.199	0.886
25	A'	12.53	12.503	0.887
26	A'	12.07	12.002	0.889
27	A"	12.29	12.142	0.814
28	A'	11.3	11.517	0.896
29	A"	10.29	10.435	0.876
30	A"	8.93	8.942	0.888
31	A"	8.14	8.167 (8.13)[a]	0.892

[a] G3 level calculation

Predictably, as the ionization energy increases, agreement between the OVGF calculations and the experimental spectra becomes weaker, due to the breakdown of the assumptions in the Green's function approximation.

The experimentally determined IE for ethynylbenzene is 8.78 ± 0.02 eV. There is good agreement between this and the G3-level calculated value of 8.77 eV and various values from the literature ranging from 8.75 eV[2] to an electron ionization value of 8.9 eV[3], with the most recent photoelectron results being 8.82 eV[4-6]. Both the ground state of the ion and second and third excited states show vibrational structure indicative of good Franck-Condon overlap between the neutral and ion states.

The experimentally determined IE for benzocyclobutene is 8.61 ± 0.02 eV. The value is significantly lower than the G3-level calculated value of 8.70 eV. Literature values range from 8.74 eV for the electron ionization threshold to vertical IE values of 8.66 from photoelectron spectroscopy, which are in better agreement with the present vertical IE of 8.62 eV.[7-8]

The experimentally determined IE for propylbenzene is 8.38 ± 0.02 eV. There is excellent agreement between this and the G3-level calculated value, which is also 8.38 eV. Both are slightly lower than previous photoelectron results of 8.41 – 8.49 eV[5, 9-10]. Both the ground state and third excited state (ionization of MO 28) display vibrational structure.

The experimentally determined IE for indene is 8.12 ± 0.02 eV. There is excellent agreement between this and the G3-level calculated value, 8.13 eV. Previous photoelectron results are all around these values, 8.13 – 8.15 eV[11-13]. Both the ground state of the ion and second excited state show vibrational structure.

7.2.2 Dissociative Photoionization

Overall, there are five reaction channels observed for the four molecules being presented in this work:

$$C_9H_8^{+\cdot}\ (\text{1-propynylbezene}) \rightarrow C_9H_7^{+} + H \qquad \text{(R1)}$$

$$C_9H_8^{+\cdot}\ (\text{indene}) \rightarrow C_9H_7^{+} + H \qquad \text{(R2)}$$

$$C_8H_8^{+\cdot}\ (\text{benzocyclobutene}) \rightarrow C_8H_7^{+} + H \qquad \text{(R3)}$$

$$C_8H_8^{+\cdot}\ (\text{benzocyclobutene}) \rightarrow C_6H_6^{+} + C_2H_2 \qquad \text{(R4)}$$

$$C_8H_6^{+\cdot}\ (\text{1-ethynylbenzene}) \rightarrow C_6H_4^{+} + C_2H_2 \qquad \text{(R5)}$$

The proposed fragment ion structures for each reaction are presented in Figure 37.

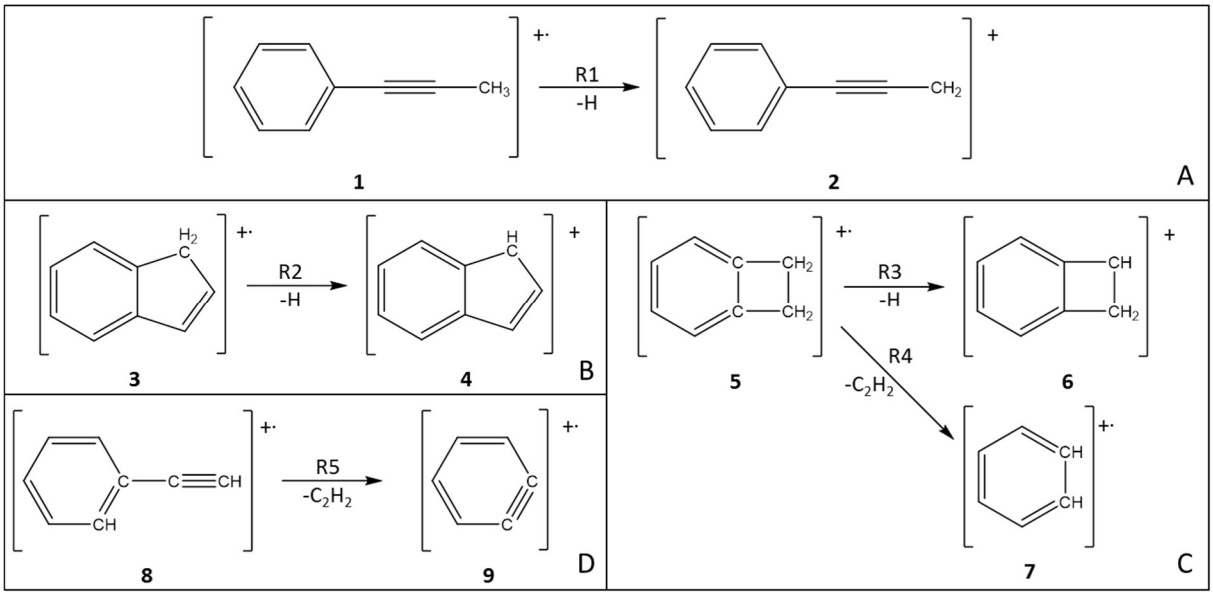

Figure 37: Reaction schemes for R1-5 for the four starting molecules; A) 1-propynylbenzene, B) indene, C) benzocyclobutene and D) 1-ethynylbenzene.

Each pair of similar molecules will be discussed together in order to compare their fragmentation reactions, because, to date, no literature data has been found.

7.2.3 1-Propynylbenzene (1) vs. Indene (3)

Both of these ions dissociate by H loss (R1 and R2). Since hydrogen atoms attached to sp^3 carbons have lower bond dissociation energies than those attached to sp^2 sites,[14] the product ion from reaction R1 was assigned to structure **2** whereas the product for R2 was assigned to the indenyl structure (**4**).

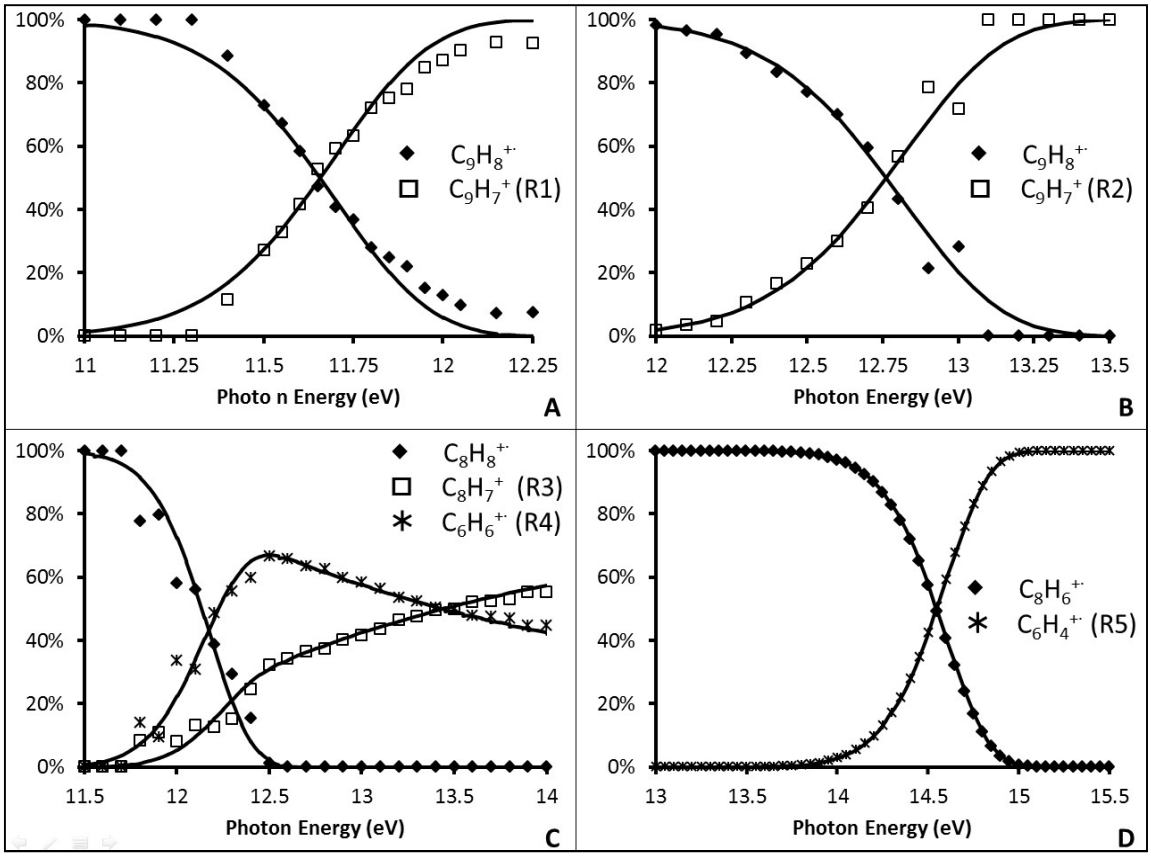

Figure 38: Experimental iPEPICO breakdown curves for the four molecules studied, A) 1-propynylbenzene, B) indene, C) benzocyclobutene, and D) 1-ethynylbenzene, all at ion draw-out potentials of 120 V/cm.

Figure 38a shows the fitted breakdown curve for R1, the removal of a hydrogen atom from the methyl group. From an enthalpic perspective this is a fairly facile reaction and thus the low dissociation energy (1.86 ± 0.17 eV) is quite reasonable. Typically, for a dehydrogenation reaction, one would expect a loose transition state, and a positive $\Delta^{\ddagger}S_{1000K}$ value. However, in this case, the negative value obtained (-30 ± 31 J K^{-1} mol^{-1}) can be explained by the loss of rotational degrees of freedom of the methyl group in going from **1** to **2**, as there may be a reverse barrier on the way to planarity.

From indene, the H loss is also the removal from the sp3 carbon but in this case there is little change in the rigidity of the structure as it is already quite restricted. Figure 38b shows the breakdown diagram for R2. The $\Delta^{\ddagger}S_{1000K}$ value was determined to be -2 ± 38 J K^{-1} mol^{-1} due to the lack of re-organization of the ring upon H loss. The E_0 value of 2.56 ± 0.37 eV is 0.7 eV higher in energy than that of R1 which indicates that the presence of the second ring has a stabilizing effect on the C-H bonds. As there have been no literature values found for comparison, the E_0 values were compared to the G3 calculations. The calculated values are shown alongside the fitted values in Table 12. For R1, there is some discrepancy between the calculated energy difference and those determined from RRKM (2.57 eV versus 1.86 eV). The agreement between the values for R2 is much better; with the E_0(G3) value falling well within the error associated with the fitted E_0 value (2.78 eV compared to 2.56 ± 0.37 eV).

7.2.4 Benzocyclobutene (5) vs. 1-ethynylbenzene (8)

Unlike the previous molecules, benzocyclobutene (**5**) undergoes two dissociation channels, dehydrogenation (R3) and the loss of C_2H_2 (R4). The iPEPICO experiments were conducted from 11.5 – 15 eV in energy, which is very similar to the range used for indene. R3, like the other dehydrogenation processes, was assigned structure (**6**) as there were only the two identical sp^3 carbon sites. The assignment of R4 leading to benzene cation was made as it is the energetically most favorably $C_6H_6^{+\cdot}$ ion.

1-ethynylbenzene (**8**) is the only molecule investigated which did not undergo hydrogen atom loss. This is evident based on its molecular structure (Figure 35), because there are no readily available hydrogen atoms; the majority of the hydrogen atoms are on the benzene ring and the only other hydrogen atom is attached to a sp carbon site which would

have an even higher bond dissociation energy.[14] Similar to benzocyclobutene, it did lose C_2H_2 (R5), which yielded the proposed structure **9** since the cleavage of the side chain (after a hydrogen migration) would result in the benzynyl cation.

Figure 38c shows the breakdown diagram for benzocyclobutene. For R3, the E_0 and $\Delta^{\ddagger}S_{1000K}$ values were 2.23 ± 0.10 eV and -11 ± 8 J K^{-1} mol^{-1} respectively. These values are notably similar to those obtained for R2, which gives credence to the observation that the fused bicyclic structure has an effect on the dehydrogenation. The competing channel, R4, which dominates at most energies studied, gave energetic results of E_0 equal to 2.00 ± 0.10 eV and a $\Delta^{\ddagger}S_{1000K}$ value of -17 ± 9 J K^{-1} mol^{-1}. In both reactions for benzocyclobutene, their entropies of activation are comparable. The enthalpy value is slightly lower for R4 compared to R3. This can be explained by the influence of ring strain on the reactivity of the molecule,[15] as it will be seen that when compared to R5, the energy required for R4 is significantly lower than the cleavage from 1-ethynylbenzene.

As indicated above, the energy requirements for R5 are substantially higher than for R4. Figure 38d shows the breakdown curve for 1-ethynylbenzene. The RRKM fitting gave the values of 3.94 ± 0.43 eV for E_0 and 42 ± 36 J K^{-1} mol^{-1} for $\Delta^{\ddagger}S_{1000K}$; which makes R5 approximately 2 eV higher in energy than its close equivalent R4. It should be noted that this is the reverse trend observed for H loss, where the open isomer had the lower entropy of activation. The entropy value for this channel is the only one which is always positive, even at the furthest extent of the error, which could suggest the involvement of an intermediate ion-molecule complex between the benzynyl cation and acetylene.

Unlike the previous molecules, both benzocyclobutene and 1-ethynylbenzene do produce asymmetric TOF peaks for the lower end of their respective energy ranges. This gives another parameter to improve the accuracy of the RRKM fitting. Figure 39a-b shows two representative fits for each $[M\text{-}C_2H_2]^{+\cdot}$ TOF peak, one before and after the Gaussian shape has been achieved.

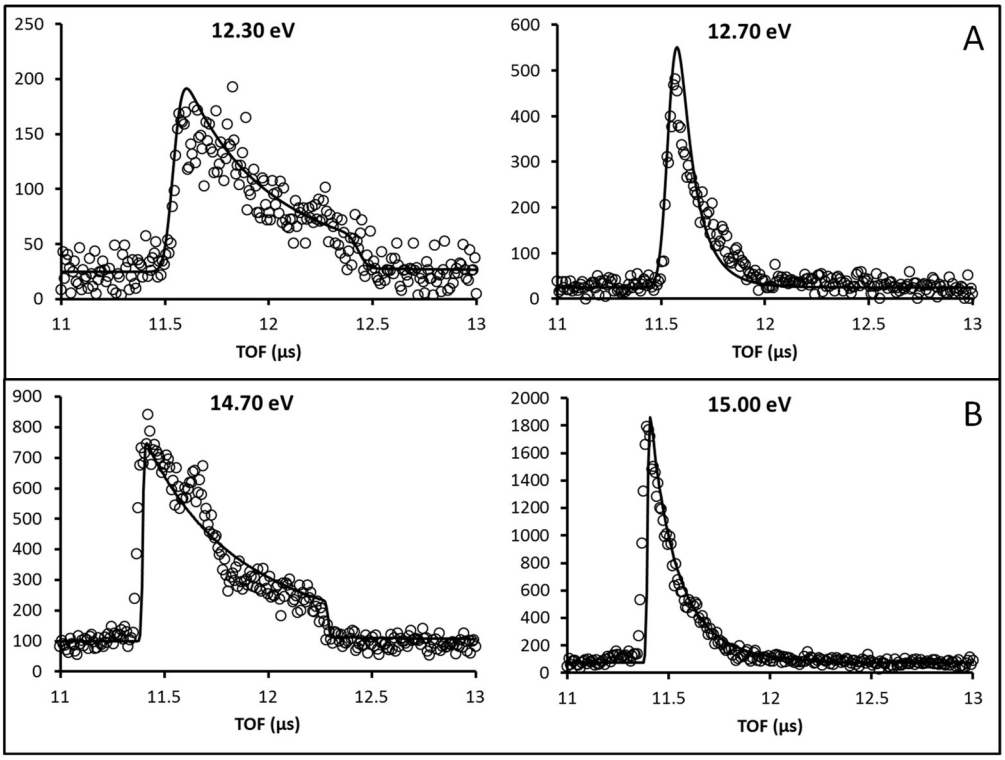

Figure 39: Representative TOF fittings for the asymmetric $[M\text{-}C_2H_2]+\bullet$ peak for; A) benzocyclobutene and B) 1-ethynylbenzene.

The E_0 values were again compared to those calculated at the G3 level of theory (Table 12). The result for R3 shows good agreement (2.33 eV versus 2.23 ± 0.10 eV for calculated and fitted, respectively) while the comparison for R4 (1.70 eV calculated compared to 2.00 ± 0.10 eV) certainly indicates that what was measured was the height of the reverse energy barrier in the reaction, in which two H atoms must be back-transferred to

the benzene ring prior to C_2H_2 loss. The last reaction, R5 for 1-ethynylbenzene had the largest calculated energy (4.54 eV compared to 3.94 ± 0.43 eV). We note that for these systems, it is unclear as to the reliability of the G3 calculations, as values for the reaction energies range widely with level of theory (Table 12).

Table 12: Comparison between various calculated ΔE values and fitted RRKM E_0 and $\Delta^{\ddagger}S_{1000K}$.

		Calculated (eV)				RRKM fitting	
		E_0(G3)	E_0(MP2)	E_0(B3LYP)	E_0(QCISD(T))	E_0 (eV)	$\Delta^{\ddagger}S_{1000K}$ (J K-1 mol-1)
(R1)	$C_9H_8^{+\cdot} \rightarrow C_9H_7^{+} + H$	2.57	1.82	2.69	2.31	1.98 ± 0.27	-21 ± 31
(R2)	$C_9H_8^{+\cdot} \rightarrow C_9H_7^{+} + H$	2.78	1.97	2.95	2.51	2.47 ± 0.41	-17 ± 43
(R3)	$C_8H_8^{+\cdot} \rightarrow$ C8H7+ +H	2.33	1.64	2.47	2.08	2.25 ± 0.20	-13 ± 29
(R4)	$C_8H_8^{+\cdot} \rightarrow C_6H_6^{+\cdot} + C_2H_2$	1.70	1.88	1.56	1.81	2.06 ± 0.26	-16 ± 33
(R5)	$C_8H_6^{+\cdot} \rightarrow C_6H_4^{+\cdot} + C_2H_2$	4.54	4.41	4.68	4.58	4.03 ± 0.42	42 ± 36

7.3 Conclusion

The photoelectron spectra of the four target molecules in this study were obtained from iPEPICO data. In general, the measured ground state IEs were in good agreement with the IEs determined using G3-level calculations. The observed dissociation of each ion was modeled with RRKM theory and the resulting activation energies and entropies provide information on the barriers likely to be present in isomerisation reactions prior to fragmentation.

7.4 References for Chapter 7

1. Cava, M. P.; Mitchell, M. J., *Cyclobutadiene and Related Compounds*. Academic Press: New York, 1967; Vol. 10, p 503.

2. NIST, *Nist Computational Chemistry Comparison and Benchmark Database, Nist Standard Reference Database Number 101* National Institute of Standards and Technology: Gaithersburg MD, 2006; Vol. http://srdata.nist.gov/cccbdb

3. Renaud, J.; Mayer, P., The Applicability of the Kinetic Method for Measuring Relative Affinities of Macromolecules for Polyatomic Substrates. *Eur. J. Mass Spectrom.* **2012,** *18*, 223-234.

4. Fujiwara, K.; Harada, A.; Aihara, J.-i., Ch Bond Dissociation Energies of Polycyclic Aromatic Hydrocarbon Molecular Cations: Theoretical Interpretation of the (M-1)+ Peak in the Mass Spectra. *J. Mass Spectrom.* **1996,** *31*, 1216-1220.

5. Afeefy, H. Y.; Liebman, J. F.; Stein, S. E., Neutral Thermochemical Data. In *Nist Chemistry Webbook, Nist Standard Reference Database Number 69*, Linstrom, P. J.; Mallard, W. G., Eds. National Institute of Standards and Technology: Gaithersburg MD, 20899.

6. Kwon, C. H.; Kim, H. L.; Kim, M. S., Vibrational Analysis of Vacuum Ultraviolet Mass-Analyzed Threshold Ionization Spectra of Phenylacetylene and Benzonitrile. *J. Phys. Chem. A* **2003,** *107*, 10969-10975.

7. Hemberger, P.; Trevitt, A. J.; Ross, E.; da Silva, G., Direct Observation of Para-Xylylene as the Decomposition Product of the Meta-Xylyl Radical Using VUV Synchrotron Radiation. *The Journal of Physical Chemistry Letters* **2013,** *4*, 2546-2550.

8. DePuy, C. H., Interstellar Organic Chemistry and Other Applcations of Gas Phase Ion-Molecule Chemistry. *Pure Appl. Chem.* **1989,** *61*, 693-698.

9. Knapman, T. W.; Berryman, J. T.; Campuzano, I.; Harris, S. A.; Ashcroft, A. E., Considerations in Experimental and Theoretical Collision Cross-Section Measurements of Small Molecules Using Travelling Wave Ion Mobility Spectrometry-Mass Spectrometry. *Int. J. Mass spectrom.* **2010,** *298*, 17-23.

10. Beitz, T.; Laudien, R.; Löhmannsröben, H.-G.; Kallies, B., Ion Mobility Spectrometric Investigation of Aromatic Cations in the Gas Phase. *J. Phys. Chem. A* **2006,** *110*, 3514-3520.

11. Griffin, G.; Dzidic, I.; Carroll, D.; Stillwell, R.; Horning, E., Ion Mass Assignments Based on Mobility Measuremets. Validity of Plasma Chromatographic Mass Mobility Correlations. *Anal. Chem.* **1973,** *45*, 1204-1209.

12. Bodi, A.; Hemberger, P., Imaging Breakdown Diagrams for Bromobutyne Isomers with Photoelectron-Photoion Coincidence. *PCCP* **2014,** *16*, 505-515.

13. Guevremont, R.; Siu, K. W. M.; Wang, J.; Ding, L., Combined Ion Mobility/Time-of-Flight Mass Spectrometry Study of Electrospray-Generated Ions. *Anal. Chem.* **1997,** *69*, 3959-3965.

14. Bruice, P. Y., *Organic Chemistry*. 4th ed.; Pearson Education Ltd.: Toronto, 2004.

15. Bodi, A.; Hemberger, P.; Gerber, T.; Sztáray, B., A New Double Imaging Velocity Focusing Coincidence Experiment: I2pepico. *Rev. Sci. Instrum.* **2012,** *83*, -.

8 Pyrene

8.1 Introduction

Pyrene is the first example of a pericondensed PAH in our list of species. There has been another study on the dissociation of pyrene conducted by Ling et al., which shows three dissociation channels, two primary channels (H-loss and H_2-loss) and one secondary channel (2H-loss).[1] Their results show for the primary channels that H_2-loss has the lower appearance energy (15.2 eV ± 0.2 versus 16.2 eV ± 0.2) though from the breakdown curves it is quite apparent that H-loss is the dominant channel.

In this work, we are reinvestigating the dissociation of the pyrene cation using the PIRENEA setup, which consists in a cold ion cyclotron resonance (ICR) cell to simulate the interstellar environment, as well as iPEPICO which was conducted at the Swiss Light Source (SLS). Both techniques produce ions through photoionization, PIRENEA uses a Xe arc lamp for subsequent dissociation, the SLS uses VUV radiation and then ions are then allowed to dissociate spontaneously.

The PIRENEA experimental results were used to create a fragmentation map outlining all the different pathways connecting the fragments from pyrene radical cation ($C_{16}H_{10}^{+\cdot}$) down to the bare 14 carbon clusters (C_{14}^{+}) as well as all side channels which occurred. The data collected from the iPEPICO experiments was used to create breakdown curves for H-loss and 2H-loss, based on photon energy. Using RRKM, the breakdown curves were fit and the energy of activation (E_0) and entropy of activation ($\Delta^{\ddagger}S$) were extracted. These results will be compared with those of Ling et al. which were conducted using a similar process to the iPEPICO where pyrene was photoionized using VUV radiation.[1]

This work also shows theoretical structures calculated based on energetic and chemical intuition garnered from our previous work with naphthalene.[2] These calculated structures are combined with the PIRENEA results to give a better picture of what forms pyrene takes as the fragmentation progresses through 22 separate reactions.

8.2 Results and discussion

8.2.1 Calculations

Following the PIRENEA results,[3-4] the next step was to determine the likely structures of species present in the fragmentation map. Figure 40 reports all the species involved in the map and their associated structure numbers. All structures are shown in Figure 41a-c while the calculated dissociation energies can be found in Table 13.

.

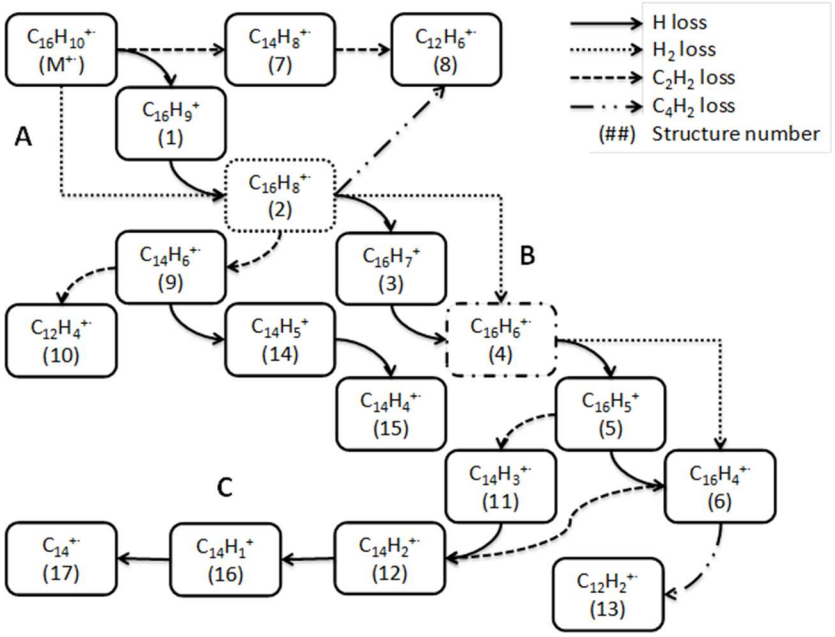

Figure 40: Schematic of fragmentation map as outlined in reference 3. A-C are to relate position of structure maps on overall map. Solid arrows indicate H loss, dashed arrows C_2H_2 loss while dash/dot arrows are C_4H_2 loss. Structure numbers are shown in parenthesis in order to link structure image to the text. The dashed lines around structures (2) and (4) represent the division structures for Figure 40a-c.

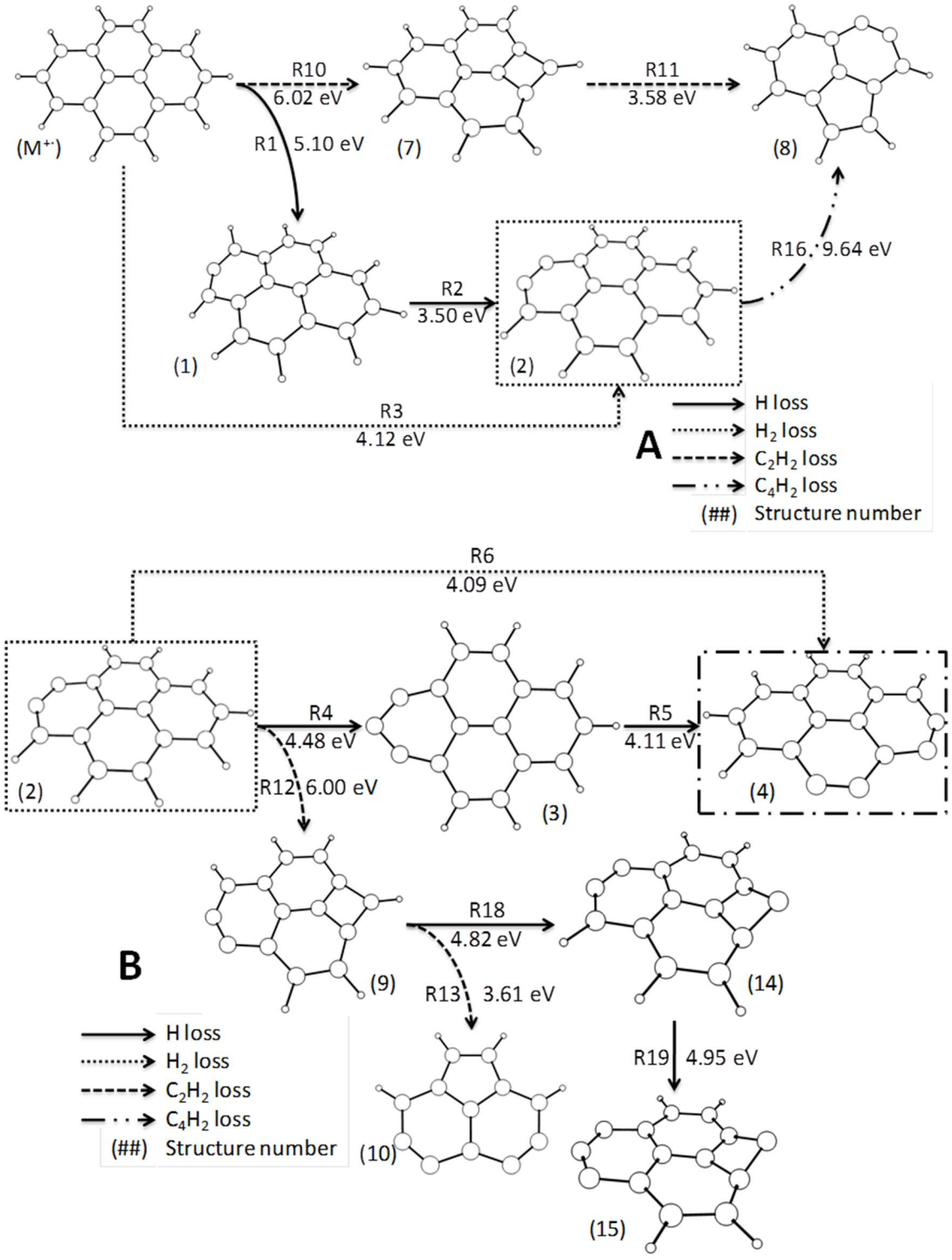
(M+·)
R10
6.02 eV
R1 5.10 eV
(7)
R11
3.58 eV
(8)
(1)
R2
3.50 eV
(2)
R16 9.64 eV
R3
4.12 eV
A
H loss
H2 loss
C2H2 loss
C4H2 loss
(##) Structure number
R6
4.09 eV
(2)
R4
4.48 eV
R12 6.00 eV
(3)
R5
4.11 eV
(4)
B
(9)
R18
4.82 eV
R13 3.61 eV
(14)
R19 4.95 eV
(10)
(15)
H loss
H2 loss
C2H2 loss
C4H2 loss
(##) Structure number

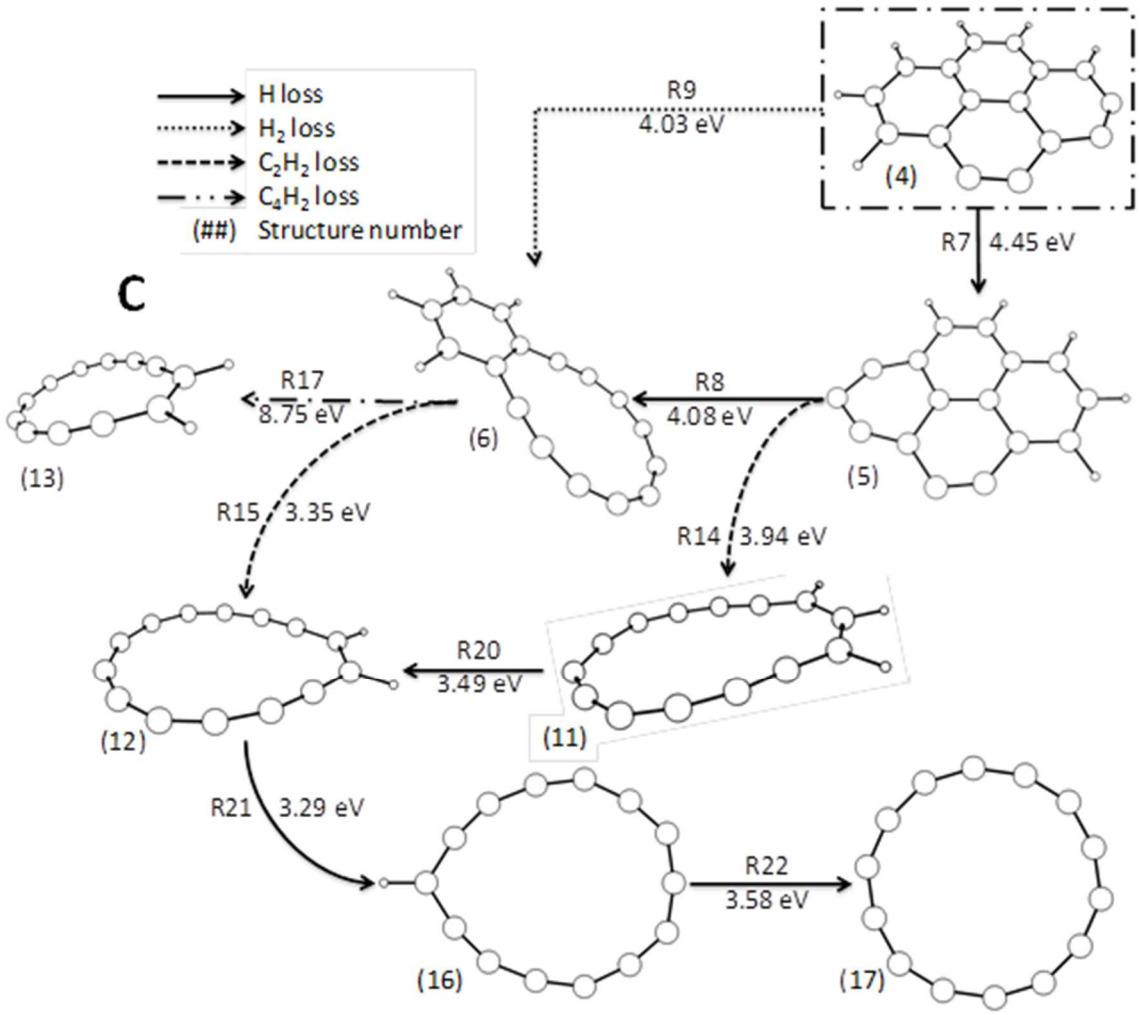

Figure 41: a) Fragmentation map with structures and dissociation energies for pyrene fragments down to $C_{16}H_8^{+\cdot}$, b) Fragmentation map with structures and dissociation enthalpies for pyrene fragmentation from $C_{16}H_8^{+\cdot}$ to $C_{16}H_6^{+}$, c) Fragmentation map with structures and dissociation energies for pyrene fragmentation from $C_{16}H_6^{+}$ to C_{14}^{+}.

Table 13: Calculated dissociation energies for reactions R1-R22 of pyrene.

Number	Reaction	ΔE (eV)	Number	Reaction	ΔE (eV)
R1	$C_{16}H_{10}^{+\cdot} \rightarrow C_{16}H_9^{+} + H$	5.10	R12	$C_{16}H_8^{+\cdot} \rightarrow C_{14}H_6^{+\cdot} + C_2H_2$	6.00
R2	$C_{16}H_9^{+} \rightarrow C_{16}H_8^{+\cdot} + H$	3.50	R13	$C_{14}H_6^{+\cdot} \rightarrow C_{12}H_4^{+\cdot} + C_2H_2$	3.61
R3	$C_{16}H_{10}^{+\cdot} \rightarrow C_{16}H_8^{+\cdot} + H_2$	4.12	R14	$C_{16}H_5^{+} \rightarrow C_{14}H_3^{+} + C_2H_2$	3.94
R4	$C_{16}H_8^{+\cdot} \rightarrow C_{16}H_7^{+} + H$	4.48	R15	$C_{16}H_4^{+\cdot} \rightarrow C_{14}H_2^{+\cdot} + C_2H_2$	3.35
R5	$C_{16}H_7^{+} \rightarrow C_{16}H_6^{+\cdot} + H$	4.11	R16	$C_{16}H_8^{+\cdot} \rightarrow C_{12}H_6^{+\cdot} + C_4H_2$	9.64
R6	$C_{16}H_8^{+\cdot} \rightarrow C_{16}H_6^{+\cdot} + H_2$	4.09	R17	$C_{16}H_4^{+\cdot} \rightarrow C_{12}H_2^{+\cdot} + C_4H_2$	8.75
R7	$C_{16}H_6^{+\cdot} \rightarrow C_{16}H_5^{+} + H$	4.45	R18	$C_{14}H_6^{+\cdot} \rightarrow C_{14}H_5^{+} + H$	4.82
R8	$C_{16}H_5^{+} \rightarrow C_{16}H_4^{+\cdot} + H$	4.08	R19	$C_{14}H_5^{+} \rightarrow C_{14}H_4^{+\cdot} + H$	4.95
R9	$C_{16}H_6^{+\cdot} \rightarrow C_{16}H_4^{+\cdot} + H_2$	4.03	R20	$C_{14}H_3^{+} \rightarrow C_{14}H_2^{+\cdot} + H$	3.49
R10	$C_{16}H_{10}^{+\cdot} \rightarrow C_{14}H_8^{+\cdot} + C_2H_2$	6.02	R21	$C_{14}H_2^{+\cdot} \rightarrow C_{14}H^{+} + H$	3.29
R11	$C_{14}H_8^{+\cdot} \rightarrow C_{12}H_6^{+\cdot} + C_2H_2$	3.58	R22	$C_{14}H^{+} \rightarrow C_{14}^{+} + H$	3.58

8.2.1.1 Dehydrogenation of $C_{16}H_m^+$

The main 'trunk' of the dissociation tree for pyrene consists of consecutive hydrogen loss. There are nine potential reactions which make up the $C_{16}H_n^+$ pathway which are as follows,

$$C_{16}H_{10}^{+\cdot}\ (M^{+\bullet}) \rightarrow H + C_{16}H_9^+\ (1) \qquad \text{(R1)}$$

$$C_{16}H_9^+\ (1) \rightarrow H + C_{16}H_8^{+\cdot}\ (2) \qquad \text{(R2)}$$

$$C_{16}H_{10}^{+\cdot}\ (M^{+\bullet}) \rightarrow H_2 + C_{16}H_8^{+\cdot}\ (2) \qquad \text{(R3)}$$

$$C_{16}H_8^{+\cdot}\ (2) \rightarrow H + C_{16}H_7^+\ (3) \qquad \text{(R4)}$$

$$C_{16}H_7^+\ (3) \rightarrow H + C_{16}H_6^{+\cdot}\ (4) \qquad \text{(R5)}$$

$$C_{16}H_8^{+\cdot}\ (2) \rightarrow H_2 + C_{16}H_6^{+\cdot}\ (4) \qquad \text{(R6)}$$

$$C_{16}H_6^{+\cdot}\ (4) \rightarrow H + C_{16}H_5^+\ (5) \qquad \text{(R7)}$$

$$C_{16}H_5^+\ (5) \rightarrow H + C_{16}H_4^{+\cdot}\ (6) \qquad \text{(R8)}$$

$$C_{16}H_6^{+\cdot}\ (4) \rightarrow H_2 + C_{16}H_4^{+\cdot}\ (6) \qquad \text{(R9)}$$

R1 consists of the first H loss, for which only three sites need to be considered, shown in Figure 1. The calculations resulted in a maximum difference in energy of only 0.25 eV between all sites. This may be an indication that due to the aromaticity of the molecule, all the H atoms are equivalent at this stage. Based on the end position being lowest in energy, $C_{16}H_9^+$ was depicted as (**1**) with a dissociation energy of 5.10 eV.

For R2, it was determined that position has a more significant effect on the energy, with the neighbouring site being 1 eV lower in energy than either of the other two possible locations. Therefore $C_{16}H_8^{+\bullet}$ was assigned (**2**) with a dissociation energy of 3.50 eV. When looking at the spectra produced from the PIRENEA experiment, the large M-2 feature

alongside this structure has led to the theory that it is possible that two competing channels are producing $C_{16}H_8^{+\bullet}$, consecutive H loss as well as H_2 loss. While the latter channel has not been observed in this work, there have been other studies where R3 is observed.[1] The assignment for R4 follows the same trend as for R2 with the H atom being removed from the already dehydrogenated ring resulting in (**3**) with a dissociation energy of 4.48 eV.

For R5, the results of dehydrogenation continue along this trend where the empty sites will pair. There is a slight change in that the pre-existing empty sites from (**3**) undergo hydrogen scrambling and the resulting structure (**4**) has two dehydrogenated carbons on two neighbouring rings, giving $C_{16}H_6^{+\bullet}$ an energy of dissociation of 4.11 eV. R7 has no empty site to pair with and therefore there is an increase in the energy requirement, with the dissociation energy being 4.45 eV and resulting in structure (**5**).

The final reaction for the dehydrogenation trunk would be R8 resulting in the formation of $C_{16}H_4^{+\bullet}$, which has the alternate structure (**6**) proposed by Lee et al.[5] While the alternate structure was calculated for all fragments from $C_{16}H_7^+$ onwards, this is the only case where this structure was significantly lower in energy, with a dissociation energy of 4.08 eV, than the pyrene structure. This is in direct agreement with literature, where the alternate structure was determined to be the most stable for $C_{16}H_4^{+\bullet}$.[5]

When each step of the two dissociation pathways (H_2 versus consecutive H loss) are compared, there is a clear difference between them, as seen in Figure 42.

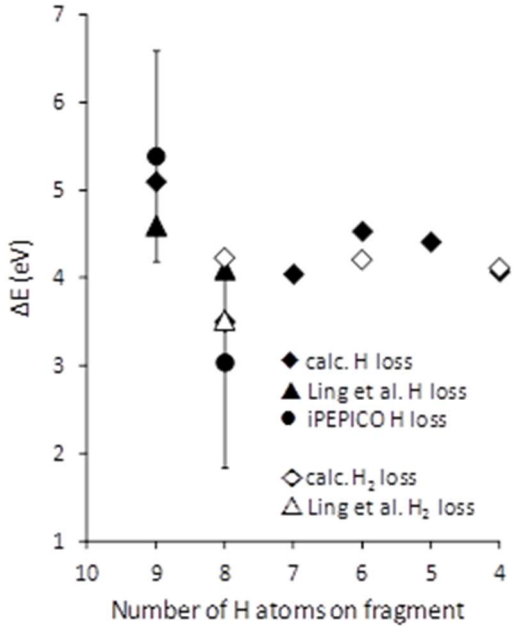

Figure 42: Reaction energies for dehydrogenation of $C_{16}H_n^+$ species. Ling et al. Points correspond to reference 1.[1] Error bars correspond to error of iPEPICO values.

For the H loss channel, there is a large drop in energy between losing the first and second hydrogen atoms. This is reasonable as the lowest energy structures with an even number of empty hydrogen sites always have them paired. In the case of H_2 loss, the trend is very linear with no big changes in energy as the molecule becomes more dehydrogenated. The idea of paired 'holes' explains this as well since two hydrogens are lost together this pairing happens automatically therefore there should be no variance. The comparison of our values with those derived for R1-3 by Ling et al.[1] can be seen in Table 14; these values fall within acceptable error, 0.5 eV for R1 and approximately 0.6 eV for R2 and R3.

Table 14: Comparison of E_0 (eV) and $\Delta^{\ddagger}S_{1000}$ (J K-1 mol-1) values for reactions R1-3.

	R1	R2	R3
E_0[a]	5.4 ± 1.2	3.3 ± 1.1	--
$\Delta^{\ddagger}S_{1000}$[a]	57 ± 89	16 ± 84	--
Calc. E_0[b]	5.1	3.5	4.12
Lit. E_0[c]	4.6	4.1	3.52
Lit. $\Delta^{\ddagger}S_{1000}$[c]	44.8	55.6	-53.1

[a] Fitted experimental iPEPICO data from this work
[b] Calculated dissociation energies
[c] Values from Ling et al.[1]

8.2.1.2 Acetylene loss

The next category of fragmentation to be discussed is that of acetylene loss. In this work, there are 6 fragments formed by acetylene losses (single or consecutive),

$$C_{16}H_{10}^{+\cdot}(M^{+\bullet}) \rightarrow C_{14}H_8^{+\cdot}(7) + C_2H_2 \quad \text{(R10)}$$

$$C_{14}H_8^{+\cdot}(7) \rightarrow C_{12}H_6^{+\cdot}(8) + C_2H_2 \quad \text{(R11)}$$

$$C_{16}H_8^{+\cdot}(2) \rightarrow C_{14}H_6^{+\cdot}(9) + C_2H_2 \quad \text{(R12)}$$

$$C_{14}H_6^{+\cdot}(9) \rightarrow C_{12}H_4^{+\cdot}(10) + C_2H_2 \quad \text{(R13)}$$

$$C_{16}H_5^{+}(5) \rightarrow C_{14}H_3^{+}(11) + C_2H_2 \quad \text{(R14)}$$

$$C_{16}H_4^{+\cdot}(6) \rightarrow C_{14}H_2^{+\cdot}(12) + C_2H_2 \quad \text{(R15)}$$

Acetylene loss doesn't appear to be able to compete with dehydrogenation on any large scale until the molecule is quite dehydrogenated. R10 is the first instance of acetylene loss, to make $C_{14}H_8^{+\cdot}$, which results in the non-planar structure (**7**) with a dissociation energy of 6.02eV. This is much greater than the competing reaction R1 (5.10 eV), which follows the results found in naphthalene and anthracene where H loss is the dominant fragment.[2, 6] $C_{14}H_8^{+\cdot}$ undergoes another acetylene loss (R11) which has a much lower energy of

dissociation of 3.58 eV resulting in structure (**8**). The next case of acetylene loss, which also happens to consist of two consecutive losses, occurs at $C_{16}H_8^{+\cdot}$ for R12 and R13. The structures calculated for these reactions, (**9**) and (**10**) respectively, look very similar to (**7**) and (**8**); they also were determined to have very similar energies with R12 having a dissociation energy of 6.00 eV while R13 was 3.61 eV.

R14, which is the acetylene loss from $C_{16}H_5^+$, shows a very different behaviour. The loss of acetylene was calculated to be comparable in energy to dehydrogenation, R8 (3.94 eV compared to 4.08 eV). R14 is also noteworthy due to it being the first instance where all organized structure is lost, yielding structure (**11**). This trend of facile acetylene loss continues with R15 when we no longer see any dehydrogenation and the energy of acetylene loss is even lower at 3.35eV and resulting in structure (**12**).

Unlike for the dehydrogenation reactions, there is no obvious trend one can derive from acetylene loss alone. The trend observed has more to do with the competition between acetylene loss and dehydrogenation. As seen in Figure 43, at early stages of dehydrogenation, there is very little competition between the two dissociations; in both cases, acetylene loss is at least 0.90 eV higher in energy.

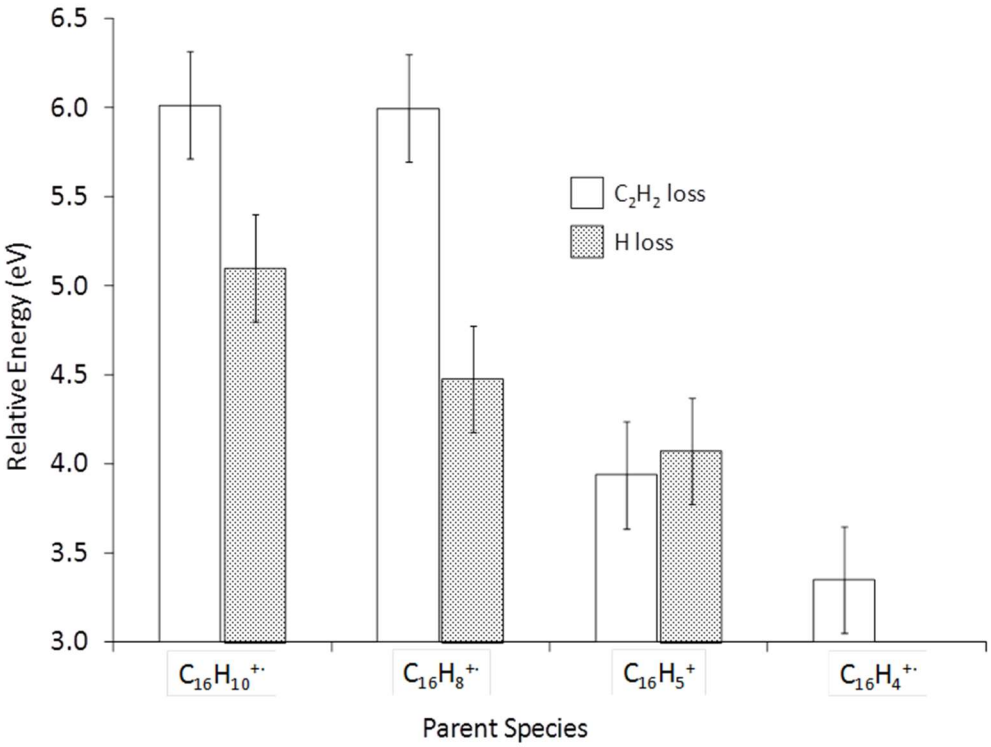

Figure 43: Bar graph comparing the energy required for different molecules to undergo dehydrogenation (light grey) and acetylene loss (white). For $C_{16}H_4^{+\cdot}$, it should be noted that no dehydrogenation was observed.

This changes dramatically at $C_{16}H_5^+$, where acetylene loss competes with dehydrogenation. For $C_{16}H_4^{+\cdot}$, dehydrogenation is no longer observed and acetylene loss is even lower in energy.

In both instances of consecutive acetylene losses, while the first acetylene loss is quite high in energy (around 6.00 eV) the second acetylene loss is dramatically easier (around 3.60 eV). This indicates that once the pyrene structure is destroyed, as both acetylene losses being discussed (structures **7** and **9**) causes the molecule to lose its planar structure, losing further hydrocarbon fragments does not involve a barrier of the same magnitude to

overcome. It seems that the first carbon loss is the limiting step. All these theoretical insights provide a very nice rationale to account for the PIRENEA measurements.[3]

8.2.1.3 Dehydrogenation of $C_{14}H_n^+$ species

Similar to the parent species, after acetylene loss the fragments undergo various stages of dehydrogenation. In the data presented here, there are two separate dehydrogenation channels starting from $C_{14}H_6^{+\cdot}$ and $C_{14}H_3^+$. The reactions are as follows,

$$C_{14}H_6^{+\cdot}\,(9) \rightarrow H + C_{14}H_5^+\,(14) \qquad \text{(R18)}$$

$$C_{14}H_5^+\,(14) \rightarrow H + C_{14}H_4^{+\cdot}\,(15) \qquad \text{(R19)}$$

$$C_{14}H_3^+\,(11) \rightarrow H + C_{14}H_2^{+\cdot}\,(12) \qquad \text{(R20)}$$

$$C_{14}H_2^{+\cdot}\,(10) \rightarrow H + C_{14}H^+\,(16) \qquad \text{(R21)}$$

$$C_{14}H^+\,(16) \rightarrow H + C_{14}^{+\cdot}\,(17) \qquad \text{(R22)}$$

Starting from $C_{14}H_6^{+\cdot}$, the molecule undergoes two consecutive dehydrogenation processes. R18 is the first reaction, which results in (**14**) with a dissociation energy of 4.82 eV. This is substantially higher in energy than the competing reaction R13 by 1.19 eV, therefore this is likely a minor reaction channel. R19, which results in (**15**) gives a similar energy of 4.95 eV.

R20-R22 are a separate reaction channel, which results in the $C_{14}^{+\cdot}$ carbon cluster. R20 consists of the first dehydrogenation of this reaction gives (**12**) with an energy of 3.49 eV. It should be noted that this is the same structure resulting from R15. This could be an indication that it doesn't matter which order the dehydrogenation occurs, be it before or after the acetylene loss. R21 and R22 continue to lose hydrogen atoms and very little change

occurs in the structures, (**16**) and (**17**) respectively, and their energies are very similar as well, corresponding to 3.29 and 3.58 eV.

The $C_{14}H_n^+$ fragments show that, in this case, consecutive dehydrogenation reactions progress with very little change in the dissociation energies of each subsequent loss and continue to complete dehydrogenation.

8.2.1.4 Diacetylene loss

There are two remaining reaction which have yet to be discussed,

$$C_{16}H_8^{+\cdot}(2) \rightarrow C_{12}H_6^{+\cdot}(8) + C_4H_2 \qquad \text{(R16)}$$

$$C_{16}H_4^{+\cdot}(6) \rightarrow C_{12}H_2^{+\cdot}(13) + C_4H_2 \qquad \text{(R17)}$$

both of which result from the loss of diacetylene. These reactions have much higher dissociation energies than all others observed which lends some doubt to how prevalent they are, especially for R16 where this same fragment is generated via R10 and R11.

The final reaction channel to be discussed is R17, which is the only route for the generation of $C_{12}H_2^{+\cdot}$ resulting in (**13**). The energy for this channel is also quite high, 8.75 eV, similar to the other diacetylene loss. This indicates how unfavourable this channel is for pericondensed PAHs, as compared to catacondensed species, like naphthalene.[2]

8.2.2 iPEPICO

iPEPICO data was collected over a large energy range, from 17-22 eV in photon energy. Three reaction channels were observed; R1 and R2 can be seen in Figure 44.

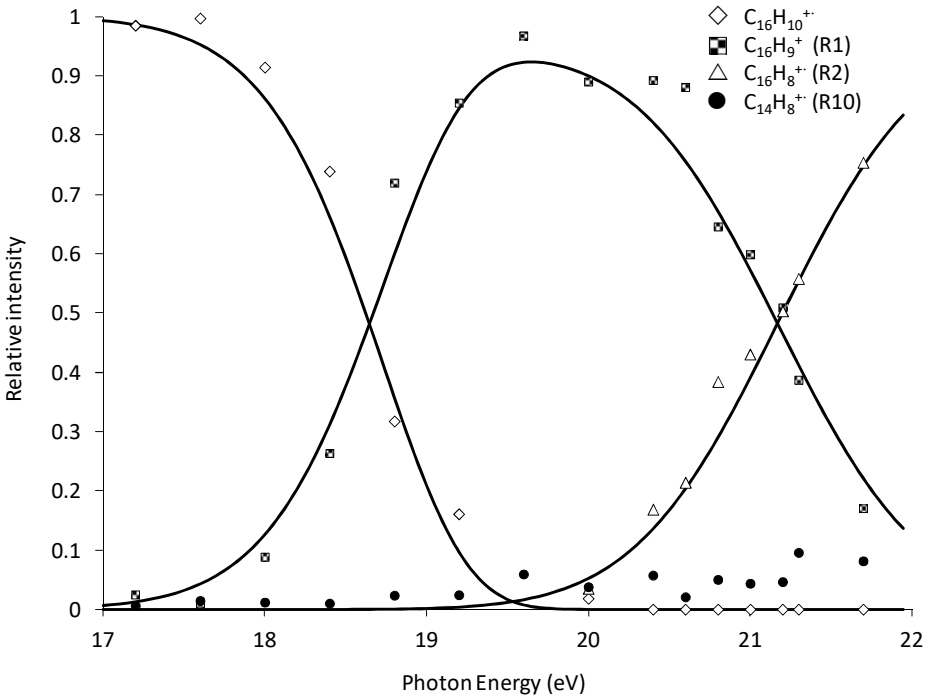

Figure 44: Experimental iPEPICO breakdown curve for the pyrene radical cation over the photon energy range of 17-29 eV. The reaction numbers for each product channel has been included in parentheses. Calculated fits are overlaid. Derived energetic and entropic parameters can be found in Table 14.

R10, while present, consists of less than 10% of the fragment ions. There is no way to restrict the fitting parameters with such low intensity, and therefore the curve can be fit with too wide a range of values to have any accuracy. Due to the low density of experimental data points, there is a wide range of possible values for all fits, though the ones shown in Table 3 yielded the best fit, though it was by a small margin. . The theoretical fitting of the breakdown curve is shown in Figure 44. The estimated values for E_0 and $\Delta^{\ddagger}S$ can be found in Table 14 along with the calculated values for those reaction channels and the literature values from Ling et al.[1] This table compares any reaction channels which are common with at least two of the three methods discussed, for this reason R3 is also listed. All the iPEPICO data was fit using RRKM theory.

For R1, the fitted values obtained were an E_0 value of 5.39 ± 1.21 eV and $\Delta^{\ddagger}S$ of 57 ± 89 J K^{-1} mol^{-1}. When the activation energy is compared to the calculated value (5.1 eV) it is a bit high but with the large error associated with the iPEPICO data it is certainly within the experimental error. When the fitted values are compared with those calculated by Ling et al. (4.60 eV), there is a large separation between the two values, though they are both within the experimental error. The entropy of activation can also be compared, with fairly good agreement between the two, the literature reported $\Delta^{\ddagger}S$ to be 44.7 J K^{-1} mol^{-1}.[1]

R2 was also compared between all three methods. The iPEPICO fitting resulted in an E_0 of 3.04 ± 1.09 eV and $\Delta^{\ddagger}S$ of 16 ± 84 J K^{-1} mol^{-1}. When comparing with the literature, the entropy of activation is quite different from the value reported (55.6 J K^{-1} mol^{-1}), same with the activation energy (4.1 eV) though both are bracketing the calculated result (3.5 eV).[1] This discrepancy is again observed when comparing the calculated and literature values for R3, with a literature value of 3.52 eV while the calculated is 4.12 eV.

8.3 Conclusion

The unimolecular dissociation of the pyrene radical cation has been investigated using a range of methods: experimentally by PIRENEA and iPEPICO and also computationally. A total of 22 reactions have been investigated by PIRENEA and 17 unique structures were calculated as a result. The dominant fragments occur from a series of consecutive H atom loss from the pyrene radical cation until $C_{16}H_4^{+\bullet}$. There is an alternating pattern to the dissociation energy due to the pairing of empty H sites when possible. The pyrene structure is well preserved until this final structure at which point the remaining hydrogens are contained on a single benzene ring and the remaining bare carbons form a single ring. Once

the PAH structure is lost, it is never restored. When $C_{16}H_4^{+\bullet}$ undergoes acetylene loss, this structure and all subsequent structures are a simple ring with any remaining hydrogens on adjacent carbon atoms. The other fragmentation routes stem from the few paths resulting from acetylene loss. As the molecule gets more dehydrogenated the acetylene loss channels become more energetically competitive. Reactions R1 and R2 were investigated further by comparison between the iPEPICO results, calculations as well as literature values. The E_0 values for the reactions are 5.4 ± 1.2 and 3.3 ± 1.1 respectively, which matches calculations quite well (5.10 eV for R1 and 3.50 eV for R2).

8.4 References for Chapter 8

1. Ling, Y.; Gotkis, Y.; Lifshitz, C., Time-Dependent Mass Spectra and Breakdown Graphs. 18. Pyrene. *Eur. J. Mass Spectrom.* **1995,** *1*, 41-49.

2. West, B.; Joblin, C.; Blanchet, V.; Bodi, A.; Sztáray, B.; Mayer, P. M., On the Dissociation of the Naphthalene Radical Cation: New iPEPICO and Tandem Mass Spectrometry Results. *J. Phys. Chem. A* **2012,** *116*, 10999-11007.

3. Useli Bacchitta, F. Photophysique Des Molécules Polycycliques Aromatiques Hydrogénées D'intérêt Interstellaire Avec L'expérience PIRENEA. l'Université Toulouse III - Paul Sabatier, Toulouse, 2009.

4. Useli-Bacchitta, F.; Bonnamy, A.; Malloci, G.; Mulas, G.; Toublanc, D.; Joblin, C., Visible Photodissociation Spectroscopy of PAH Cations and Derivatives in the PIRENEA Experiment. *Chem Phys.* **2010,** *371*, 16-23.

5. Lee, S.; Gotts, N.; von Helden, G.; Bowers, M. T., Structures of CnHx+ Molecules for $N \leq 22$ and $X \leq 5$: Emergence of PAHs and Effects of Dangling Bonds on Conformation. *J. Phys. Chem. A* **1997,** *101*, 2096-2102.

6. West, B.; Sit, A.; Mohamed, S.; Joblin, C.; Blanchet, V.; Bodi, A.; Mayer, P., Dissociation of the Anthracene Radical Cation: A Comparative Look at iPEPICO and Collision-Induced Dissociation Mass Spectrometry Results. *J. Phys. Chem. A* **2014**, submitted.

9 Conclusion

Each chapter has its own conclusion for the molecule or molecules being discussed. This global conclusion will discuss how all these results fit together and see what, if any, conclusions can be drawn. All the molecules discussed will be separated into three groups; small molecules, PAHs and the dihydroPAHs, and then any trends amongst the three groups will be discussed and what these trends can say about the potential role of the PAHs in the ISM.

The small molecules have been paired up based on their primary dissociation channel, H-loss versus C_2H_2 loss. In each pairing there is a closed and open structure which allows for the comparison of how the structure affects the dissociation. In the case of H-loss, IND and PB, it was seen that the closed structure was the more stable by 0.2 eV. Because these molecules are isomers this energy difference can only be due to structural differences. In both cases the H atom being removed is from a sp^3 carbon atom which means that there would be a small amount of rearrangement upon dissociation, which is supported by negative $\Delta^{\ddagger}S$ values. The remaining pair, BCB and EB, also have dissociations dictated by their structure. Both molecules underwent acetylene loss, with EB being the more stable example by almost 3 eV. This time, due to the cyclobutene ring, the closed structure is highly strained which facilitates the dissociation. BCB is also the only one of the small structures that has two competing dissociation channels, with H loss being only 0.2 eV higher in energy. Both channels from BCB have negative $\Delta^{\ddagger}S$ values which again illustrates the strain on the molecule as it rearranges upon dissociation, likely to more relaxed structure. EB has a positive $\Delta^{\ddagger}S$ value for acetylene loss, which normally would be

unusual, but since the ethyne tail off the benzene ring is the likeliest fragment, there is no rearrangement necessary.

All three PAHs underwent H-loss as their primary dissociation channel. There is a clear separation between the catacondensed and pericondensed molecules. NAP and ANT possessed identical dissociation energies for H-loss, 4.2 eV. This is approximately 1 eV lower in energy that the same dissociation in PYR which is reasonable with the observations that the pericondensed PAHs are more stable than the more open catacondensed molecules. While it is possible to say it is higher in energy, the data for PYR is obviously not as precise as that measured for NAP and ANT, the error associated with E_0 for PYR was greater than 1 eV, while the same measurements had much smaller error for NAP (± 0.04 eV) and ANT (± 0.3 eV). Clearly the modeling of PEPICO for larger PAH is pointless because of large kinetic shifts which result in errors in the fitted data which are so big the values can't be trusted. All the PAHs have positive $\Delta^{\ddagger}S$ values for H loss which indicates that the PAH structure remains intact as there is no sign of rearrangement for this channel. NAP and ANT underwent C2H2 loss which was competitive with H loss whereas the same channel was very minor in PYR, with it being unobservable in the iPEPICO experiments. Again there was no real difference in the between the two catacondensed molecules which indicates that size has no real effect on their dissociation.

The dihydro-PAHs were extremely interesting in their fragmentation; these were the only molecules which underwent isomerisation during the experiment. Both DHN (isomer 1 MI) and DHP (isomer 9 MF) underwent two competing H loss channels as well as methyl loss. The H loss dissociation channels resulting from the precursor ion are much lower in energy (~2 eV) than the same channel from PAHs. This is due to the H atoms being

removed; the superhydrogens of the dihydro-PAHs are not bound as tightly as the H atoms on PAHs. The $\Delta^{\ddagger}S$ values are positive for both DHN and DHP therefore no real structural changes occur at this point. Both the second H loss channel and the CH_3 loss occurred from the isomer structures (though H loss wasn't measurable from 9 MF). All the dissociation energies are on par with the primary dihydro-PAH dissociations with dissociation energies between 2-3 eV. Methyl loss indicated no rearrangement with positive $\Delta^{\ddagger}S$ values while the H loss from 1 MI possess a negative $\Delta^{\ddagger}S$ which may mean that the majority of the rearrangement occurred during isomerisation with some small changes occurring as a result of H loss.

The final observation to make is on the consecutive H loss, observed in NAP, DHN, ANT and PYR. DHN saw a very slight decrease in the dissociation energy, compared to the first H loss; nonexistent when compared to the large drop in energy reported for the PAHs (~0.2 eV for DHN compared to > 1eV for PAHs). With how much lower in energy H loss is from dihydro-PAHs it indicates that it remains facile to remove superhydrogens from PAH type molecules whereas when you are removing PAH hydrogen (those in plane with the rings) it is energetically less expensive to remove the second hydrogen atom. This observation was further expanded in the calculated results for the consecutive dehydrogenation of PYR from the precursor ion down to $C_{16}H_4^{+\bullet}$. The ion will pair up empty H sites when possible so losing an even number of H atoms is favourable.

Now that we have a good idea of trends which occur from these structures, we can start to theorize what these results tell us about the fate of PAH in the ISM. The pericondensed PAHs are more stable than their catacondensed counterparts, an observation supported by literature which indicates that the interstellar PAHs are most likely those with

a higher C to H ratio.[1] Based on this knowledge, the likelihood of PAHs being involved in the formation of acetylene is unlikely, the PAH structure is too stable. It was also determined that PAHs would likely not catalyze the formation of molecular hydrogen. Based on the results from the dihydro-PAHs, PAHs can lose superhydrogen atoms fairly easily. If hydrogen atoms can absorb on the surface it can be straightforward to remove them and the PAH structure, baring isomerisation, would be retained throughout the process. The isomerisation does cause a problem though, as it seems to occur before any dissociation and in order for the PAH structure to be retained, the ion will isomerise back prior to dissociation. There was also no evidence of H_2-loss from the dihydroPAHs (DHN only lost H_2 as a consecutive process). Based on these results, not only are PAHs not catalysts for this process, they cannot even be considered as a source of molecular hydrogen.

1. Weisman, J. L.; Lee, T. J.; Salama, F.; Head-Gordon, M., Time-Dependent Density Functional Theory Calculations of Large Compact Polycyclic Aromatic Hydrocarbon Cations: Implications for the Diffuse Interstellar Bands. *The Astrophysical Journal* **2003,** *587*, 256.

10 Appendix

Full reference details for Gaussian program

Frisch, M. J.; Trucks, G. W.; Schlegel, H. B.; Scuseria, G. E.; Robb, M. A.; Cheeseman, J. R.; Scalmani, G.; Barone, V.; Mennucci, B.; Petersson, G. A.; Nakatsuji, H.; Caricato, M.; Li, X.; Hratchian, H. P.; Izmaylov, A. F.; Bloino, J.; Zheng, G.; Sonnenberg, J. L.; Hada, M.; Ehara, M.; Toyota, K.; Fukuda, R.; Hasegawa, J.; Ishida, M.; Nakajima, T.; Honda, Y.; Kitao, O.; Nakai, H.; Vreven, T.; Montgomery, J. A.; Peralta, J. E.; Ogliaro, F.; Bearpark, M.; Heyd, J. J.; Brothers, E.; Kudin, K. N.; Staroverov, V. N.; Kobayashi, R.; Normand, J.; Raghavachari, K.; Rendell, A.; Burant, J. C.; Iyengar, S. S.; Tomasi, J.; Cossi, M.; Rega, N.; Millam, J. M.; Klene, M.; Knox, J. E.; Cross, J. B.; Bakken, V.; Adamo, C.; Jaramillo, J.; Gomperts, R.; Stratmann, R. E.; Yazyev, O.; Austin, A. J.; Cammi, R.; Pomelli, C.; Ochterski, J. W.; Martin, R. L.; Morokuma, K.; Zakrzewski, V. G.; Voth, G. A.; Salvador, P.; Dannenberg, J. J.; Dapprich, S.; Daniels, A. D.; Farkas; Foresman, J. B.; Ortiz, J. V.; Cioslowski, J.; Fox, D. J., Gaussian 09, Revision D.01. Wallingford CT, 2009.

10.1 Naphthalene

Table A1: Vibrational frequencies (cm^{-1}) of neutral naphthalene, naphthalene radical cation and initial transition state estimates for fragmentation products. Frequencies in brackets indicate the frequency removed for each transition state, which were subsequently scaled during the fitting exercise according to the procedure outlined in the methods section. Bottom three values for M, $M^{+\bullet}$ and $M\text{-}H^{+}$ are the rotational constants used for fitting, values are in GHz.

$C_{10}H_8$ (M)	$C_{10}H_8^{+\bullet}$ ($M^{+\bullet}$)	TS $(M\text{-}H)^+$	TS $(M\text{-}C_2H_2)^{+\bullet}$	TS $(M\text{-}C_4H_2)^{+\bullet}$	TS $(M\text{-}H_2)^{+\bullet}$	$(M\text{-}H)^+$	TS $[(M\text{-}H)\text{-}C_4H_2]^+$	TS $[(M\text{-}H)\text{-}H]^{+\bullet}$
176	158	*(3236)*	*(1417)*	*(1244)*	*(3236)*	150	*(1816)*	*(3212)*
187	183	148	144	126	118	187	125	236
364	357	172	166	146	137	245	155	294
398	376	336	325	286	268	306	204	385
482	426	353	342	301	282	379	254	481
490	438	401	388	341	320	428	314	595
517	474	438	438	438	438	475	428	428
519	514	474	474	474	474	534	475	475
633	557	514	514	514	514	538	534	534
634	609	557	557	557	557	597	538	538

730	731	609	609	609	609	653	597	597
773	754	731	731	731	731	686	653	653
783	775	754	754	754	754	731	686	686
801	778	775	775	775	775	760	731	731
807	808	778	778	778	778	768	760	760
850	877	808	808	808	808	842	768	768
899	937	877	877	877	877	847	842	842
948	941	937	937	937	937	871	847	847
956	981	941	941	941	941	948	871	871
977	1004	981	981	981	981	973	948	948
992	1023	1004	1004	1004	1004	980	973	973
1000	1027	1023	1023	1023	1023	1018	980	980
1040	1042	1027	1027	1027	1027	1034	1018	1018
1052	1071	1042	1042	1042	1042	1070	1034	1034
1154	1125	1071	1071	1071	1071	1124	1070	1070
1177	1128	1125	1125	1125	1125	1182	1124	1124
1181	1199	1128	1128	1128	1128	1206	1182	1182
1192	1211	1199	1199	1199	1199	1227	1206	1206
1239	1244	1211	1211	1211	1211	1254	1227	1227
1275	1265	1244	1244	1265	1244	1286	1254	1254
1294	1310	1265	1265	1310	1265	1333	1286	1286
1405	1417	1310	1310	1417	1310	1391	1333	1333
1412	1428	1417	1428	1428	1417	1448	1391	1391
1427	1440	1428	1440	1440	1428	1487	1448	1448
1499	1477	1440	1477	1477	1440	1511	1487	1487
1503	1512	1477	1512	1512	1477	1584	1511	1511
1559	1518	1512	1518	1518	1512	1643	1584	1584
1622	1560	1518	1560	1560	1518	1816	1643	1643
1648	1578	1560	1578	1578	1560	3200	3200	1816
1679	1632	1578	1632	1632	1578	3212	3212	3200
3174	3209	1632	3209	3209	1632	3222	3222	3222
3175	3211	3209	3211	3211	3209	3230	3230	3230
3177	3211	3211	3211	3211	3211	3232	3232	3232
3181	3213	3211	3213	3213	3211	3241	3241	3241
3192	3226	3213	3226	3226	3213	3259	3259	3259
3193	3226	3226	3226	3226	3226			
3205	3236	3226	3236	3236	3236			
3206	3236	3236	3236	3236	3236			
3.11	3.18					3.39		
1.23	1.24					1.20		
0.88	0.89					0.89		

10.2 1,2-dihydronaphthalene and 9,10-dihydrophenanthrene

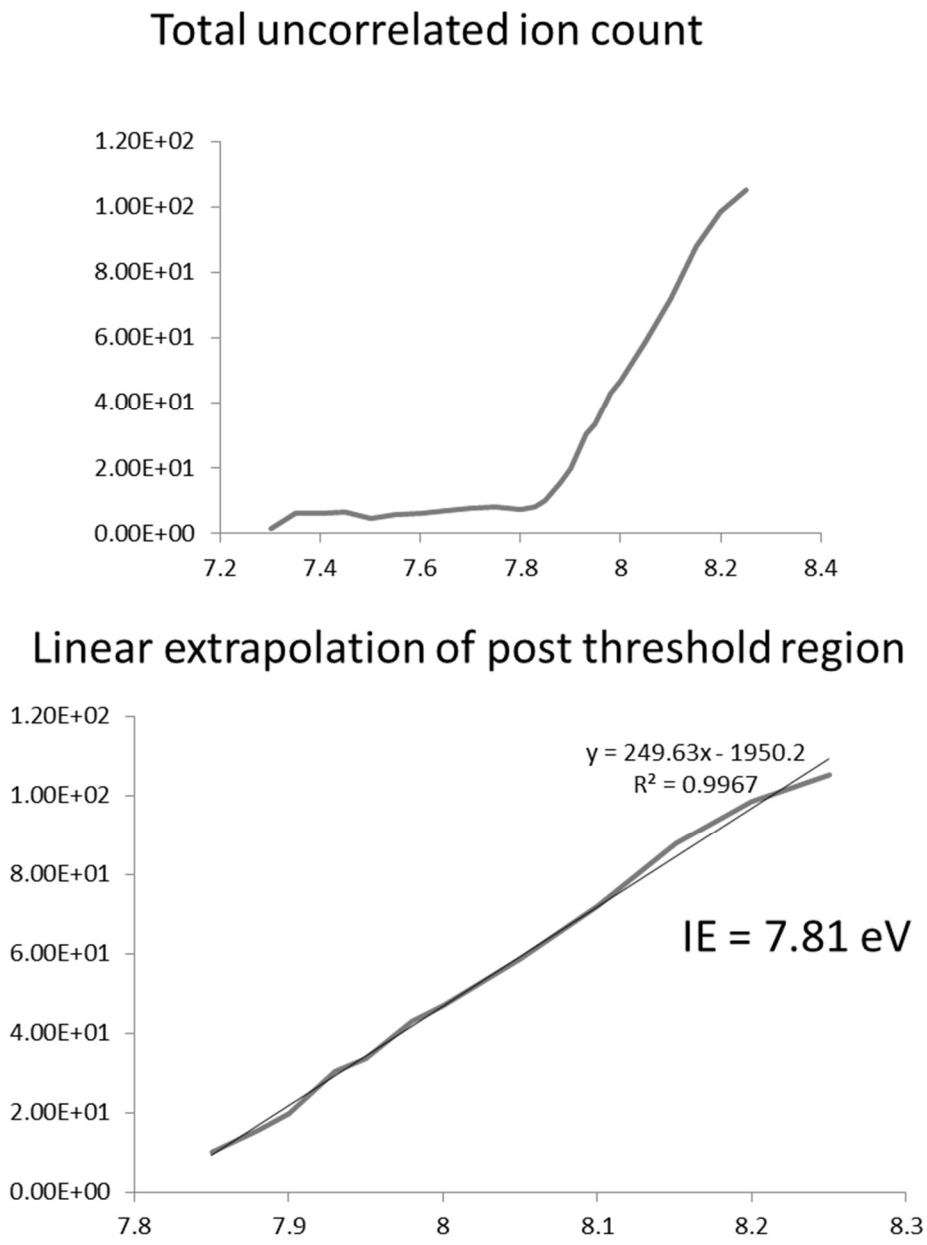

Figure A1: Determination of IE for 9,10-dihydrophenanthrene

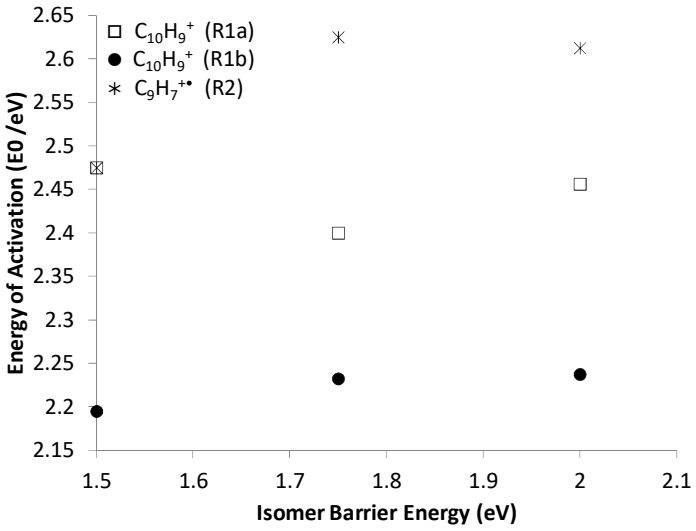

Figure A2: Plot of 0K activation energy for all three primary channels (R1a-b, R2) versus isomerization barrier energy ranging from 1.5-2.0 eV

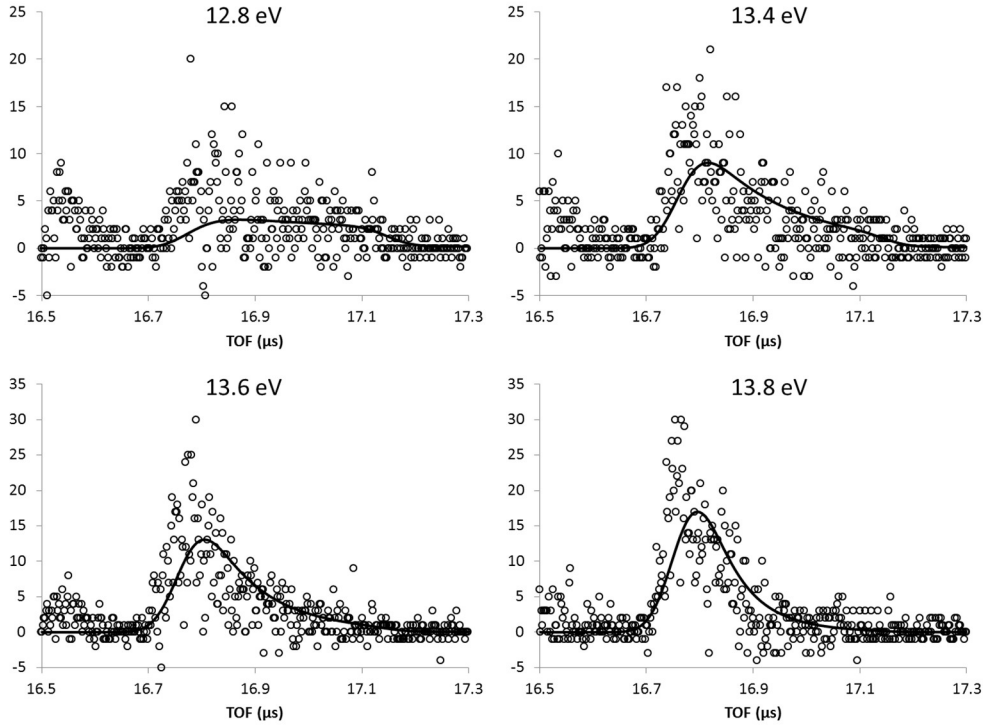

Figure A3: Representative TOF fits, for 9,10-dihydrophenanthrene, calculated during the RRKM fitting of experimental iPEPICO data. The region shown is the $C_{13}H_9^+$ region, as this peak was the only asymmetric TOF peak which was not obscured due to its proximity to its proximity to other peaks. As photon energy increases, it can be seen that the peak becomes increasingly Gaussian in shape.

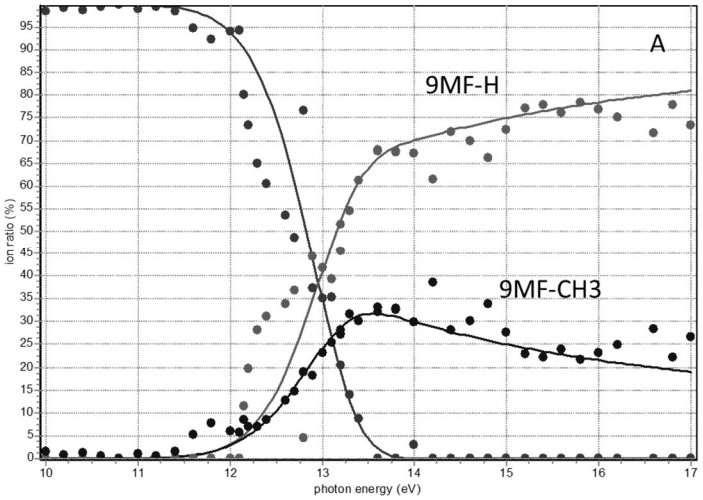

2 eV barrier height
No restrictions to calculation

Demonstrating unreasonable
Δ‡S(1000K) values when using
9MF-H instead of DHP-H

transition	E0 (eV)	Δ‡S(1000K)
DHP → 9MF	2.18	93.1391
DHP ← 9MF	2.15	82.0243
9MF-H	2.34	-9.0746
9MF-CH3	2.74	-31.9366

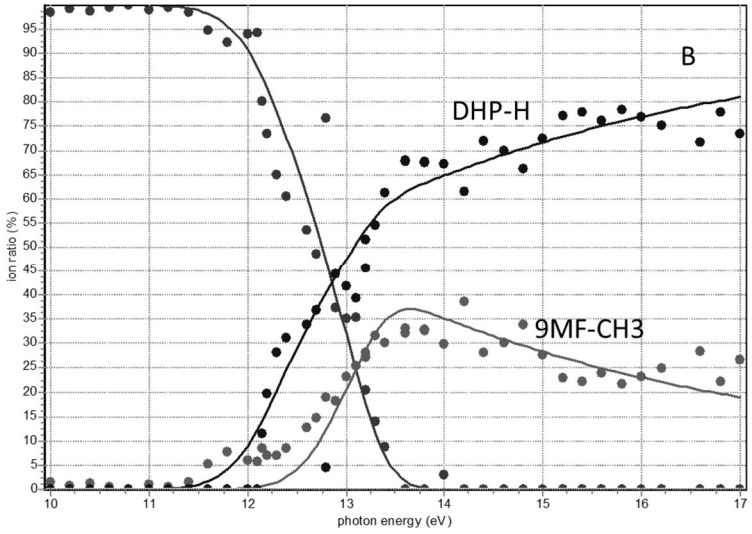

1.75 eV barrier

No restrictions on calculation

transition	E0 (eV)	Δ‡S(1000K)
DHP → 9MF	1.90	-19.1715
DHP ← 9MF	2.08	-30.2863
DHP-H	2.25	0.3535
9MF-CH3	2.50	11.3751

Figure A4: Various iPEPICO RRKM fittings for 9,10-dihydrophenanthrene to demonstrate (A) the effect of choosing to remove hydrogen from 9-methylfluorene, (B) the effect of barrier height on energetic values.

Table A2: Vibrational frequencies (cm^{-1}) used in the RRKM calculations outlined in this paper. Frequencies in parenthesis were removed for the transition state.

1,2-dihydronaphthalene

$C_{10}H_{10}$ (M)	$C_{10}H_{10}^{+\cdot}$ ($M_{DHN}^{+\cdot}$)	$C_{10}H_{10}^{+\cdot}$ ($M_{MI}^{+\cdot}$)	TS (DHN-MI)$^{+\cdot}$	TS $(M_{DHN}\text{-}H)^+$	TS $(M_{MI}\text{-}H)^+$	TS $(M_{MI}\text{-}CH_3)^+$	$(M_{DHN}\text{-}H)^+$	TS $[(M_{DHN}\text{-}H)\text{-}H]^{+\cdot}$	TS $[(M_{DHN}\text{-}H)\text{-}H_2]^+$
140	120	94	(706)	(3120)	(3001)	(1001)	121	(3206)	(3206)
161	144	155	104	78	132	48	175	97	97
278	244	229	170	94	217	79	253	140	140
366	351	250	252	158	321	117	357	202	202
408	370	263	275	228	349	127	410	286	286
440	433	385	290	240	369	134	439	328	328
506	486	431	433	433	385	385	497	439	439
520	502	483	486	486	431	431	503	497	497
583	518	501	502	502	483	483	506	503	503
615	597	540	518	518	501	501	613	506	506
722	706	596	597	597	540	540	680	613	613
735	722	716	722	706	596	596	749	680	680
785	759	729	759	722	716	716	751	749	749
794	801	758	801	759	729	729	792	751	751
833	830	785	830	801	758	758	801	792	792
854	859	836	859	830	785	785	867	801	801
931	930	863	930	859	836	836	930	867	867
934	941	894	941	930	863	863	934	930	930
985	974	911	974	941	894	894	973	934	934
1006	1014	976	1014	974	911	911	1000	973	973
1040	1050	994	1050	1014	976	976	1026	1000	1000
1048	1062	1001	1062	1050	994	994	1041	1026	1026

$C_{10}H_{10}$ (M)	$C_{10}H_{10}^{+\cdot}$ ($M_{DHN}^{+\cdot}$)	$C_{10}H_{10}^{+\cdot}$ ($M_{MI}^{+\cdot}$)	TS $(DHN\text{-}MI)^{+\cdot}$	TS $(M_{DHN}\text{-}H)^{+}$	TS $(M_{MI}\text{-}H)^{+}$	TS $(M_{MI}\text{-}CH_3)^{+}$	$(M_{DHN}\text{-}H)^{+}$	TS $[(M_{DHN}\text{-}H)\text{-}H]^{+\cdot}$	TS $[(M_{DHN}\text{-}H)\text{-}H_2]^{+}$
1072	1074	1009	1074	1062	1001	1009	1049	1041	1041
1100	1077	1019	1077	1074	1009	1019	1050	1049	1049
1104	1087	1063	1087	1077	1019	1063	1114	1050	1050
1181	1193	1092	1193	1087	1063	1092	1157	1114	1114
1223	1216	1098	1216	1193	1092	1098	1180	1157	1157
1227	1239	1140	1239	1216	1098	1140	1193	1180	1180
1244	1245	1177	1245	1239	1140	1177	1201	1193	1193
1265	1261	1184	1261	1245	1177	1184	1218	1201	1201
1281	1301	1246	1301	1261	1184	1246	1271	1218	1218
1305	1317	1266	1317	1301	1246	1266	1300	1271	1271
1362	1357	1280	1357	1317	1266	1280	1341	1300	1300
1372	1412	1317	1412	1357	1280	1317	1374	1341	1341
1434	1437	1380	1437	1412	1317	1380	1393	1374	1374
1441	1461	1412	1461	1437	1380	1412	1449	1393	1393
1492	1513	1422	1513	1461	1412	1422	1475	1449	1449
1548	1520	1445	1520	1513	1422	1445	1488	1475	1475
1554	1537	1457	1537	1520	1445	1457	1544	1488	1488
1561	1546	1497	1546	1537	1457	1497	1584	1544	1544
1593	1572	1497	1572	1546	1497	1497	1609	1584	1584
1695	1610	1509	1610	1572	1497	1509	1653	1609	1609
1730	1631	1550	1631	1610	1509	1550	2972	1653	1653
1776	1721	1644	1721	1631	1550	1644	2975	2972	2972
3094	3084	3001	3084	1721	1644	3001	3168	2975	2975
3107	3120	3047	3120	3084	3047	3047	3177	3168	3168
3173	3198	3123	3198	3198	3123	3123	3181	3177	3177
3178	3216	3125	3216	3216	3125	3125	3185	3181	3181
3269	3303	3187	3303	3303	3187	3187	3192	3185	3185
3274	3312	3196	3312	3312	3196	3196	3204	3192	3192
3279	3315	3200	3315	3315	3200	3200	3206	3204	3204
3292	3318	3205	3318	3318	3205	3205			
3294	3325	3210	3325	3325	3210	3210			
3309	3337	3223	3337	3337	3223	3223			

9,10-dihydrophenanthrene

$C_{14}H_{12}$ (M)	$C_{14}H_{12}^{+\cdot}$ ($M_{DHP}^{+\cdot}$)	$C_{14}H_{12}^{+\cdot}$ ($M_{9MF}^{+\cdot}$)	TS (DHP-9MF)$^{+\cdot}$	TS (M_{DHP}-H)$^{+}$	TS (M_{9MF}-CH_3)$^{+}$
86	72	69	(288)	(3194)	(1080)
104	94	121	40	46	65
177	157	123	70	60	114
209	198	197	71	101	116
269	258	218	114	126	185
318	288	238	127	165	205
392	383	279	383	288	238
397	393	340	393	383	279
456	433	399	433	393	340
468	459	421	459	433	399
470	474	466	474	459	421
504	477	496	477	474	466
554	500	512	500	477	496
578	529	513	529	500	512
612	588	564	588	529	513
636	620	614	620	588	564
721	704	618	704	620	614
739	718	709	718	704	618
741	720	741	720	718	709
759	772	753	772	720	741
784	778	773	778	772	753
792	809	797	809	778	773
818	816	798	816	809	797
880	880	821	880	816	798
882	882	890	882	880	821
908	892	893	892	882	890
959	983	987	983	892	893
959	991	990	991	983	987
988	994	991	994	991	990
990	1003	1001	1003	994	991
993	1018	1016	1018	1003	1001
1023	1019	1017	1019	1018	1016
1049	1034	1023	1034	1019	1017
1068	1048	1027	1048	1034	1023
1069	1052	1062	1052	1048	1027
1111	1115	1080	1115	1052	1062
1150	1156	1132	1156	1115	1132
1181	1182	1134	1182	1156	1134
1184	1187	1177	1187	1182	1177
1188	1195	1183	1195	1187	1183

1208	1199	1190	1199	1195	1190
1217	1229	1197	1229	1199	1197
1224	1236	1234	1236	1229	1234
1278	1285	1260	1285	1236	1260
1304	1299	1302	1299	1285	1302
1306	1318	1335	1318	1299	1335
1328	1353	1360	1353	1318	1360
1335	1360	1380	1360	1353	1380
1362	1379	1403	1379	1360	1403
1380	1398	1421	1398	1379	1421
1471	1455	1442	1455	1398	1442
1474	1459	1459	1459	1455	1459
1484	1471	1485	1471	1459	1485
1485	1473	1498	1473	1471	1498
1516	1495	1500	1495	1473	1500
1521	1507	1512	1507	1495	1512
1602	1537	1538	1537	1507	1538
1622	1548	1565	1548	1537	1565
1637	1615	1608	1615	1548	1608
1646	1635	1650	1635	1615	1650
2990	2996	3016	2996	1635	3016
3002	3009	3045	3009	2996	3045
3066	3095	3118	3095	3095	3118
3066	3096	3119	3096	3096	3119
3154	3184	3185	3184	3184	3185
3155	3184	3186	3184	3184	3186
3166	3194	3193	3194	3194	3193
3168	3195	3195	3195	3195	3195
3178	3202	3198	3202	3202	3198
3182	3205	3199	3205	3205	3199
3189	3214	3209	3214	3214	3209
3193	3226	3210	3226	3226	3210

10.3 Anthracene

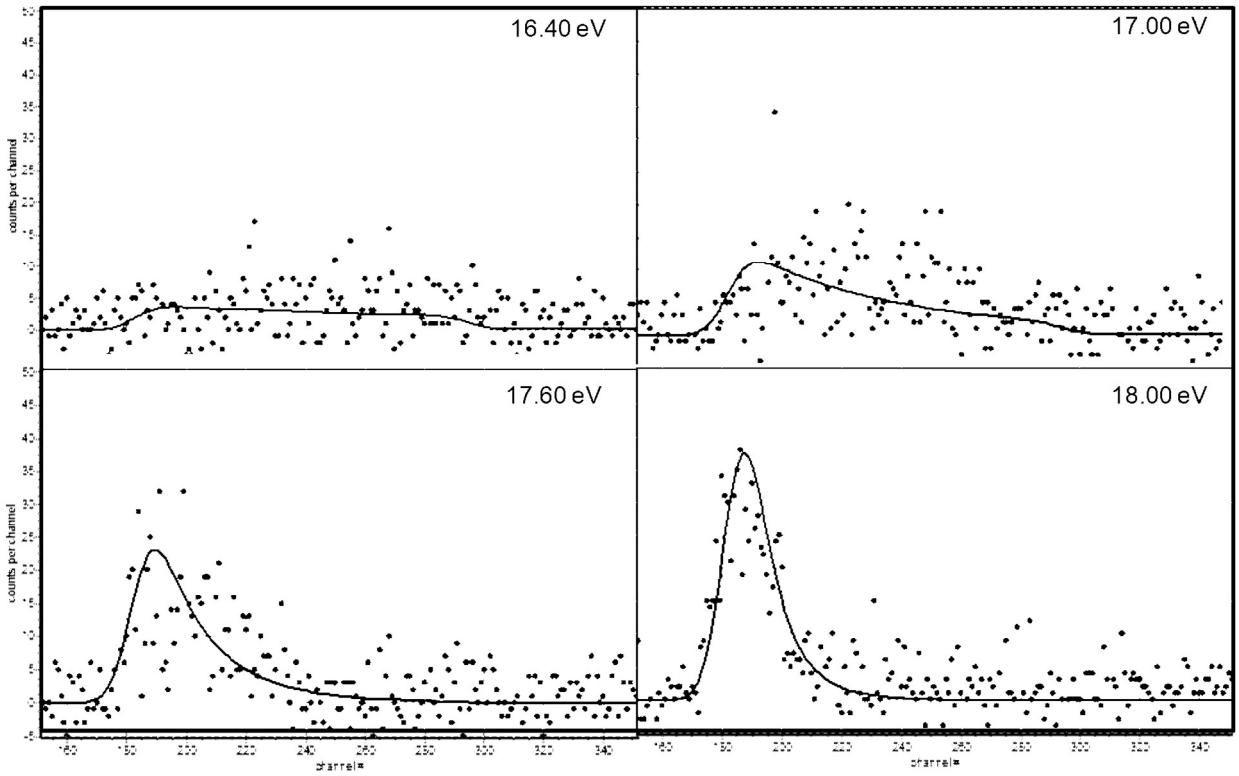

Figure A5: Illustrative TOF fittings for iPEPICO TOF focussing on the asymmetric $[M\text{-}C_2H_2]^{+\cdot}$ peak from the dissociation of the anthracene radical cation. It is demonstrating the appearance and eventual formation of the Gaussian shape. Photon energies for each spectrum is listed

Table A3: Vibrational frequencies (cm^{-1}) of neutral anthracene, anthracene radical cation and initial transition state estimates for fragmentation products. Frequencies in brackets indicate the frequency removed for each transition state, which were subsequently

$C_{14}H_{10}$ (M)	$C_{14}H_{10}^{+\cdot}$ ($M^{+\cdot}$)	TS $(M\text{-}H)^{+}$	TS $(M\text{-}C_2H_2)^{+\cdot}_{\sigma=6}$	TS $(M\text{-}C_2H_2)^{+\cdot}_{\sigma=1}$	$C_{14}H_9^{+}$ $(M\text{-}H)^{+}$	TS $[(M\text{-}H)\text{-}H]^{+\cdot}$
95	90	(3335)	(1411)	(1411)	90	(3229)
127	126	67	70	47	121	90
242	228	94	98	67	227	121
246	239	171	178	121	238	227
280	284	179	186	127	276	238
405	393	213	222	151	357	276
407	402	393	393	393	382	357
411	407	402	402	402	391	382
501	459	407	407	407	423	391
507	479	459	459	459	433	423
525	501	479	479	479	476	433
551	532	501	501	501	514	476
611	581	532	532	532	539	514
635	629	581	581	581	584	539
661	644	629	629	629	608	584
682	688	644	644	644	629	608
777	753	688	688	688	708	629
781	769	753	753	753	739	708
795	793	769	769	769	755	739
806	803	793	793	793	765	755
807	812	803	803	803	772	765
851	866	812	812	812	782	772
885	915	866	866	866	817	782
907	944	915	915	915	832	817
950	947	944	944	944	881	832
950	957	947	947	947	919	881
960	977	957	957	957	924	919
1026	990	977	977	977	936	924
1032	1044	990	990	990	962	936
1051	1051	1044	1044	1044	996	962
1052	1079	1051	1051	1051	1025	996
1063	1080	1079	1079	1079	1049	1025
1069	1094	1080	1080	1080	1085	1049
1173	1095	1094	1094	1094	1098	1085
1186	1167	1095	1095	1095	1157	1098
1222	1204	1167	1167	1167	1182	1157
1238	1228	1204	1204	1204	1200	1182
1239	1249	1228	1228	1228	1217	1200
1261	1254	1249	1249	1249	1233	1217

1342	1258	1254	1254	1254	1272	1233
1343	1332	1258	1258	1258	1299	1272
1353	1355	1332	1332	1332	1310	1299
1397	1361	1355	1355	1355	1337	1310
1415	1368	1361	1361	1361	1382	1337
1476	1411	1368	1368	1368	1413	1382
1490	1470	1411	1470	1470	1417	1413
1503	1483	1470	1483	1483	1441	1417
1550	1492	1483	1492	1492	1481	1441
1553	1552	1492	1552	1552	1498	1481
1587	1555	1552	1555	1555	1536	1498
1661	1599	1555	1599	1599	1593	1536
1682	1607	1599	1607	1607	1600	1593
1705	1650	1607	1650	1650	1643	1600
1758	1652	1650	1652	1652	1711	1643
1762	1685	1652	1685	1685	3188	1711
3276	1694	1685	1694	1694	3200	3188
3277	3302	1694	3302	3302	3203	3200
3281	3304	3302	3304	3304	3205	3203
3282	3309	3304	3309	3309	3207	3205
3285	3310	3309	3310	3310	3212	3207
3287	3312	3310	3312	3312	3218	3212
3300	3313	3312	3313	3313	3228	3218
3300	3325	3313	3325	3325	3229	3228
3312	3325	3325	3325	3325		
3312	3335	3325	3335	3335		
3325	3335	3335	3335	3335		
2.172	2.179				2.155	
0.456	0.456				0.464	
0.377	0.377				0.382	

10.4 Small Molecules

Table A4: Vibrational frequencies (cm^{-1}) of the neutral, radical cation and the estimated transition states for the relevant fragmentation channels for each molecule. The frequencies listed in brackets represent the frequency removed from the original $M^{+\cdot}$ to simulate the transition state. These frequencies were scaled in the final fitting by a value of 0.964. The bottom three values for M and $M^{+\cdot}$ (for each molecule) are the rotational constants used for the fitting with units of GHz.

1-propynylbenzene			Indene			Benzocyclobutene			1-ethynylbenzene		
C_9H_8 (M)	$C_9H_8^{+\cdot}$ ($M^{+\cdot}$)	TS $(M\text{-}H)^+$	C_9H_8 (M)	$C_9H_8^{+\cdot}$ ($M^{+\cdot}$)	TS $(M\text{-}H)^+$	C_8H_8 (M)	$C_8H_8^{+\cdot}$ ($M^{+\cdot}$)	TS $(M\text{-}H)^+$	TS $(M\text{-}C_2H_2)^{+\cdot}$	C_8H_6 (M)	$C_8H_6^{+\cdot}$ ($M^{+\cdot}$)	TS $(M\text{-}C_2H_2)^{+\cdot}$
21	26	(3113)	194	160	(3026)	189	137	(3050)	(779)	141	118	(2109)
93	84	55	210	201	241	214	195	171	189	161	154	40
93	93	177	387	339	302	400	357	243	270	367	321	52
245	228	196	396	392	509	414	374	445	494	409	359	109
303	305	478	427	412	588	488	390	466	517	473	468	134
402	364	640	542	474	618	549	539	486	539	539	469	159
404	396	364	562	525	474	645	544	539	539	550	530	469
410	405	396	605	594	525	717	568	544	544	636	580	530
542	502	405	708	691	594	728	661	568	568	647	637	580
550	528	502	733	732	691	793	762	661	661	697	703	637
637	594	528	744	742	732	795	779	762	762	703	744	703
703	644	594	783	807	742	866	855	779	855	774	764	744
715	708	644	844	830	807	881	878	855	878	775	800	764
772	798	708	872	867	830	908	912	878	912	854	821	800
852	826	798	873	878	867	949	949	912	949	936	982	821
932	963	826	937	949	878	995	984	949	984	987	995	982
985	978	963	955	950	949	1021	1008	984	1008	1005	1007	995
985	986	978	956	979	950	1046	1016	1008	1016	1014	1017	1007
1002	1004	986	968	1002	979	1094	1057	1016	1057	1048	1025	1017

1-propynylbenzene			Indene			Benzocyclobutene				1-ethynylbenzene		
C_9H_8 (M)	$C_9H_8^{+\cdot}$ ($M^{+\cdot}$)	TS $(M-H)^+$	C_9H_8 (M)	$C_9H_8^{+\cdot}$ ($M^{+\cdot}$)	TS $(M-H)^+$	C_8H_8 (M)	$C_8H_8^{+\cdot}$ ($M^{+\cdot}$)	TS $(M-H)^+$	TS $(M-C_2H_2)^{+\cdot}$	C_8H_6 (M)	$C_8H_6^{+\cdot}$ ($M^{+\cdot}$)	TS $(M-C_2H_2)^{+\cdot}$
1016	1013	1004	992	1009	1002	1100	1074	1057	1074	1100	1111	1025
1050	1014	1013	1040	1021	1009	1151	1118	1074	1118	1183	1173	1111
1050	1025	1014	1088	1094	1021	1175	1173	1118	1173	1200	1208	1173
1054	1040	1025	1132	1135	1094	1183	1188	1173	1188	1222	1264	1208
1099	1112	1040	1149	1162	1135	1206	1214	1188	1214	1313	1297	1264
1182	1181	1112	1177	1173	1162	1219	1216	1214	1216	1352	1385	1297
1200	1210	1181	1186	1184	1173	1231	1236	1216	1236	1472	1433	1385
1291	1304	1210	1227	1246	1184	1305	1317	1236	1317	1520	1479	1433
1310	1348	1304	1249	1275	1246	1365	1384	1317	1384	1609	1531	1479
1352	1380	1348	1314	1325	1275	1464	1390	1384	1390	1639	1643	1531
1416	1382	1380	1345	1378	1325	1479	1435	1390	1435	2202	2109	1643
1471	1433	1382	1389	1410	1378	1488	1451	1435	1451	3166	3191	3191
1478	1442	1433	1436	1422	1410	1495	1463	1451	1463	3175	3202	3202
1479	1444	1442	1486	1446	1422	1634	1510	1463	1510	3185	3205	3205
1524	1493	1444	1490	1462	1446	1641	1578	1510	1578	3193	3214	3214
1607	1537	1493	1597	1507	1462	3040	3039	1578	3039	3197	3216	3216
1640	1636	1537	1631	1550	1507	3045	3050	3039	3050	3476	3416	3416
2333	2230	1636	1648	1650	1550	3078	3080	3080	3080	5.697	5.452	
3020	3008	2230	3016	3026	1650	3093	3093	3093	3093	1.531	1.562	
3074	3057	3008	3038	3050	3050	3156	3189	3189	3189	1.207	1.214	
3080	3113	3057	3157	3189	3189	3165	3197	3197	3197			
3164	3191	3191	3163	3197	3197	3174	3210	3210	3210			
3172	3201	3201	3174	3201	3201	3184	3211	3211	3211			
3183	3204	3204	3187	3211	3211	4.463	4.260					
3190	3213	3213	3189	3212	3212	2.082	2.129					
3195	3216	3216	3213	3227	3227	1.445	1.445					
5.510	5.300		3.788	3.697								
0.823	0.839		1.580	1.601								
0.719	0.727		1.122	1.125								

10.5 Pyrene

Table A5: Vibrational frequencies (cm^{-1}) of neutral pyrene, pyrene radical cation and initial transition state estimates for fragmentation products. Frequencies in brackets indicate the frequency removed for each transition state, which were subsequently scaled during the fitting exercise according to the procedure outlined in the methods section. Bottom three values for M, $M^{+\bullet}$ and $M\text{-}H^{+}$ are the rotational constants used for fitting, values are in GHz

$C_{16}H_{10}$ (M)	$C_{16}H_{10}^{+\bullet}$ ($M^{+\bullet}$)	TS $(M\text{-}H)^{+}$	$(M\text{-}H)^{+}$	TS $((M\text{-}H)\text{-}H)^{+\bullet}$
98	100	(3185)	104	(3190)
151	145	25	141	70
211	199	36	201	94
247	244	50	236	135
262	254	61	274	158
359	354	63	320	183
403	398	354	380	320
412	414	398	391	380
462	459	414	407	391
499	468	459	466	407
506	471	468	479	466
507	501	471	512	479
508	504	501	514	512
536	538	504	524	514
554	539	538	537	524
582	546	539	547	537
595	601	546	598	547
688	676	601	607	598
703	687	676	679	607
718	694	687	683	679
749	711	694	736	683
755	742	711	738	736
763	779	742	749	738
810	806	779	774	749
814	815	806	801	774
814	831	815	809	801
834	841	831	828	809
857	873	841	857	828
906	948	873	870	857
919	959	948	961	870
978	992	959	972	961
980	993	992	973	972
984	1002	993	998	973

986	1004	1002	1005	998
994	1012	1004	1020	1005
1014	1014	1012	1095	1020
1090	1095	1014	1105	1095
1113	1122	1095	1139	1105
1126	1144	1122	1163	1139
1165	1168	1144	1164	1163
1168	1171	1168	1188	1164
1198	1202	1171	1217	1188
1204	1213	1202	1230	1217
1230	1234	1213	1235	1230
1261	1248	1234	1251	1235
1263	1264	1248	1273	1251
1268	1266	1264	1308	1273
1343	1365	1266	1380	1308
1351	1370	1365	1393	1380
1399	1373	1370	1409	1393
1426	1423	1373	1422	1409
1433	1448	1423	1449	1422
1457	1451	1448	1450	1449
1458	1463	1451	1491	1450
1482	1466	1463	1523	1491
1513	1516	1466	1562	1523
1533	1520	1516	1590	1562
1593	1560	1520	1605	1590
1624	1580	1560	1637	1605
1633	1585	1580	1798	1637
1642	1593	1585	3181	1798
1668	1657	1593	3182	3181
3156	3182	1657	3184	3182
3157	3182	3182	3187	3184
3160	3184	3182	3189	3187
3161	3185	3184	3190	3189
3168	3187	3187	3200	3200
3168	3188	3188	3200	3200
3176	3196	3196	3207	3207
3176	3196	3196		
3185	3208	3208		
3185	3208	3208		
1.01	1.02		1.01	
0.56	0.55		0.58	
0.36	0.36		0.37	